The Effects of Elevated Temperature and Laminating on the Quasi-Static and Fatigue Properties of Electrical Steel

by

Gurmeet Gill

A thesis
presented to the University of Waterloo
in fulfillment of the
thesis requirement for the degree of
Master of Applied Science
in
Mechanical and Mechatronics Engineering

Waterloo, Ontario, Canada, 2023

Author's Declaration

This thesis consists of material all of which I authored or co-authored: see Statement of Contributions included in the thesis. This is a true copy of the thesis, including any required final revisions, as accepted by my examiners.

I understand that my thesis may be made electronically available to the public.

Statement of Contributions

Section 4.2.1 was co-autored by myself and Dr. Dulal Saha. He is a post-doctoral fellow who conducted the experiments to gather the microstructural information that is presented in this section. Additionally, the micro-graphs in section 4.3 and the micro-hardness testing presented in section 5.4 was done by him.

A condensed analysis on Chapter 5 of this thesis was approved for publication by SAE International for WCX 2023. This paper is co-authored by my supervisor Dr Hamid Jahed, Dr. Dulal Saha and Dr. Behzad Behravesh, both of which are post-doctoral fellows, Yi-Hsin Chen, Marie Mills, Wensheng Zhang, and Gianni Lamonaca who are all members of Stellantis. I carried out the writing of the paper, the lab experiments and the fracture analysis. Dr. Jahed, Dr. Saha and Dr. Behravesh supervised the experiments and gave guidance on how to carry out the analysis and the testing. Yi-Hsin Chen, Marie Mills, Wensheng Zhang, and Gianni Lamonaca helped to guide the research which would not have been possible without the help of Stellantis.

Abstract

Electrical steel is an alloy of steel that can have on average 3% silicon. These alloys are known to possess great magnetic properties, and this makes them an ideal material choice for the application of electric motors as they are used in the rotor and stator construction. Rotors and stators are comprised of laminated stacks of thin electrical steel sheets. As the automotive industry moves towards electrification of automobiles, it is crucial to comprehend the impact of laminating electrical steel and exposing it to higher temperatures on both the quasi-static and fatigue properties.

An electric motor can reach high temperatures under a heavy load, and it is important to understand the combined effect of temperature and load on the electrical steel's performance to ensure the durability and safety of electric vehicles. This research investigated the quasi-static and fatigue strength and failure behavior of stamped 0.27mm thick electrical steel sheets as well as laminated electrical steel samples that were comprised of 8 individual sheets. Stress-controlled fatigue tests were performed at both room temperature and 150°C. The quasi-static test results showed a decrease in mechanical strength at the higher temperature in terms of the elastic modulus, ductility, yield strength and ultimate tensile strength. The single sheet samples had a decrease in yield strength by 21% and a decrease in elastic modulus by 5%. The laminated samples had a decrease in yield strength by 18% and a decrease in elastic modulus by 6.7%. The cyclic test results showed a decrease in the fatigue life of the samples at the elevated temperature compared to room temperature, in both the LCF (Low Cycle Fatigue) and HCF (High Cycle Fatigue) regimes. For the single sheet samples a decrease in life of 21% was observed at 0.51 normalized stress and 55% at 0.40 normalized stress. For the laminated samples a decrease in life of 38% was observed at 0.51 normalized stress and 56% at 0.40 normalized stress. Examination of the fracture surface of the single sheet samples tested at room temperature showed some inter-granular cleavage facets along with predominant trans-granular facets in the crack initiation zone and transitioned to only trans-granular cleavage facets in the crack propagation zone, at both the low- and high-cycle regimes. In contrast, the high temperature samples showed a smaller fatigue damage zone, and outside of this zone, the main failure mechanism was severe necking for both the low- and high-cycle samples. The laminated samples behaved similarly to the single sheet samples and possessed very similar quasi-static and fatigue properties. Regardless of test condition and load level, the crack always initiated from the breakaway zone on the stamped edge of the samples. The higher temperature

adversely affected the overall strength, as the higher temperature releases residual stresses and annihilates dislocation density induced during the sheet manufacturing and sample preparation, resulting in shorter fatigue life.

Acknowledgements

I wanted to begin by thanking Professor Hamid Jahed for allowing me to work on this research. He has supported me in every step of the process of the research by providing me guidance and direction. It was only with his support that I was able to join the master's program at the University of Waterloo, and the success of this research is a result of his support.

I want to thank Dr. Behzad Behravesh and Dr. Dulal Saha as well. Behzad's help and guidance in this research cannot be understated as he helped train me on the machines used for the research. He has also given me a lot of good advice whenever I had to make decisions regarding the direction of the research. Whenever I needed help with any portion of the research, testing or reporting, he made sure to devote as much time as needed to make sure that I was going in the right direction. Dulal's support has also been very important for the progress of the research. He has helped me in a lot in interpreting the test results, helped me to learn how to use the scanning electron microscope, and helped to make sure that I am reporting the results correctly. This research would not have been possible without their help. I want to also thank Tamuno-Ibim Tolofari. He has also worked on the same project as myself and his research and mine overlaps quite a bit. He and I had discussions regarding the research and we helped advise each other and made sure to support each other in this research.

I want to thank the Natural Sciences and Engineering Research Council of Canada (NSERC) Alliance and Stellantis as the research performed in this thesis was financially supported by them under grant number ALLRP 556432 - 20.

Finally, I want to thank my family. I want to thank my father, mother, sister and brother. While the FATSLAB team has been supporting me inside and outside the lab, my family has given me a lot of support at home and their support has helped me to progress in the research.

Table of Contents

Author's Declaration ii

Statement of Contributions iii

Abstract iv

Acknowledgements vi

List of Figures x

List of Tables xvii

Chapter 1: Introduction 1

1.1 Motivation . . . 1

1.2 Objectives . . . 2

1.3 Thesis Overview . . . 2

Chapter 2: Background and Literature Review 5

2.1 Manufacturing Process . . . 7

2.2 Microstructure of Electrical Steel and The Role of Silicon Content . . . 9

2.3 Effects of Punching on Electric Steel . . . 17

2.4 Joining of Laminated Electrical Steel . . . 22

2.5 Quasi-Static Analysis . . . 27

2.5.1 Quasi-Static Behavior of Electrical Steel . . . 30

2.6 Cyclic Loading (Fatigue) Analysis . . . 35

2.6.1 Fatigue Behavior of Electrical Steel . . . 38

Chapter 3: Methodologies 43

3.1 Material Characterization . . . 43

3.2 Mechanical Characterization . . . 45

3.2.1 Quasi-Static Testing Method . . . 45

3.2.2 Fatigue Testing Method . . . 46

3.3 Sample Preparation . . . 46

3.4 Quasi-Static Test Setup . . . 49

3.5 Fatigue Test Setup 49

Chapter 4: Quasi-Static Behavior of Electrical Steel at Room and High Temperature 50

4.1 Material and Methods 50
4.2 Results 50
4.2.1 Microstructural Analysis 50
4.2.2 Quasi-Static Testing Room Temperature 54
4.2.3 Quasi-Static Testing High Temperature 56
4.3 Analysis 57
4.3.1 Fracture Analysis 59
4.3.2 Further Failure Analysis 61
4.4 Discussion 63
4.5 Chapter Conclusion 65

Chapter 5: Fatigue Behavior of Electrical Steel (Room and High Temperature) 66

5.1 Material and Methods 66
5.2 Results 66
5.2.1 Fatigue Testing Room Temperature 66
5.2.2 Fatigue Testing High Temperature 68
5.3 Analysis 70
5.3.1 Fracture Analysis 73
5.4 Discussion 76
5.5 Chapter Conclusion 80

Chapter 6: Laminated Electrical Steel Quasi-Static and Fatigue Testing Behavior 81

6.1 Methods and Materials 81
6.2 Results 81
6.2.1 Quasi-Static Testing Room Temperature 81
6.2.2 Quasi-Static Testing High Temperature 83
6.2.3 Fatigue Testing Room Temperature 84
6.2.4 Fatigue Testing High Temperature 86
6.3 Analysis 88

6.3.1 Quasi-Static Properties . . . 88
6.3.2 Fatigue Properties . . . 89
6.3.3 Fracture Analysis of Quasi-Static Testing . . . 90
6.3.4 Fracture Analysis of Fatigue Testing . . . 92
6.4 Discussion . . . 97
6.4.1 Quasi-Static . . . 97
6.4.2 Fatigue . . . 99
6.5 Chapter Conclusion . . . 101

Conclusion, Research Contribution and Future Work **103**
Thesis Conclusions . . . 103
Research Contributions . . . 104
Recommended Future Work . . . 105

Letters of Copyright Permission **106**

Bibliography **109**

List of Figures

Figure 1: Graphical abstract of the research conducted for electrical steel 4

Figure 2: (a) Historical development of core loss reduction in electrical steel (b) development of thinner-gauge material by NSC [3] 6

Figure 3: Electric motor applications within a modern automobile [5] 7

Figure 4: Manufacturing process of grain-oriented and non-oriented electric steels [8] . . 8

Figure 5: Single crystal projections (a & d), unit cell orientation (b & e) and pole figures (c & f) for the cube-on-edge and cube texture, the two main crystal orientation of electrical steels [1] 10

Figure 6: The effect of relative elongation under straightening annealing on the dislocation structure of 50WW470 electric steel (a) $\varepsilon = 0$, (b) $\varepsilon = 0.015$, (c) $\varepsilon = 0.02$, (d) $\varepsilon = 0.035$, (e) $\varepsilon = 0.04$, (f) $\varepsilon = 0.05$ [11] 11

Figure 7: Electrical steel microstructure of (a) sample A, 50W800: 0.80% Si (b) sample B, 50W600: 1.57% Si (c) sample C, 50W300 2.52% Si, showing the increase in grain size with additional Si content [12] 12

Figure 8: Magnetic properties of samples from figure 7 [12] 13

Figure 9: The influence of grain size on the core losses in electrical steel with varying silicon content [14] 14

Figure 10: Mass gain during oxidation of steel in 15% humidity with (a) 0.02% Si content (b) 3.2% Si content [18] 16

Figure 11: Cross section of steel after oxidation for 15 minutes (a) at 850°C with 0.02% Si content (b) at 1100°C with 3.2% Si content [18] 16

Figure 12: SEM images of silicon steel oxidized for 20 minutes at (a) 950°C (b) 1100 °C (c) 1150°C [20] 17

Figure 13: Punching of electric steel sheets showing how a burr is formed [21] 18

Figure 14: Cross section of M330-35A electric steel (a) away from cutting edge and (b) at the cutting edge. region 1: finer elongated grains, region 2: deformed area where grains are not visible, region 3: bend contours, region 4: un-deformed region [21] 18

Figure 15: EBSD results on sample shown in figure 14(b) showing plastic deformation (dark areas) and which plane the grains are aligned in [21] 19

Figure 16: Residual stress measurement near the cutting edge of electrical steel, for an annealed and un-annealed sample [24] 20
Figure 17: (a) S-N curves obtained for different various specimen configurations of M330-35A (b) micro-hardness measurements for these same specimens [23] 21
Figure 18: (a) Fracture surface of electrical steel 30WGP1600 (b) crack growth of 30WGP1600 showing the crack initiate from the surface and show trans-granular fracture through grain boundaries as the main crack propagation mechanism [27] . . . 22
Figure 19: Three joining methods of laminated electric steel: (a) adhesive bonding (b) mechanical bonding (c) welding [28] 23
Figure 20: The relationship between torque and torsion angle of laser welded laminations at different welding speeds [28] 24
Figure 21: The relationship between welding speeds and the magnetic field strength of welded laminations shown in figure 20 [28] 25
Figure 22: (a) Flow of eddy currents on a non-welded sample (b) flow of eddy currents on a welded sample [28] 26
Figure 23: Varnish preparation, electrical steel coating, stacking and lamination process [33] 27
Figure 24: Elastic stress-strain curve [35] 28
Figure 25: True stress-strain curve [35] 29
Figure 26: Tensile test specimen geometry according to ASTM E345 [37] 30
Figure 27: (a) Stress-strain curve for electrical steel with 3.3% Si content (b) fracture surface after test showing local necking and (c) trans-granular cleavage facets [38] 30
Figure 28: (a) Stress-strain curve for electrical steel with 2.9% Si content [40] 31
Figure 29: (a) Microstructure of Fe-3Si electrical steel (b) grain size distribution of the electrical steel [40] 31
Figure 30: (a) Light-optical micro-graph of the sample before the test. Plastic strain component in axial direction of the least-square fit strain tensor for each grain for (b)–(f) 1.5%, 4%, 10%, 19.5%, 40%. The shape change of the grains is not reflected. [42] 33

Figure 31: (a)–(e) Grain orientation gradient for plastic strain 0%, 1.5%, 4%, 10%, 19.5%. The regions in black indicate failure of automatic orientation estimation. (f) Optical photograph of the sample with 40% plastic strain showing necking. [42] 34
Figure 32: Anisotropy of the mechanical properties of electrical steel [43] 35
Figure 33: General constant amplitude loading [35] 35
Figure 34: Characteristic S-N diagram (a) plot of sample results (b) resulting line of best fit in results [35] 36
Figure 35: Fatigue test specimen geometry according to ASTM E466 [49] 38
Figure 36: S-N curve normalized to the yield strength, stress amplitude versus number of cycles, for (a) polished sample (R = 0.1) and (b) punched samples (R = 0.005) [38] 39
Figure 37: Labeled diagram of the punched edge of an electrical steel sample [47] 40
Figure 38: SEM image of the fracture surface at (a) 0.5% strain, where trans-granular crack initiation is found (b) 1% strain where inter-granular crack initiation is found and (c) above 1% strain where brittle crack propagation occurs. [40] . . 40
Figure 39: Crack length of stamped electrical steel M330-35A as a function of number of cycles, fatigue tested at room temperature, R = 0.1, 64Hz, Nf = 187,595 [47] 41
Figure 40: Fatigue sample of 30WGP1600 with Nf = 62400 cycles (a) fatigue crack initiation from a surface inclusion (b) energy spectrum of inclusion indicating that this inclusion is aluminum nitride [27] 42
Figure 41: Stress-life curves for electrical steel recorded at 20°C and 180°C [47] 42
Figure 42: Zeiss LEO 1530 FE-SEM 43
Figure 43: Keyence VK-X250 [51] 44
Figure 44: Measurement of final cross sectional area using ImageJ 44
Figure 45: Clemex CMT (version 8.0.197) [53] 45
Figure 46: MTS 810 with Instron environmental chamber (a) and Instron 8874 (b) . . . 46
Figure 47: Sample geometry used for both the single sheet samples and the laminated samples. Thk = 0.27mm for single sheet samples, Thk = 2.16mm for laminated samples 47
Figure 48: Illustration of the sample's geometries 47
Figure 49: High temperature quasi-static test setup for laminated samples 48
Figure 50: (a) Single sheet sample (b) laminated sample 49

Figure 51: Micro-graph of electrical steel in the rolling direction 51
Figure 52: Phase identification of the electrical steel in the rolling direction 51
Figure 53: Fe-Si phase diagram [56] 52
Figure 54: (a) Grain orientation of electrical steel in the rolling direction, (b) graph showing the angular misalignment of the grains 52
Figure 55: Crystallographic texture of the electrical steel 53
Figure 56: Aluminum nitride precipitates shown (a) along the grain boundaries and (b) within the grains 53
Figure 57: Top layer of the sample showing a mixture of the silicon oxide layer and insulation layer, totalling to 0.5-1 µm in thickness 54
Figure 58: Room temperature quasi-static test results for single sheet samples (a) engineering, and (b) true stress-strain curves 55
Figure 59: Room temperature quasi-static tested single sheet samples, painted and speckled for strain measurement using DIC (a) before and (b) after testing 56
Figure 60: High temperature quasi-static test results for single sheet samples (a) engineering and (b) true stress-strain curves 56
Figure 61: High temperature quasi-static tested single sheet samples, painted and speckled for strain measurement using DIC (a) before and (b) after testing 57
Figure 62: Quasi-static stress-strain curves of single sheet samples (a) engineering stress (b) true stress 58
Figure 63: Fracture surface of room temperature quasi-static tested single sheet (a) overall view of fracture surface (b) local necking (c) local necking-transition zone (d) edge of sample (e) crack initiation zone with inter-granular cleavage facets (f) crack propagation zone with inter-granular cleavage facets (g) transition zone to local necking 59
Figure 64: Fracture surface of high temperature quasi-static tested single sheet (a) fatigue damage zone showing some severe thinning (b) crack initiation zone (c) other side of fracture surface showing some deformation twinning and severe thinning 60
Figure 65: Fracture surface CAD drawing of a quasi-static tested sample at (a) room temperature (b) high temperature 61

Figure 66: Side view of the fracture zone of room temperature quasi-static tested single sheet (a) overall sample (b) highlighted (red line in (a)) edge under OM (c) highlighted edge under SEM, showing trans-granular failure 62
Figure 67: Side view of the fracture zone of high temperature quasi-static tested single sheet (a) overall sample (b) highlighted (red line in (a)) edge under SEM (c) highlighted edge under OM, with grains showing considerable elongation (highlighted in blue) 63
Figure 68: Fatigue results for room temperature tested single sheet samples 67
Figure 69: Fatigue samples for room temperature tested single sheet samples 68
Figure 70: Fatigue results for high temperature tested single sheet samples 69
Figure 71: Fatigue samples for high temperature tested single sheet samples 70
Figure 72: Fatigue results for room and high temperature tested single sheet samples . . 71
Figure 73: Fatigue properties for room temperature tested single sheet samples 71
Figure 74: Fatigue properties for high temperature tested single sheet samples 72
Figure 75: Fracture surface of single sheet sample at room temperature, low cycle fatigue, Nf = 27,728 cycles, (a) overall fracture surface (b) crack initiation zone with visible striations (c) trans-granular cleavage facets 73
Figure 76: Fracture surface of single sheet sample at room temperature, high cycle fatigue, Nf = 557,532 cycles, (a) overall fracture surface (b) fatigue damage zone (c) crack initiation zone (c) trans-granular cleavage facets 74
Figure 77: Fracture surface of single sheet sample at high temperature, low cycle fatigue, Nf = 25,583 cycles, (a) overall fracture surface (b) fatigue damage zone (c) trans-granular cleavage facets (d) crack initiation zone with visible striations . 75
Figure 78: Fracture surface of single sheet sample at high temperature, high cycle fatigue, Nf = 201,798 cycles, (a) overall fracture surface (b) severe necking (thinning) (c) crack initiation zone (d) fatigue damage zone 76
Figure 79: Laminated sample micro-hardness 78
Figure 80: Cutting edge of punched electrical steel 79
Figure 81: Room temperature quasi-static test results for laminated samples (a) engineering and (b) true stress-strain curves 82
Figure 82: Room temperature quasi-static tested laminated samples, painted and speckled for strain measurement using DIC (a) before and (b) after testing 83

Figure 83: High temperature quasi-static test results for laminated samples (a) engineering and (b) true stress-strain curves 83
Figure 84: High temperature quasi-static tested laminated samples, painted and speckled for strain measurement using DIC (a) before and (b) after testing 84
Figure 85: Fatigue results for room temperature tested laminated samples 85
Figure 86: Fatigue samples for room temperature tested laminated samples 86
Figure 87: Fatigue results for high temperature tested laminated samples 87
Figure 88: Fatigue samples for high temperature tested laminated samples 88
Figure 89: Quasi-static stress-strain curves of laminated samples 88
Figure 90: Fatigue results for room and high temperature tested laminated samples . . . 89
Figure 91: Fractured quasi-static laminated sample grain structure (a) front view (b) close-up to fracture surface (c) angled view (d) side view 90
Figure 92: Fracture surface laminated quasi-static sample room temperature, (a) overall sample (b) cleavage facets and local necking (c) local necking (d) bending and cleavage facets 91
Figure 93: Fracture surface laminated quasi-static sample high temperature (a) overall sample (b) sheet 6, local necking (c) sheet 5, local necking (d) sheet 5, local necking 92
Figure 94: Fatigue samples for room temperature tested laminated sample Nf = 20,423 cycles (a) overall sample (b) close-up view for sheets 1 and 2 (c) fatigue damage zone for sheet 1 93
Figure 95: Fatigue sample for room temperature tested laminated sample, Nf = 233,684 cycles, (a) overall view of fracture surface (b) overall view of sheet 1 (c) fatigue damage zone (d) crack initiation zone (e) overall view of sheet 4 (f) crack initiation zone (g) overall view of sheet 8 (h) trans-granular cleavage facets (i) severe necking (j) crack initiation zone 94
Figure 96: Fatigue sample for high temperature tested laminated sample, Nf = 20,364 cycles, (a) overall view of fracture surface (b) view of sheet 1 (c) crack initiation point of sheet 1 (d) some local necking on sheet 1 (e) view of sheet 8 (f) crack initiation point of sheet 8 (g) some local necking on sheet 8 95

Figure 97: Fatigue sample for high temperature tested laminated sample, Nf = 135,929 cycles, (a) overall view of fracture surface (b) view of sheet 1 (c) crack initiation point of sheet 1 (d) view of sheet 5 (e) fatigue damage zone of sheet 5 (f) crack initiation point on sheet 5 (g) local necking on sheet 5 96
Figure 98: Comparison of quasi-static curves between laminated samples and sheet samples at room temperature 98
Figure 99: Comparison of quasi-static curves between laminated samples and sheet samples at 150°C 98
Figure 100: Stress life curve of laminated samples compared to single sheet samples at room temperature 100
Figure 101: Stress life curve of laminated samples compared to single sheet samples at high temperature 100

List of Tables

Table 1: Material composition of electrical steel used in testing 53
Table 2: Normalized quasi-static test results at room temperature for the single sheet samples 55
Table 3: Normalized quasi-static test results at elevated temperature for the single sheet samples 57
Table 4: Normalized quasi-static test results for the electrical steel single sheet samples . 58
Table 5: Normalized room temperature fatigue results for single sheet samples 67
Table 6: Normalized high temperature fatigue results for single sheet samples 69
Table 7: Normalized quasi-static test results at room temperature for the laminated samples 82
Table 8: Normalized quasi-static test results at high temperature for the laminated samples 84
Table 9: Normalized room temperature fatigue results for laminated samples 85
Table 10: Normalized high temperature fatigue results for laminated samples 87
Table 11: Normalized quasi-static test results for the laminated samples 89

Chapter 1: Introduction

1.1 Motivation

Electrical steel is not a newly discovered alloy of silicon steel, in fact the invention of both grain-oriented and non-oriented electrical steel is close to one hundred years old. It is a silicon alloy steel that is used in the construction of the stator and rotor core of the electric motor. The interest in electrical steel is now growing worldwide and further research into the electrical steel is important now more than ever as automobile companies shift towards electric vehicles. Even though the invention of the electric car pre-dates the invention of the gasoline car, the industry standard for powering transportation as well as industrial equipment has been through the use of internal combustion engines. However, the world climate is going through a rapid change and the greenhouse gases (GHGs) that are produced from internal combustion engine cars must be reduced to help mitigate the effects of climate change.

The overarching goal of this research is to understand and characterize the mechanical behavior of electrical steel to help and support the transition towards electric vehicles. The short term goal in this research is to establish a relationship between the elevated temperature and laminating process on the quasi-static and fatigue properties of electrical steel. The long term goal of this research is help facilitate a change to fully electric vehicles to help reduce GHGs and fight climate change. In order to do this, it is important to characterize the mechanical and thermal behavior of the electrical steel. The purpose here is to establish a relationship between the performance and the microstructure of the electrical steel. This information is crucial in the design of the electric motors as these properties are needed for computer aided design to ensure the electric motor design can be robust. The current literature shows that there is some information regarding the fatigue, the effects of punching on the fatigue as well as the effects of elevated temperatures on electrical steel. In this research however, a baseline measurement for stamped electrical steel will be recorded and compared with the effects of the laminating process with respect to the quasi-static and fatigue properties as well as the effect of temperature on both of these properties.

1.2 Objectives

The objective of this research is to gain a deeper understanding of the mechanical behavior of electrical steel when subjected to cyclic loading, as well as to identify the fracture mechanisms at work and establish a correlation between cyclic performance and material structure. As automotive manufacturers increasingly seek to design more powerful electric motors while reducing their size, this study will make a significant contribution by identifying the durability limitations of such electrical motors.

To achieve the objectives following research plan is pursued:
1. Obtain the fundamental microstructural attributes of electrical steel and the effects of different cutting methods on such attributes.
2. Characterize tensile behavior (at room and elevated temperatures) and to identify its failure mechanisms.
3. Characterize fatigue behavior of the single sheet samples (at room and elevated temperatures), identify failure mechanisms (under cyclic loads) and develop a fatigue model.
4. Characterize tensile behavior of the laminated samples (at room and elevated temperatures), fatigue behavior (at room and elevated temperatures), identify failure mechanisms (under quasi-static and cyclic loads) and develop a fatigue model.
5. Establish a link between material structure and its performance under static and cyclic loading conditions at room temperature and elevated temperatures.

1.3 Thesis Overview

Chapter 2 will review the relevant literature regarding the background of electrical steel, its microstructure, behavior under quasi-static and cyclic loading, effect of temperature and effect of cutting methods.

Chapter 3 will discuss the methodology used in the microstructural and mechanical characterization of the electrical steel sheets. It details the parameters used in the setup used for the microstructural and micro-hardness analysis, the testing of electrical steel (both quasi-static and fatigue testing) and the sample geometry.

Chapter 4 will discuss the microstructural analysis that was conducted on the electrical steel and compare it to what is known in the literature. This addresses the first objective of this research. The chapter will then the quasi-static findings on the electrical steel sheets. This addresses the second objective of this research. This chapter will discuss the tensile behavior of the electrical steel sheets and failure mechanisms at room and elevated temperatures, as well as severe thinning, and potential activation of additional deformation mechanism at high temperature. A correlation between quasi-static behavior and electrical steel structure will be established. Such correlation will be provided at room and high temperature.

Chapter 5 will discuss the cyclic behavior of the electrical steel single sheets. This chapter addresses the third objective of the research. This chapter will discuss the fatigue/cyclic behavior of the electrical steel sheets, root cause of crack initiation, and major differences in crack propagation at room and high temperature. The effect of stamping on microstructure at the edge of samples and its correlation to crack initiation at the low- and high-cycle fatigue will be discussed. Temperature role on relieving the residual stress induced in stamping, and its role in facilitating cracking will be discussed also.

Chapter 6 will discuss the quasi-static and fatigue behavior of laminated electrical steel. This chapter will address the fourth objective. This chapter will discuss the effects of laminating the electrical steel and its effect on the tensile behavior at room and high temperature. This chapter will also discuss the fatigue behavior at room and high temperature for the laminated electrical steel. Similarities and differences in behavior of single and laminated sheets will be discussed in detail.

Finally the Conclusion will highlight the main conclusions of this research, discuss its limitations, and provides a future outlook for key research topic for electrical steels. By culminating the findings of the thesis, the fifth and final objective will be addressed.

Below is a graphical abstract to help visually understand the process that the research followed and how the different topics all relate to the work that was conducted.

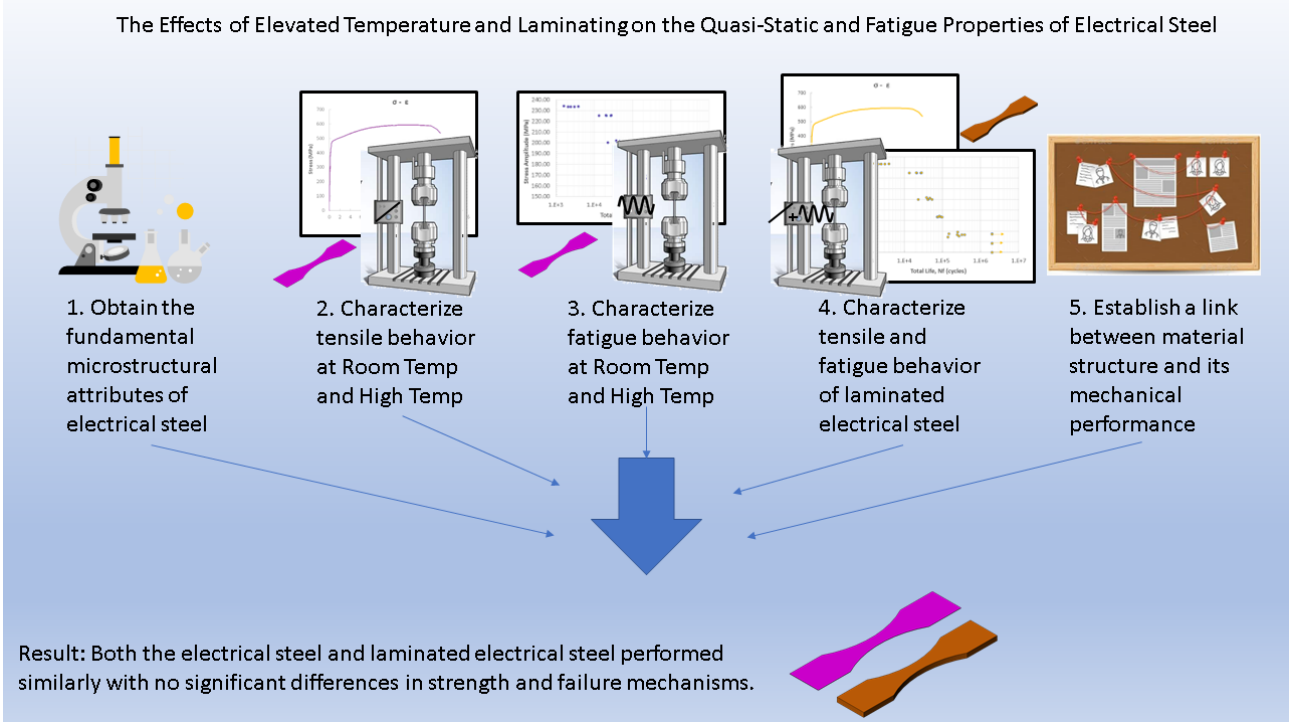

Figure 1: Graphical abstract of the research conducted for electrical steel

Chapter 2: Background and Literature Review

Electrical steel is the most commonly used material in the manufacturing of the stator and rotor core of most electrical machines including motors, generators and transformers [1]. Electrical steel is also referred to as transformer steel and silicon steel. This is a steel alloy that has a high in silicon content and is known for having great magnetic properties, as its magnetic domains can shift with little energy loss. The addition of the silicon to the steel, allows the electrical resistivity to increase which, in turn, causes a reduction in eddy currents and iron losses, which helps to achieve better efficiency. Another benefit to the increase in the silicon content, is that it will cause magnetostriction to decrease which will lead to a lower sensitivity to strain related stress. Magnetostriction is the phenomenon where magnetic materials change their dimensions when they are within a magnetic field due to the magnetic force causing a stress and therefore strain on the material [1]. The electrical steel, when used in the electrical motors mentioned above, is often covered with an insulation coating to prevent eddy currents from travelling from one sheet to another. It is then stacked to the desired height. When this process of coating and assembly is done, it is referred to as laminated electrical steel.

The two main types of electrical steel are grain-oriented and non-oriented electrical steel [1]. Non-oriented electric steel has a silicon content of 0.5-3.25% [2]. It was originally developed by an English metallurgist named Robert Hadfield in 1900 [1]. This variant of electrical steel has no grain orientation, as the name suggests. The benefit of this type of electrical steel is that it can produce a magnetic field in any direction and the magnetic field can be oriented in any single direction once another magnetic field is induced on the material. Since the direction of the grains and subsequently the magnetic domains, are not restricted to a singular direction, this steel is often used in applications where the stack of laminated electrical steel is in motion such as motors, and generators where the magnetic field is required to change direction constantly [2].

The other variant of electrical steel is grain-oriented electrical steels, and as the name suggests, this material has its grain structure oriented in the rolling direction, and this is a by product of the manufacturing process itself. These types of electrical steels have a silicon content of 3-6.5% [2]. This steel was developed sometime after the development of non-oriented electrical steel by a metallurgist named Norman Goss in 1933 [1]. This type of electrical steel will have a fixed magnetic

field with a fixed direction and are typically used in stationary applications such as transformers, where the magnetic field is not changing direction.

Figure 2 below shows the impressive development that has occurred for electrical steel over the past one hundred years. Figure 2a shows the contribution provided by different scientists and corporations to reduce the core losses of electrical steel, thereby increasing the energy efficiency of the corresponding electric machines that they are used in. Figure 2b shows the amazing improvements to decrease the sheet thickness conducted by the Nippon Steel Corporation (NSC) and just how thin electrical steel can now be produced. This is important as thinner sheets can help to reduce eddy current losses and increase energy efficiency of the machines they are utilized in. However, it is important to note that if the sheet becomes too thin, it can also act as a disadvantage as secondary re-crystallization becomes more unstable at this size, hysteresis losses increase, and there will be a reduction in the shaping factor of the part [3]

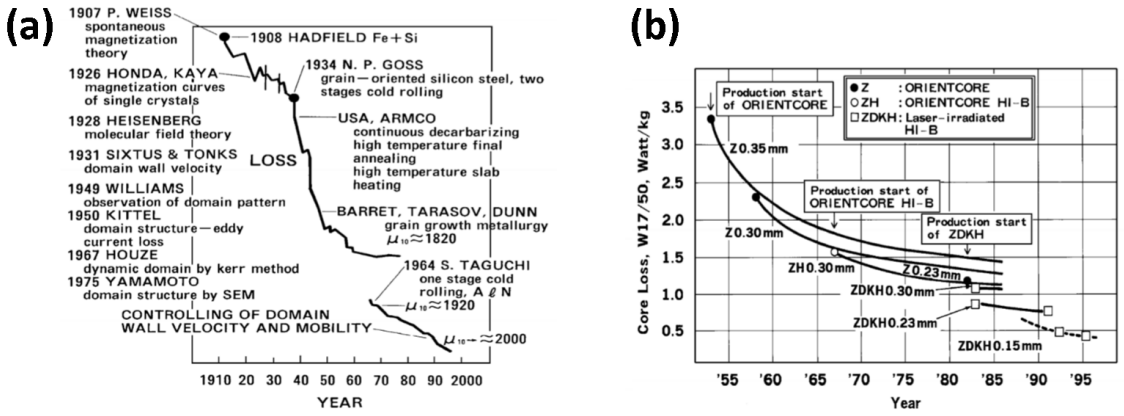

Figure 2: (a) Historical development of core loss reduction in electrical steel (b) development of thinner-gauge material by NSC [3]

The research into electrical steel is very important for the automotive industry, as the average automobile today, while not fully electric, utilizes anywhere from 20-60 small sized motors [4]. This can range from power window actuators, sunroof motors, windshield wiper motors, seat adjustment motors and electric power steering motors. A diagram of this is shown below in figure 3. Improvements to electrical steel not only benefit the electric drive motor design, it can also improve various other motor designs to improve efficiency and overall reliability.

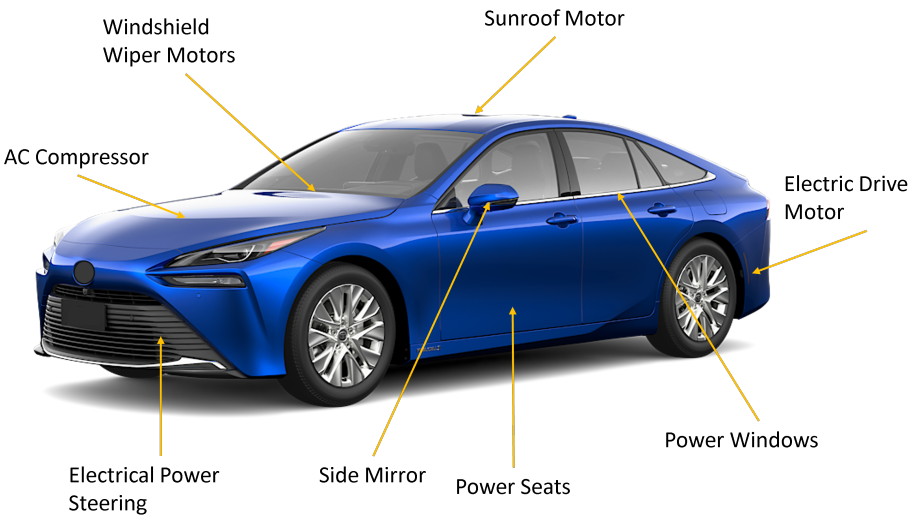

Figure 3: Electric motor applications within a modern automobile [5]

2.1 Manufacturing Process

The magnetic properties of electrical steels can be altered based on their silicon content, and manufacturing process. The two types of electrical steels are grain-oriented and non-oriented electrical steel. A diagram of their manufacturing process is shown in figure 4. They both have very similar manufacturing processes and go through many of the same steps however, the grain-oriented electrical steel requires some extra steps in order to ensure that the magnetic domains are aligned in one direction and, in order to do this, secondary re-crystallization is needed. This however comes at a cost, as the higher silicon content in this grain-oriented electrical steel decreases the ductility of the electrical steel and this will require some additional processes to prevent any cracking [1]. Now primary re-crystallization can form new strain-free grains however, they would not be able to orient in a particular direction. Secondary re-crystallization is a process where the material is annealed at a temperature higher than the temperature required for primary re-crystallization, and where the material is annealed for a very long time. This process allows for very large grain growth that extends the thickness of the cold rolled sheets of electrical steel [1]. To have secondary re-crystallization, there must be something that prevents the normal grain growth that occurs in primary re-crystallization [6, 7]. Second-phase precipitates located at the grain boundaries are what help to do this job and they are normally removed at the high temperature or they disappear into the material as a solid state solution and diffuse towards the grain boundaries during annealing [6].

However, in this processes there can be some impurities which are used to prevent normal grain growth. These are manganese sulfide and aluminum nitride, and it is important to remove them after the annealing process as they can act as wall pinning sites and can restrict the movement of the magnetic domain [1, 6, 7].

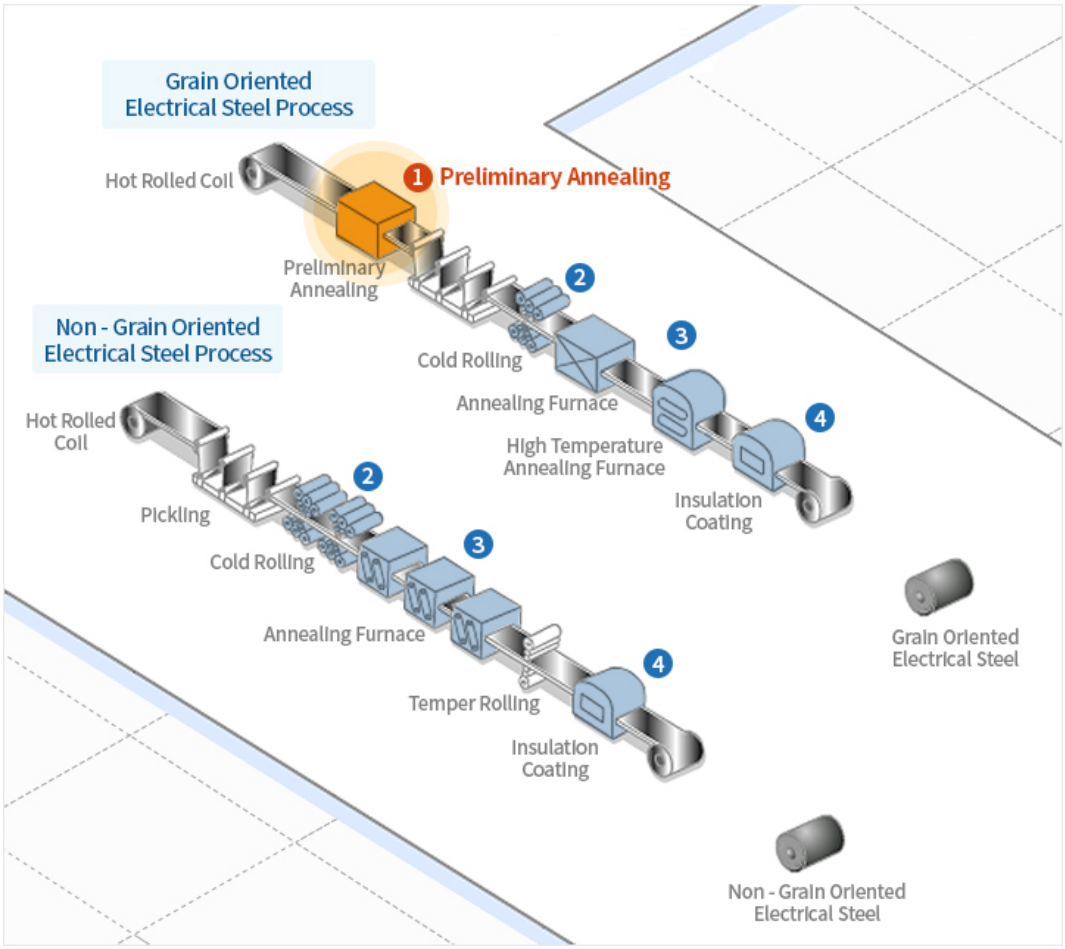

Figure 4: Manufacturing process of grain-oriented and non-oriented electric steels [8]

Both of the electrical steels begin their manufacturing processes with hot rolling [8]. The grain-oriented steel then goes through a primary annealing step. This is done to improve the cold rolling properties of the grain-oriented electrical steel. In addition, this step is done to remove any scales that form during the hot rolling step by passing the sheet through a scale breaker, and an acid bath. Here both of the electrical steels goes through a pickling process before the cold rolling step. From there both types of electrical steels will undergo a cold rolling step where the sheet thickness is reduced by 40% - 90%. After this step both steels undergo an annealing process. This step is done

to remove any residual stresses within the electrical steel. For the grain-oriented electrical steel, the high temperature annealing process is used to create the secondary re-crystallized structures necessary to have a grain-oriented microstructure. Here another process called decarbonization can be used to remove any access carbon from the steel. The process then concludes with both steels receiving an insulation coating that is given when the steels both pass through rollers. This insulation coating is very important for the electrical steel to prepare it for use inside an electrical machine, as it prevents eddy currents from travelling between adjacent sheets when the electrical steel is stacked and laminated. This coating often has magnesium oxide which at a high temperature, combines with silicon oxide to form a glassy magnesium silicate [8]. This not only electrically insulates the electric steel, but it also leaves a residual tensile stress in the steel once it returns to room temperature [1]. This causes the core losses in a motor to decrease as well as form magnetic domain walls 180° to the rolling direction.

2.2 Microstructure of Electrical Steel and The Role of Silicon Content

The secondary re-crystallized structure in the electric steel is much more different than the primary re-crystallized structure and is much stronger as well [1]. The primary texture is very complex, and does not possess as much strength. Secondary re-crystallization can only occur if normal grain growth is inhibited [3]. The plane of (011) is the plane that is parallel to the sheet thickness and [100] is the rolling direction for the stereographic projections shown in figure 5. Figure 5 shows that the cube-on-edge texture makes the <100> family of directions in all grains almost parallel to one another, and this is the direction mainly used for quoting the properties of the grain-oriented electrical steel [1, 3]. The coarse grained texture of {110} <100> shown in figure 5 is the principle direction and has the highest torque strength [9, 10]. These are the two main crystal orientations that are shown in grain-oriented electrical steel and are the result of secondary re-crystallization in addition to the rolling process.

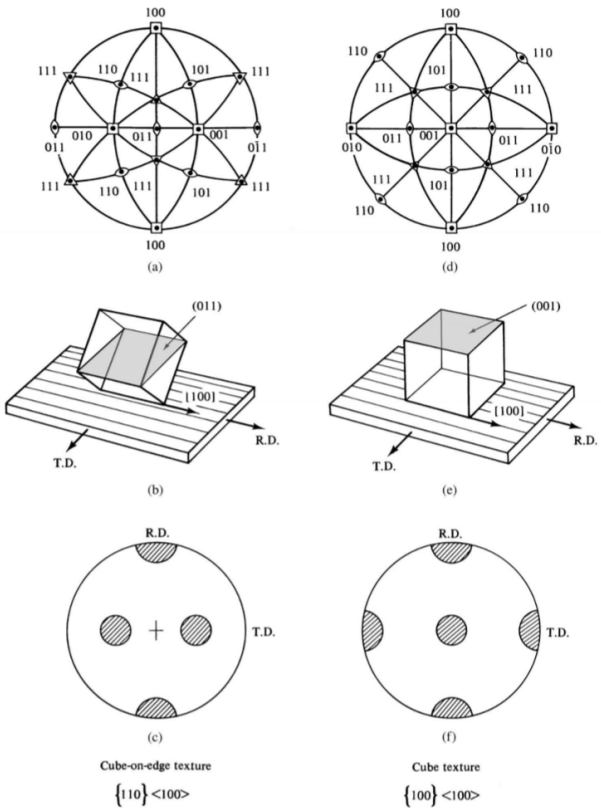

Figure 5: Single crystal projections (a & d), unit cell orientation (b & e) and pole figures (c & f) for the cube-on-edge and cube texture, the two main crystal orientation of electrical steels [1]

In manufacturing the grain-oriented and non-oriented electrical steel, one key issue that can affect the final product is the effect of residual stresses. Residual stress can inhibit the movement of magnetic domains and it is one of the largest factors that will cause a transformer to drop in energy efficiency and lose power internally [11]. Residual stresses can appear in the electrical steel for many different reasons and is a by-product of the entire manufacturing process of the electrical steel. It mainly comes from the cold and hot rolling process, it can come from a cutting/stamping process and it can come from a joining process. Figure 6 below shows the effects of different strains during the elongation of electric steel under straightening annealing, which is a process that takes place during the annealing step. It is important to note that figure 6a was not elongated and it shows very little to no dislocations along the grain boundaries. However, as the strain increases, the dislocation cluster around the grain boundaries increase. This is not good for the magnetic properties of the electrical steel as residual stresses restrict the movement of the magnetic domains which can greatly deteriorate the energy efficiency of the electrical device. The same research done by Korzunin et al. [11] goes on to prove that the increase in the strain of the material greatly

increases the power losses and the magnetic field deterioration.

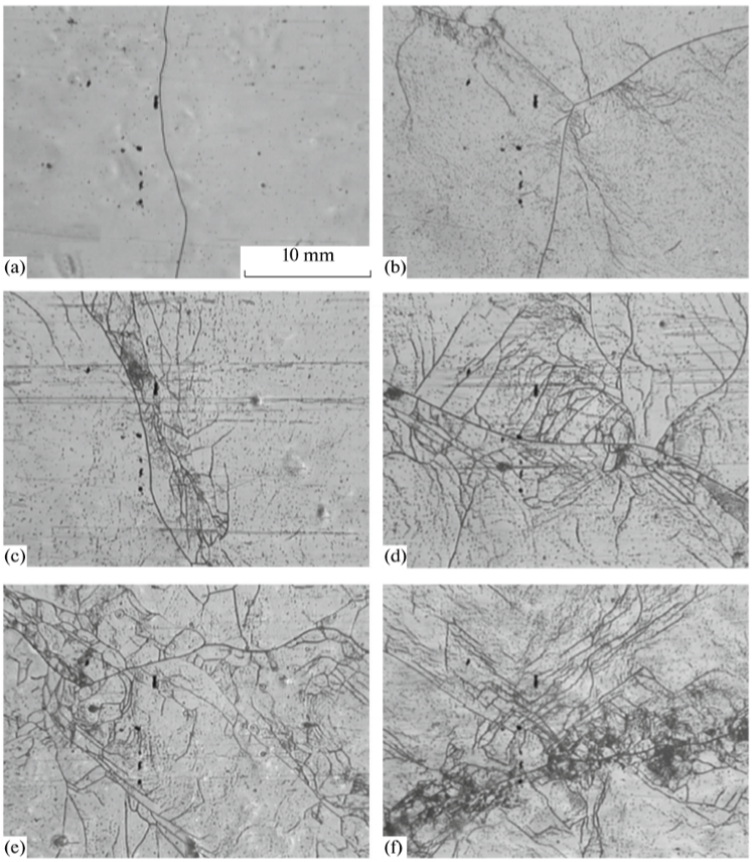

Figure 6: The effect of relative elongation under straightening annealing on the dislocation structure of 50WW470 electric steel (a) $\varepsilon = 0$, (b) $\varepsilon = 0.015$, (c) $\varepsilon = 0.02$, (d) $\varepsilon = 0.035$, (e) $\varepsilon = 0.04$, (f) $\varepsilon = 0.05$ [11]

Electrical steel production has increased due to the recent popularity of electric vehicles, and due to this, there is a growing push towards getting greater magnetic properties and greater strength from the electric steel. Silicon is the key alloying element used in electrical steel and it can improve the resistivity, reduce the eddy currents and hysteresis losses [12]. In addition to this, the silicon content can make the grain size bigger as well as reduce the austenite content in the microstructure [12]. An increase in silicon content is important in achieving better magnetic properties however, it is important to understand the effect that the added silicon will have on the mechanical properties of the material.

Ye et al. [12] conducted a study to determine the effect additional silicon content on the microstructure of electrical steel. They found that an increase in silicon content causes the annealing temperature and the time for annealing to increase for the electric steel. In this study, sample A was annealed at 880°C with a speed of 120 m/min, sample B was annealed at 900°C with a speed of 95 m/min and sample C was annealed at 920°C with a speed of 80 m/min. Here, the additional silicon content can decrease the ductility and as a result, more time is required to allow for better re-crystallization and to allow for the larger grain growth that results from the additional silicon content [12]. Below the effects of adding additional silicon content are shown in figure 7.

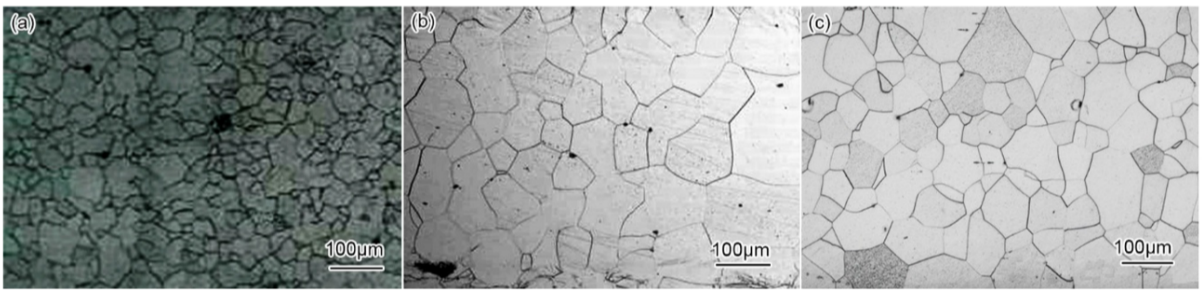

Figure 7: Electrical steel microstructure of (a) sample A, 50W800: 0.80% Si (b) sample B, 50W600: 1.57% Si (c) sample C, 50W300 2.52% Si, showing the increase in grain size with additional Si content [12]

During the hot rolling process of the electric steel, austenite can form within the microstructure This is the gamma phase of iron and it is soft and ductile. This phase in the electric steel only occurs when the silicon content is below 1.7% [12]. As a result, only the sample shown in figure 7a has austenite in the microstructure. However, since the other two samples have the larger grain sizes, they become more brittle, and the strain energy increases due to the increase of the silicon content. This makes them even more difficult to deform which is advantageous to the overall strength of the electrical steel, even if it affects the manufacturability [12]. The microstructure does however confirm that the increase in silicon content does lead to larger grain growth. It is known that the addition of Si in the steel accelerates the formation of ferrite which in turn, promotes the formation of austenite through nucleation followed by grain growth [13]. This process of grain growth promotes the growth of austenite of higher hardenability which results in a higher volume of martensite in the final structure, overall resulting in an increase of mechanical strength [13]. However, if too much aluminum nitride or manganese sulfide precipitates are found in the

microstructure, it will restrict grain growth and can affect the magnetic properties of the electrical steel as well [6]. The average grain diameter for samples shown in figure 7 are as follows: sample (a) was approximately 50 µm, sample (b) was 75 µm and sample (c) was 87 µm [12]. The effects of the additional silicon content on the magnetic properties are explored in figure below 8.

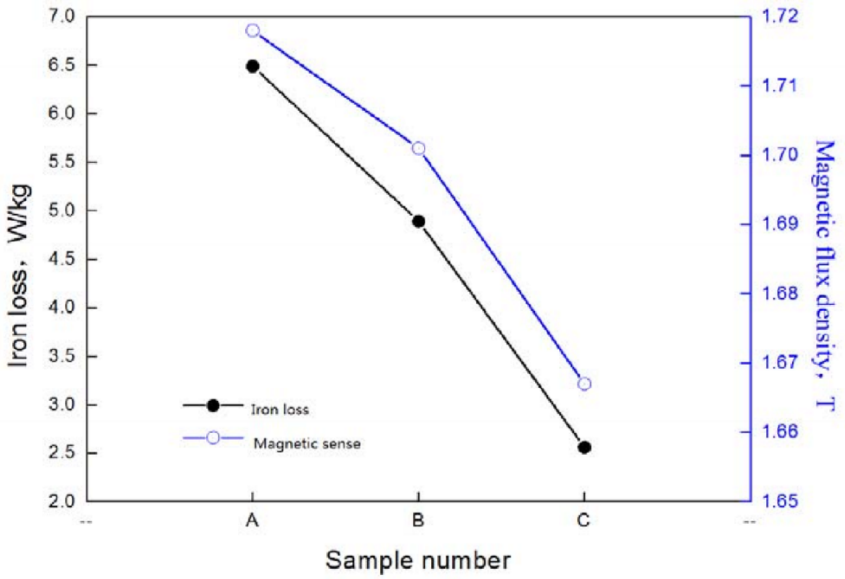

Figure 8: Magnetic properties of samples from figure 7 [12]

The improvement of the texture of the electric steel with the increase of the silicon content allowed for better magnetic properties (in general) as shown in figure 8. The samples in this graph from A to C increase in the silicon content and it shows a downward trend of iron losses [12]. The iron losses are the combination of losses within the electric steel due to the eddy currents and the deterioration of the magnetic hysteresis curve. Here the magnetic flux density also decreased with the silicon content, which is unusual however, the change here is very small and this slight decrease can be accounted for by the increase in the residual stresses caused by the additional silicon [12]. There are many factors that can influence the magnetic properties of electrical steel. Grain size is another factor that can influence the core loses. According to Shimanaka et al. [14] the increase in silicon content decreases the core loses of the material, but the relationship between the grain size is different. Figure 9 below shows that the approximate grain size of 100 µm to 150µm allows for the lowest losses and that above this size, the losses increases. This behavior is an important finding and proves that there is an optimal grain size that allows for the lowest core loses.

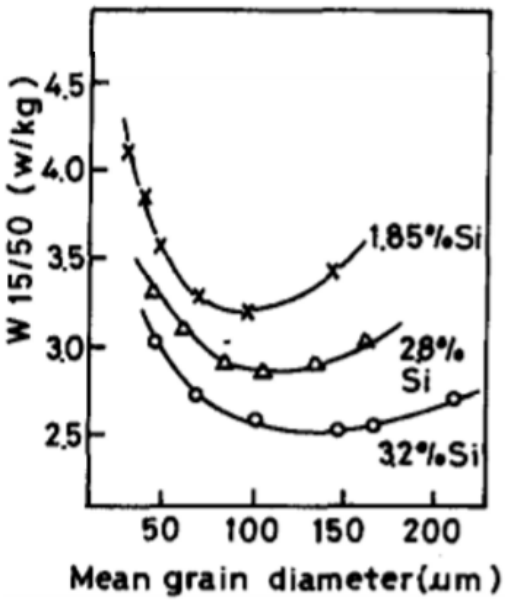

Figure 9: The influence of grain size on the core losses in electrical steel with varying silicon content [14]

Increasing the Si content can further improve electrical resistivity of electrical steel, can increase the saturation magnetization and can reduce the magnetostriction to near zero [10, 15]. However, increasing the silicon content past 3.7% can inhibit secondary re-crystallization and controlling the microstructure can be more difficult [7]. This is important as in a typical electric motor, the iron losses can contribute to 20% of the power losses in the system [10]. Normal production of electric steel limits the silicon content to 3.25 % to achieve a more reliable manufacturing process. Various studies have been done to try and achieve 6.5% silicon. Since the added silicon content improves the magnetic behavior of the material, it is advantageous to increase the percentage of silicon content. The normal manufacturing process for electrical steel cannot work at these high silicon contents as the material becomes very brittle in nature however, cold rolling is still possible. It is more costly but the sheets can be hot-rolled, warm-rolled and then cold-rolled to manufacture this type of electrical steel however, the process requires tighter control [16, 9]. Chemical vapor deposition is a chemical process that can be used to synthesize 6.5% Si electrical steel. This process can produce a sheet that is 0.1mm-0.3mm with great magnetic properties [15]. This process is carried out by using a chemical displacement reaction with silicon chloride ($SiCl_4$) in an inert gas atmosphere at 1200°C, that will react with the iron to deposit Fe_3Si on to a 3% Si electrical steel sheet to convert

it to a 6.5% Si electrical steel sheet [15]. This is a revolutionary process that achieves what normal cold rolling cannot, as high silicon content makes the electrical steel very brittle. Electron beam physical vapor deposition is another process that can increase the silicon content of electrical steel to 6.5%. This process involves a stainless steel disk substrate that contains the high silicon content. This substrate is heated and then using electron beams, the ingot iron and silicon are bombarded, converted into a gaseous state, and then deposited on the stainless steel disk where they harden to create the desired electrical steel [17].

The effect of adding in silicon content helps improve electrical resistivity and this property is needed for electrical steel. However, for normal steels, silicon content is often added to improve mechanical and corrosion resistance as well [18, 19]. Khan et al. [19] found in structural steel S275, that adding 1.6% Si reduced the corrosion rate to 18% of the original rate for S275 which contains no silicon. It was also found that the silicon content had minimal degradation on the mechanical properties of the structural steel. In steel, adding in greater silicon content can improve corrosion resistance by forming layers of silica (SiO_2), fayalite (Fe_2SiO_4) or at higher temperatures, wustite (FeO) [18]. At high oxidation temperatures, the silicon can form a layer of silica up to 950°C. Above this temperature and below 1150°C fayalite begins to form as a scale layer which will also help to inhibit corrosion however, above 1177°C the iron will begin to corrode and form wustite (FeO) and fayalite which infiltrates scale and grain boundaries. Figure 10 below shows the mass gain for steel with silicon content of 0.02%, and 3.2%. The steel with 3.2% Si performs much better in reducing the oxidation and has very little oxidation below a temperature of 1177°C. A cross section of these samples that were oxidized for 15 minutes is shown below in figure 11. It shows that the sample with the greater silicon content has a protective layer of fayalite and wustite which prevents oxidation. At lower temperatures such as 850°C the sample shown in figure 11b would also have a silica layer which would further prevent oxidation. This is an added benefit to have for electrical steel as it allows for a more controlled heat treating process however, it does make the pickling process more difficult depending on which scale layer forms [18]. While the rotor and stator core will not likely be exposed to a corrosive environment since they are enclosed within an electric motor, it is still a beneficial trait to have as it makes the manufacturing and transportation of electrical steel much easier.

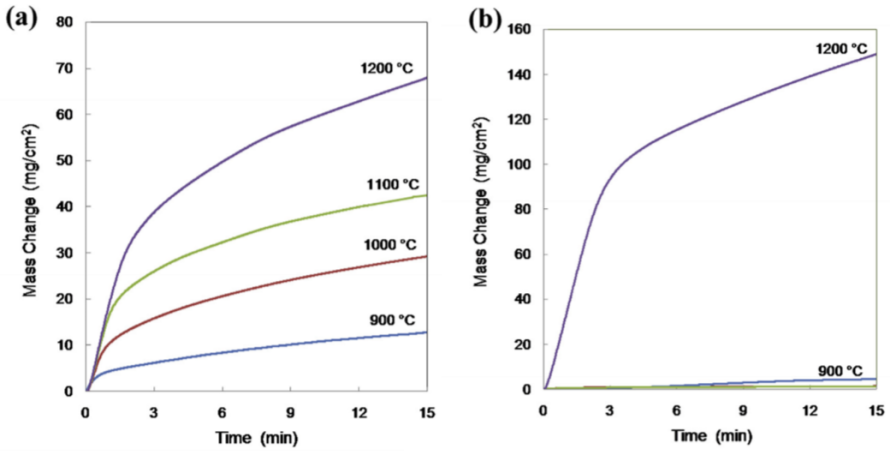

Figure 10: Mass gain during oxidation of steel in 15% humidity with (a) 0.02% Si content (b) 3.2% Si content [18]

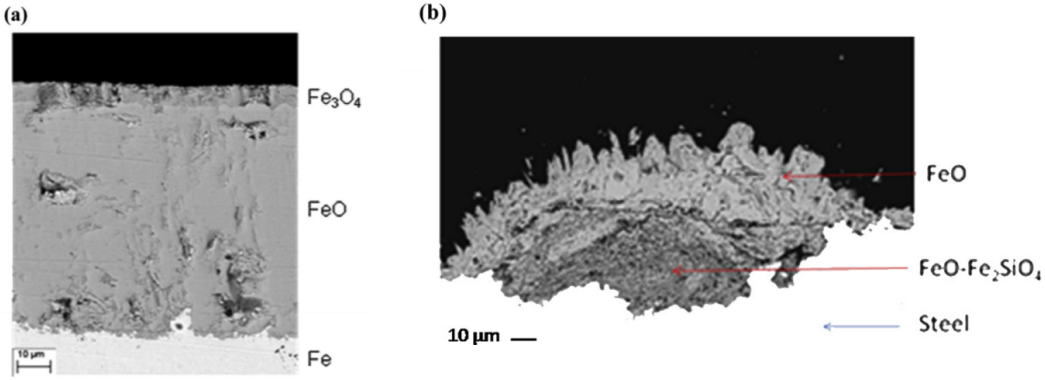

Figure 11: Cross section of steel after oxidation for 15 minutes (a) at 850°C with 0.02% Si content (b) at 1100°C with 3.2% Si content [18]

During the manufacturing of the electrical steel, there is a hot rolling step. In this step, there is a high likelihood of oxidation occurring and the likely result of this could be the formation of iron oxides FeO, Fe_3O_4, and Fe_2O_3 [20]. Due to the silicon content, there can also be creation of fayalite Fe_2SiO_4. No matter which temperature the electrical steel is hot rolled at a layer of iron oxides and fayalite will form [20]. Figure 12 shows an image of electrical steel oxidation at extreme high temperatures.

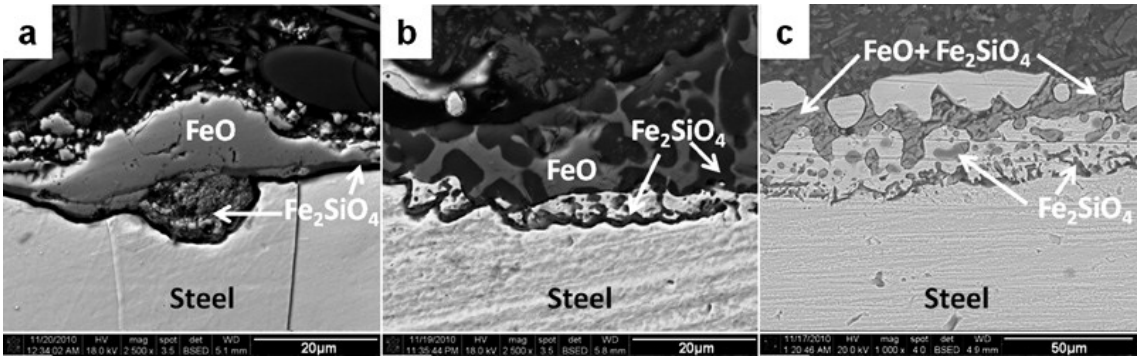

Figure 12: SEM images of silicon steel oxidized for 20 minutes at (a) 950°C (b) 1100 °C (c) 1150°C [20]

2.3 Effects of Punching on Electric Steel

When electrical steel is finished the manufacturing process discussed above, the sheet metal is ready to be molded into its desired shape and size. It is at this point that the roll of the electric steel is cut to the desired shape for use within the machine. The issue is that common cutting processes like laser cutting and punching can create residual stresses at the sight of the cut can lead to premature failure and can also cause some deterioration of magnetic properties [21]. Punching is a very common cutting process for electrical steel due to its cost effectiveness and while it is common practice to punch sheets of electrical steel, it is important to understand what happens during this process and how any disadvantages of the process can be avoided.

The punching process of the electric steel is shown below in figure 13. Here the steel sheet passes above the die, and once the sheet has reached the starting position, the punch comes down to separate the final part from the sheet. Here the punch first meets the sheet and causes it to roll over. The load then increases until the metal yields and fractures. At this part of the process, a crack initiates and then propagates along the punched profile. Here there is a ductile fracture that causes this raised edge or burr to form. The important factor here is that once the electrical steel is punched, it will have a raised edge on the final part [21].

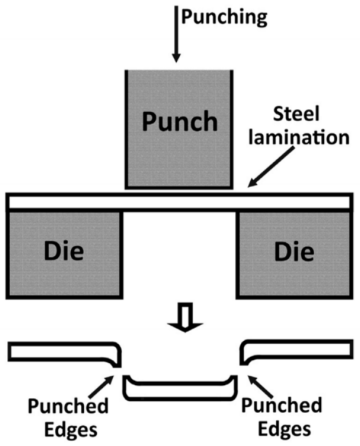

Figure 13: Punching of electric steel sheets showing how a burr is formed [21]

The punching process causes plastic deformation at the edges where the material was cut/separated from the sheet. This damaged region will have a higher hardness due to the residual stress and the work hardening, in addition to the increase of the dislocation density [21]. This will lead to changes in the microstructure that will cause the magnetic properties to deteriorate, as these new dislocations will act as pins that will restrict the movement of the magnetic domains [21]. This plastic deformation is shown below in figure 14, and it shows both how the electric steel's microstructure normally looks and how it looks at the deformed edge of the material.

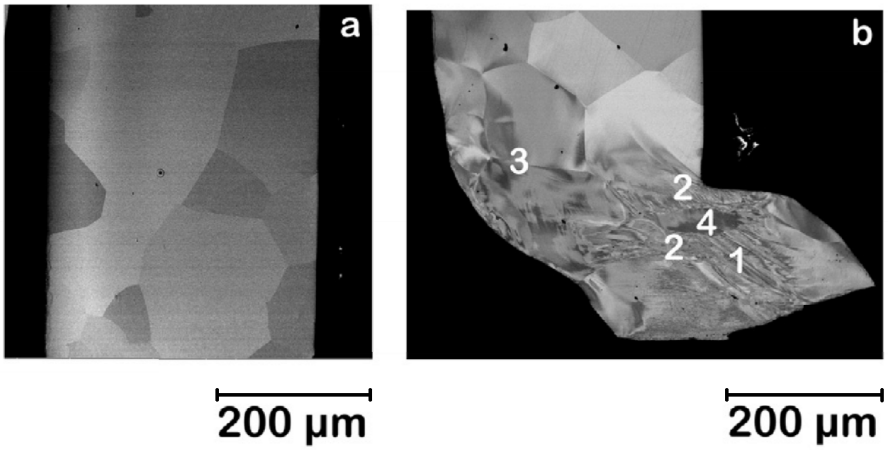

Figure 14: Cross section of M330-35A electric steel (a) away from cutting edge and (b) at the cutting edge. region 1: finer elongated grains, region 2: deformed area where grains are not visible, region 3: bend contours, region 4: un-deformed region [21]

Taking a closer look at figure 14b there is quite a bit of plastic deformation that occurred to punch the electric steel sample. At this region there are crystal defects and deformed grains which results in bend contours within the region of plastic deformation [21]. These bend contours are visible in region 3 as this was the region that stretched and underwent bending during the punching process. Similarly elongated grains are shown in region 1 which is the region that was undergoing shear loading. In regions 2 shear bands are shown forming around regions 4 and regions 1, as this is the region where the microstructure was elongated and constricted. Region 4 is an un-deformed region within the microstructure [21]. Using electron backscatter diffraction (EBSD) from an electron microscope, the crystal structure in this region can be studied. The sample shown in figure 14b was scanned using EBSD and the results for this test are shown below in figure 15.

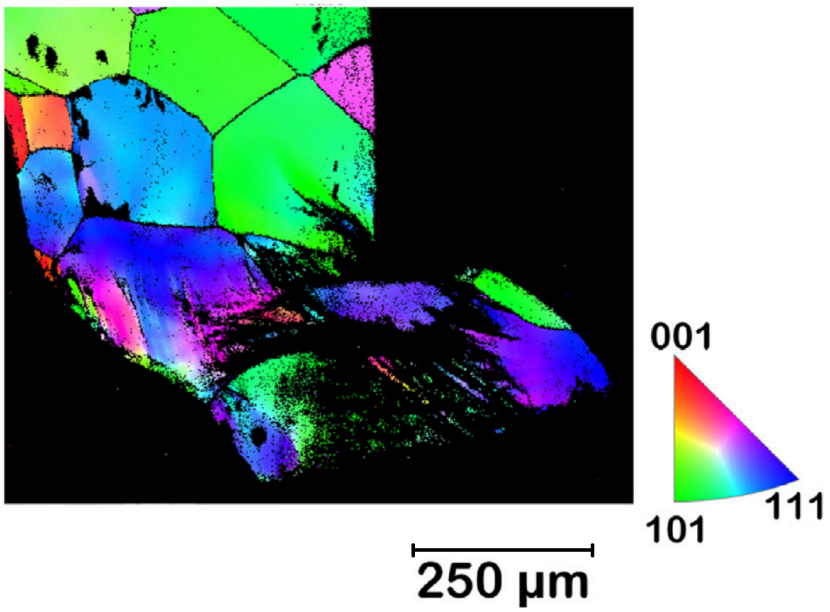

Figure 15: EBSD results on sample shown in figure 14(b) showing plastic deformation (dark areas) and which plane the grains are aligned in [21]

The EBSD data provides useful information as the shear bands are shown much more clearly in figure 15. These areas of plastic deformation show up as black regions within the microstructure. The reason for this is that the quality of the scan worsens as the dislocation density increases in a region as it will distort the crystal lattice to where the data cannot pinpoint a crystal structure from said region [21]. This also indicates that the region of deformation has high strain energy concentrated at the shear bands. These shear bands developed to accommodate the larger strain, and help to understand the mechanism at work during the punching process. Here newer and finer

grains are not evolving throughout the cross section, rather they are forming in between the shear band regions, and remain localized in single grains [21]. For the punching of electrical steel, it is very important that the punch and die have sufficient clearance and tonnage to correctly punch the sample, as not doing so can result in a large burr that can overall increase residual stresses, and decrease the magnetic properties of the motor/transformer [22].

Punching can have a detrimental effect to the fatigue strength of the electrical steel. The punching (or stamping) can cause tensile residual stresses near the cutting edge, that can be as large as 200µm from the cutting edge according to Dehmani et al. [23], even larger at 500µm according to Hongzhi et al. [24] and up to 700 µm from the cutting edge according to Maurel et al. [25]. It is important to note that the residual stress peaks near the cutting edge and tappers as the distance from the edge increases. This variance in the residual stresses can be attributed to the clearance and tonnage of the punching process [22]. The residual stress measurement conducted by Hongzhi et al. [24] is shown in figure 16. This study found the residual stress to peak at 340 MPa right at the cutting edge. Dehmani et al. [23] found that the residual stress peaked to 415 MPa at the cutting edge. This residual stress can reduce the overall life of the sample during fatigue, and must be controlled during the manufacturing process.

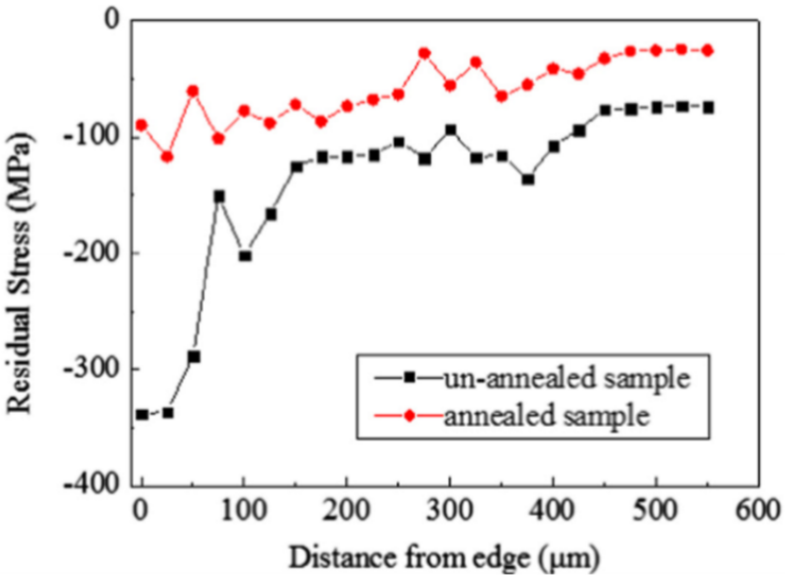

Figure 16: Residual stress measurement near the cutting edge of electrical steel, for an annealed and un-annealed sample [24]

Dehmani et al. [23] also conducted micro-hardness measurements near the punched edge to identify if the grains are hardening due to the applied stress of the punching process. It is known that punching can cause a rough edge as the edge will roll over, and have a shear zone. When the material suddenly fractures, a fracture zone and burr is left over. This fracture zone and burr is a rough surface that can cause stress concentration during cyclic loading, and it is the location where a crack can initiate [23, 26]. The area where the micro-hardness peaks is at the cutting edge where we see the highest residual stresses of electrical steel. Figure 17a below shows that if the sample is polished, the fatigue life drastically improves as it can remove some of the areas of stress concentration and plasticity which reduces the likely-hood of fatigue crack initiation [23, 26]. By polishing the cutting edge, the area of tensile residual stresses are also removed. Annealing can also accomplish this however, to a lesser extent [23, 24]. This study was done on an electrical steel called M330-35A, which has a silicon content of 2-3.5% [23].

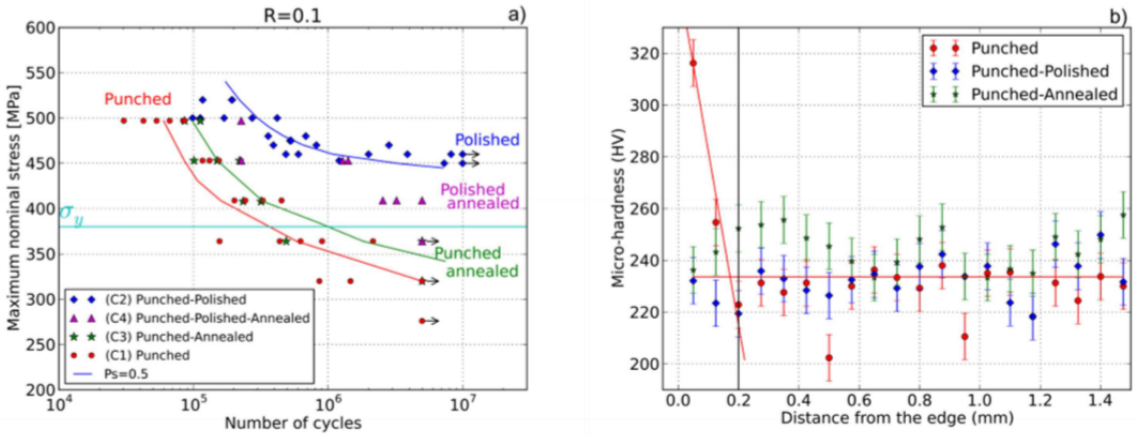

Figure 17: (a) S-N curves obtained for different various specimen configurations of M330-35A (b) micro-hardness measurements for these same specimens [23]

The fatigue cracking of stamped electrical steel initiates from the free surface [27]. According to Du et al. [27] the crack growth does not follow the path that would directly traverse the minimum cross section, and it does not flow in a linear fashion. The crack will start at one corner and follow a trans-granular crack growth and the fracture surface amongst neighboring grains may not be continuous. Figure 18 shows a picture of the fracture surface where the crack initiation is shown below as well as an image showing the fatigue crack growth for the sample [27]. These findings

help to better understand how the electrical steel behaves under tensile stress.

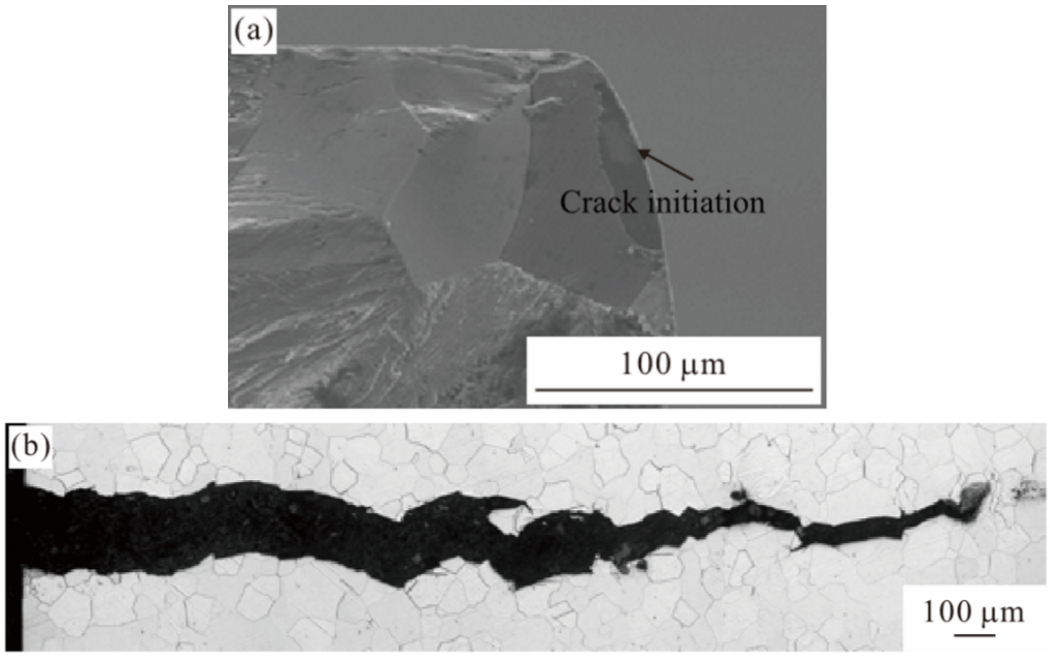

Figure 18: (a) Fracture surface of electrical steel 30WGP1600 (b) crack growth of 30WGP1600 showing the crack initiate from the surface and show trans-granular fracture through grain boundaries as the main crack propagation mechanism [27]

2.4 Joining of Laminated Electrical Steel

The laminated electrical steels used in the application of electric motors, are non-oriented electrical steels. The stator and rotor core are typically made from sheets of thickness 0.2-0.5mm stacked and joined together to reduce the eddy current losses within the electric motor [28]. Electrical steels in this case, non-oriented electrical steels are typically kept below 3 - 3.5 wt% Si as this gives the best magnetic properties [29]. Once the desired profile is stamped, they are then joined together in a stack. These steels are typically clamped and then fastened together by means of either adhesive bonding, mechanical bonding or welding [28]. These different methods are shown below in figure 19.

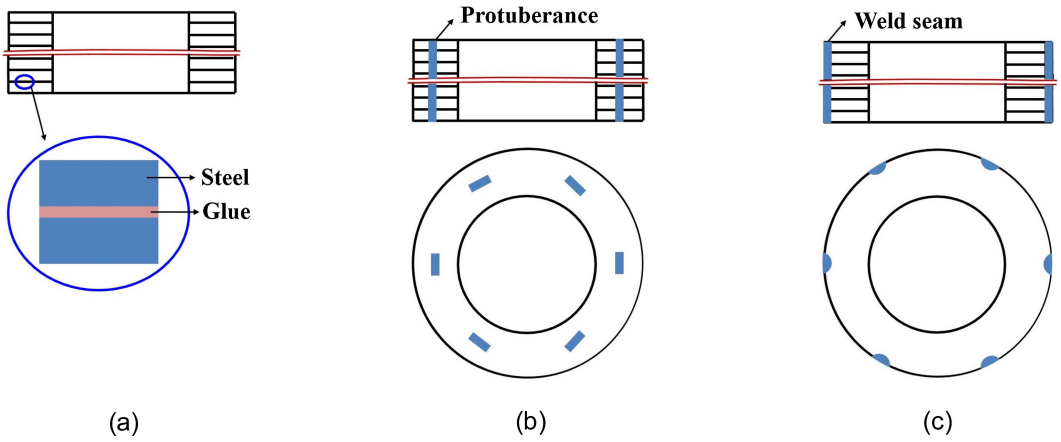

Figure 19: Three joining methods of laminated electric steel: (a) adhesive bonding (b) mechanical bonding (c) welding [28]

Adhesive bonding is a very popular and great way to join the laminated electric steel sheets together for one main reasons. Adhesive bonding yields the best magnetic properties out of the three different joining processes [30]. The reason is that by gluing each of the sheets together, they remain electrically isolated, thereby preventing the eddy currents from travelling between each of the individual laminated sheets. There are however drawbacks to this method. The greatest drawback is the cost as this is the most expensive option out of the three different joining methods [30]. The second issue is that the adhesive does occupy the spaces in between each lamination. As a result, it yields a low stacking factor, and requires more space compared to the other two methods. In the application of modern automobiles, space is limited and as such this is one disadvantage to using this method of joining. The final issue is that this method yields the lowest bonding strength as, under torsional stress, this method fails at the adhesive joints.

Mechanical Joining is another joining method for laminated electrical steels. The sheets in this method are joined by the use of interlocking protuberances [28]. The issue here is that this method can make the assembly quick and cost effective however there is a large deterioration of magnetic properties. This method causes the eddy currents to flow through each protuberance due to the electrical contact and travel between each sheet causing large eddy currents within the stator [31]. This leads to a great loss in energy efficiency and as such, this method is not widely used.

The welding method is one of the most widely used joining method for laminated electrical steels.

It is a sort of compromise between the adhesive bonding and mechanical bonding methods. The laminated steel sheets are clamped together and then welded on multiple different, equally spaced seams [28]. There is however, some deterioration in permeability, and an increase in eddy current losses as each sheet becomes electrically shorted to one-another. However, this method yields the greatest overall torsional strength [28]. It also has the greatest overall resistance to temperature compared to mechanical and adhesive bonding.

Laser welding is a very good automated welding processes, as it can produce good quality repeatable welds. In order to understand the benefits of this process, a relationship must be determined between the weld, and the key magnetic and strength properties of the laminated electric steels. In figure 20, we can see a clear relationship between the torque and the torsion angle of the welded laminations at different welding speeds, determined by Wang et al. [28]. The samples welded at 10mm/s, can endure the greatest torque before failure. At the same torque, these samples also show lower torsional angle. This means that a decrease in the weld speed, leading to greater heat input, results in an overall stronger lamination, and this graph shows this trend [28].

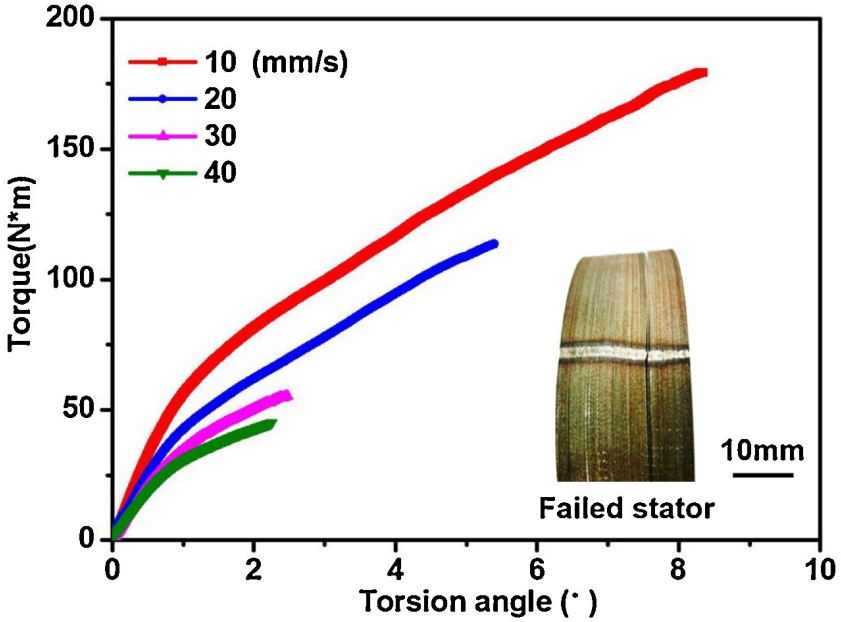

Figure 20: The relationship between torque and torsion angle of laser welded laminations at different welding speeds [28]

To understand the effect of the welding on the magnetic properties, it is important to look at the magnetic properties of the samples shown in figure 20. The resulting hysteresis curves of these samples is shown in figure 21. The sample welded at 10mm/s was shown to have the highest torsional strength of the welded laminated electric steels shown in figure 20. However, this same sample deviates the greatest from the non-welded electric steel samples in terms of the magnetic hysteresis curve, and shows the greatest losses. This is due to the greater heat input creating a greater residual stress and the greater weld dimension causing there to be an increase in the eddy current losses within the welded stack [28].

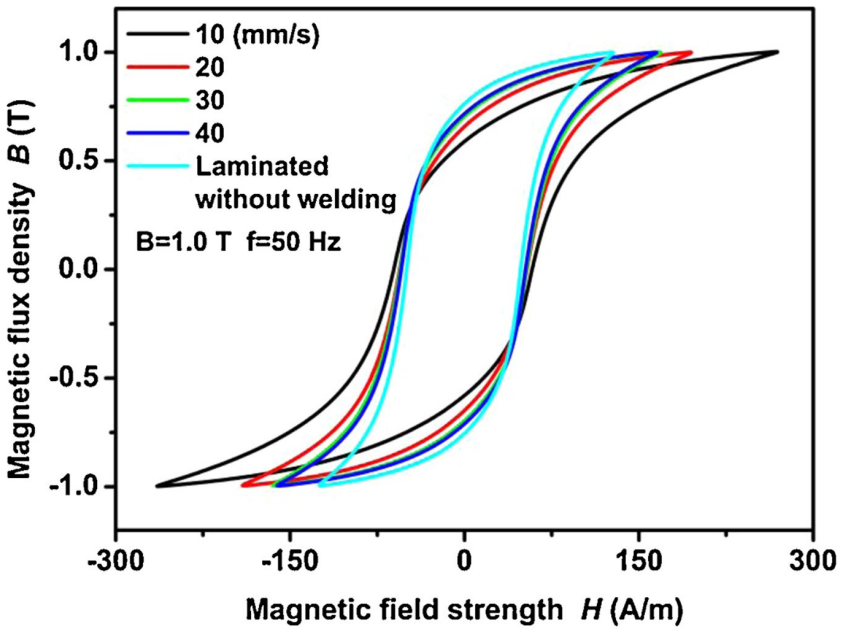

Figure 21: The relationship between welding speeds and the magnetic field strength of welded laminations shown in figure 20 [28]

Figure 22 shows the effect that a weld has on the electric steel. Figure 22a shows the ideal flow of eddy currents. Here, each laminated sheet contains its own internal eddy currents isolated from the adjacent sheets. However, in figure 22b a weld is done on the stack of laminated electric steel. The weld does two things here. Firstly it destroys the insulation layer at the sight of the weld and then the weld seam both physically and electrically joins all of the sheets together. This causes the eddy currents to now travel between each of the sheets. This increase in eddy currents creates an opposing magnetic field which causes the deterioration of the hysteresis curve shown in figure 21.

The greater the weld is, the easier it is for the eddy currents to flow between each of the sheets which further deteriorates the hysteresis curve [28].

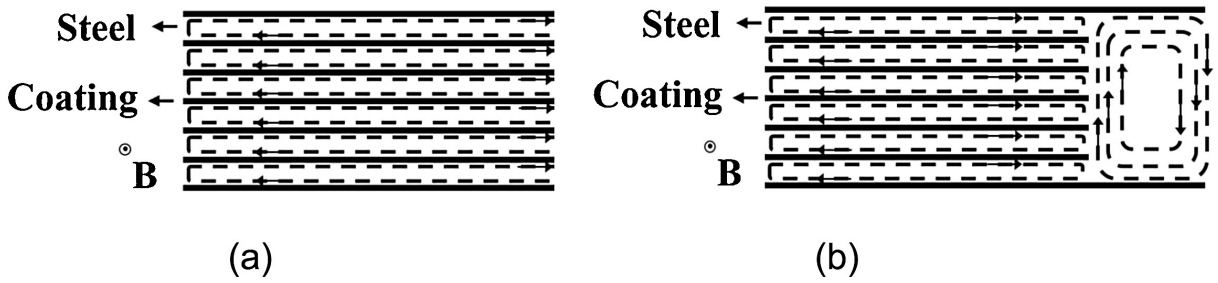

Figure 22: (a) Flow of eddy currents on a non-welded sample (b) flow of eddy currents on a welded sample [28]

In addition to shear strength, an electric motor must have good magnetic properties to ensure an energy efficient motor is produced. In applications where strength is important welding can be done. TIG welded samples and laser welded samples (the two most popular forms of welding for laminated electrical steel) will deviate greatly from the non-welded sample and show a significant deterioration in the magnetic properties [32]. This same trend occurs in the other magnetic parameters where the TIG welded sample has the greatest iron losses, lowest permeability and lowest magnetic flux density. The laser welded sample will also show a deterioration however it will be less than the TIG welded sample and closer to the original non-welded sample [32]. It is for this reason why the adhesive bonding is the ideal choice for the automotive industry as it provides the greatest energy efficiency, even at the cost of torsional strength. It is important to understand the benefits and drawbacks of welding the laminations to understand why gluing the laminations is overall the best choice for automobiles.

Joining the individual layers of electrical steel by adding adhesive layers is very beneficial as it leads to low eddy currents (due to the electrical isolation between each layer) and allows for high efficiency of the motor [33]. The lamination process is preferred for automotive applications for this reason. The preparation of the laminated electric steel is illustrated below in figure 23. The process here is very simple. Firstly, the epoxy varnish is prepared by mixing the epoxy, distilled water, a hardener and emulsifier, and this formulation can vary depending on the type of epoxy varnish used. Next, a very thin layer of the varnish (less than 1 µm) is applied to the electrical

steel sheet. This coating is not very thick and can be up to 20µm in thickness [34]. Currently, laminated electrical steels are bonded using a full-surface coating with varnishes that are based on epoxy resins [34]. This step is normally done at the end of the manufacturing process while the electrical steel sheet is rolled into a coil for stamping. The sheets are then cut to the desired profile and stacked together, where they are cured at a high temperature and under some pressure to ensure the epoxy adheres all layers together, thereby completing the joining of laminated electrical steel [33].

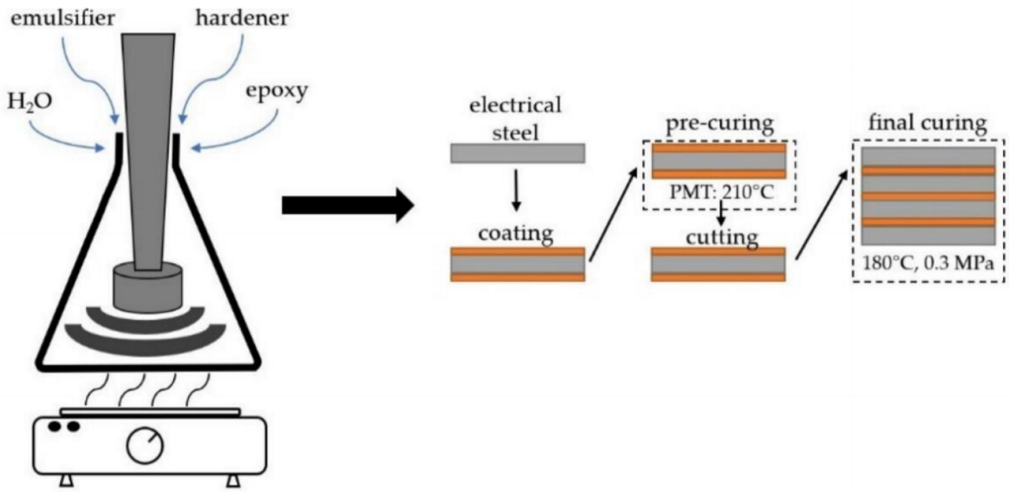

Figure 23: Varnish preparation, electrical steel coating, stacking and lamination process [33]

2.5 Quasi-Static Analysis

In order to understand the various material characteristics and how they factor into the material's strength, it is important to first introduce what the different material properties are and how they are derived from a stress-strain curve. If a specimen is axially loaded, the stress and corresponding strain can be measured and graphed to create an engineering stress-strain curve. This curve can then be used to derive very important elastic material properties such as the elastic modulus, the yield strength and the ultimate tensile strength. Figure 24 illustrates what a typical elastic, engineering stress curve looks like.

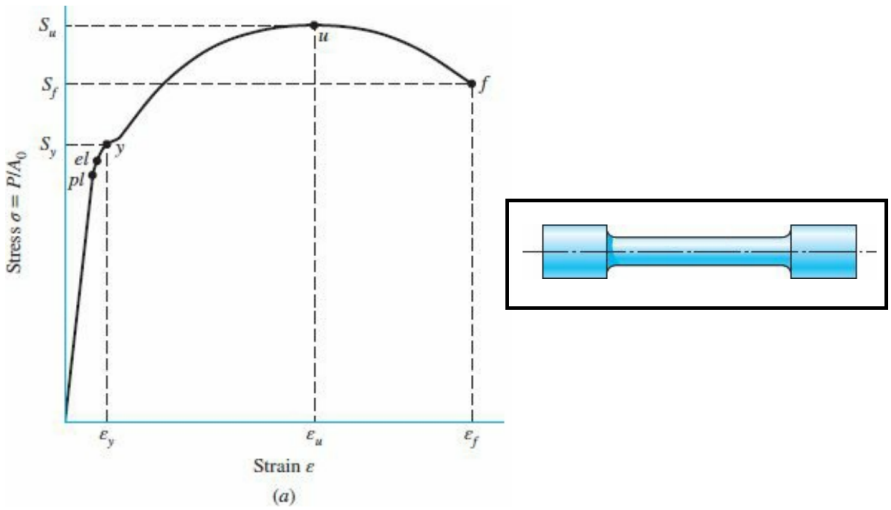

Figure 24: Elastic stress-strain curve [35]

Looking at this curve, we can derive some very important material properties such as the elastic modulus. The elastic modulus is the slope of the stress-strain curve that is derived from the straight line up to the point indicated as pl (the proportional limit) in figure 24. Using this constant, the strain and stress of the material can be predicted using the equation below. This equation is called Hooke's Law [35].

$$E = \sigma\epsilon \tag{1}$$

The yield strength (S_y) is one of the various constants that can be derived from the stress-strain curve above. It is the stress beyond which, the material permanently yields, and can no longer return to a strain value of 0. Beyond this point, the material will leave the region of elastic deformation and enter the region of plastic deformation. The ultimate tensile strength (S_u) is the maximum stress that the material can tolerate and the fracture strain (ϵ_f) is the strain at which the material fractures.

Hooke's Law can help to predict the material behavior in the elastic range however, it is not sufficient in predicting the shape of the stress-strain curve in the plastic region. For this, the Ramberg-Osgood equation is useful in modeling the material behavior up to the ultimate tensile strength. Using the material constants of H as the strain hardening coefficient and n as the strain hardening exponent, it is possible to model the material behavior using the equation below.

$$\epsilon = \frac{\sigma}{E} + (\frac{\sigma}{H})^{(\frac{1}{n})} \tag{2}$$

It is also important to understand the concept of true stress and true strain. They follow the same equations listed above however with one major change. As a material is loaded, the cross sectional area of the material changes, and decreases. Instead of using the initial area A_0, the real (true) area at the corresponding stress value is used, creating a true stress-strain curve. This is shown below in figure 25.

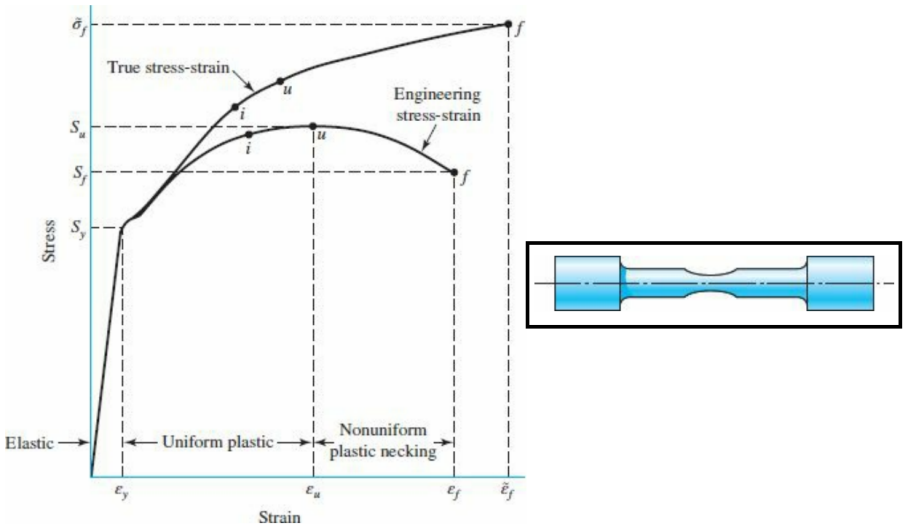

Figure 25: True stress-strain curve [35]

Looking at this figure, some of the key concepts such as the elastic modulus and yield strength remain constant. The main difference here is that the true ultimate tensile strength changes and increases to take into account the true strain of the material. Knowing these key concepts helps to understand the quasi-static analysis that is conducted in this research.

To conduct a quasi-static test, the test setup must follows ASTM E8 [36] and ASTM E345 [37]. These are guidelines set by the American Society for Testing and Materials (ASTM) and they outline what shape the specimen should follow and what parameters the test should follow. ASTM E8 outlines a general guideline for conducting the tensile testing but ASTM E345 is more specific for very thin materials, such as electrical steel. These standards outline valuable information as to how values such as yield strength, elongation and reduction of area are to be calculated. The sample geometry required is shown in figure 26, following the type A dimensions outlined in ASTM E345. According to ASTM E345, the strain rate to determine the yield strength must be 0.002 - 0.010 mm/mm/min.

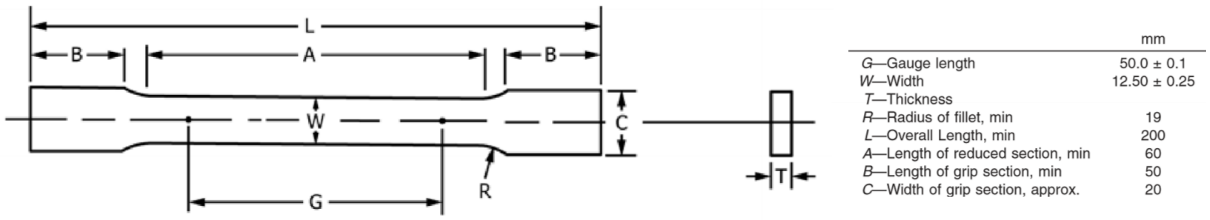

	mm
G—Gauge length	50.0 ± 0.1
W—Width	12.50 ± 0.25
T—Thickness	
R—Radius of fillet, min	19
L—Overall Length, min	200
A—Length of reduced section, min	60
B—Length of grip section, min	50
C—Width of grip section, approx.	20

Figure 26: Tensile test specimen geometry according to ASTM E345 [37]

2.5.1 Quasi-Static Behavior of Electrical Steel

Figure 27a shows a stress-strain curve of an electrical steel containing 3.3% Si content. This study was done by Bode et al. [38], where he found that under quasi-static loading, the specimens undergo a ductile failure and show some global necking (see figure 27b). However, plastic deformation under a load appears to take place at shear bands, as this is where plastic strain accumulates and cracks initiate. Under quasi-static loading, the main failure mechanism was found to be trans-granular cleavage facets shown in figure 27c. This is the same failure mechanism that appears in electrical steel whether the cutting method is stamping, CNC machining or abrasive waterjet cutting [39]. Looking at the stress-strain curve in figure 27a the fracture strain is approximately 16.5% and the ultimate tensile strength is close to 1.3 normalized stress. In this study, the stress dipped downwards after reaching the yield strength and then follows a normal stress-strain curve shape. These findings are very important and provide a great baseline as to what behavior can be expected from the samples in this research.

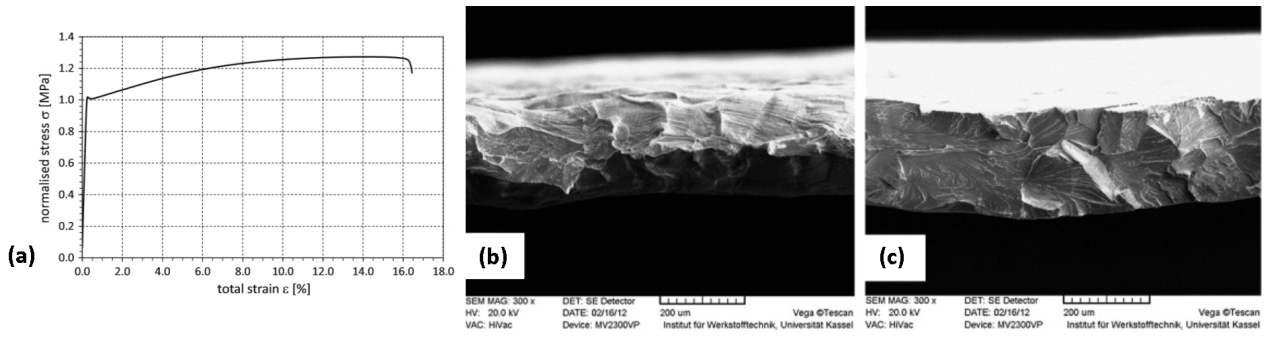

Figure 27: (a) Stress-strain curve for electrical steel with 3.3% Si content (b) fracture surface after test showing local necking and (c) trans-granular cleavage facets [38]

A study was conducted by Schayes et al. [40] where a 2.9% Si electrical steel was tensile tested.

The resulting stress-strain curve from this analysis is shown below in figure 28. Here the sample had a higher fracture strain at 28% and had a ultimate tensile strength of 1.36 normalized stress which is comparable to the study done by Bode et al. [38]. The curve in this study followed the same stress dip downwards after the yield stress seen in figure 27 above. This study also measured the grain size of their material to around 75µm and an image of the microstructure is shown in figure 29a. The grain size distribution of this alloy is shown in figure 29b, and this shows that the grains can be quite large in electrical steel.

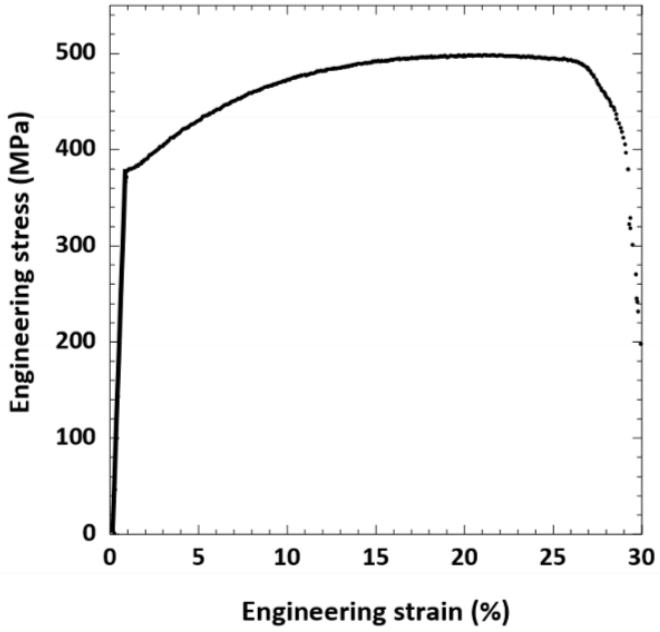

Figure 28: (a) Stress-strain curve for electrical steel with 2.9% Si content [40]

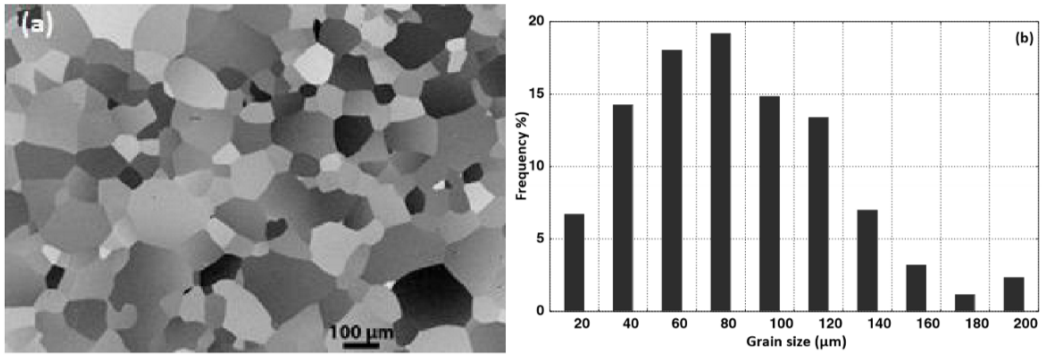

Figure 29: (a) Microstructure of Fe-3Si electrical steel (b) grain size distribution of the electrical steel [40]

A study was done by Fortese et al. [41] where tensile tests were conducted on a non-oriented electrical steel called NO20-1200 at room temperature, 100°C and 150°C, with the samples oriented in the rolling direction. The study found a decrease in the elastic modulus at 100° by 6.4% and at 150° by 4.4% relative to the room temperature results. When comparing the yield strength, a decrease of 12.7% was seen at 100° and a decrease of 15.3% was seen at 150° [41]. In literature there is little information regarding the quasi-static properties of electrical steel at higher temperatures. This is important information needed to design using electrical steel and is the motivation for the research conducted as there is no information available related to the failure mechanism or how the high temperature affected the ductility of the material.

Electrical steel has relatively large grains, and sometimes there may only be 2-3 grains along the thickness of the sample as shown in figure 14a. The large grain size is of a similar magnitude to the sheet thickness. A study was conducted by Henning et al. [42] where tensile tests were conducted on electrical steel sheets that had 3% silicon content. This study incrementally loaded the sample and after each strain increment, analyzed the sample for slip bands and grain orientation. It was found that grain hardening zones originated from grain boundary triple points rather than at grain boundaries. Since the grain sizes are very small, it can lead to local in-homogeneity. Another finding is that even though the grain size is very large with respect to the thickness of the sample, elastic anisotropy cannot be neglected as the shear bands aligned in the loading direction. This study found that the grain that hardened first, was not necessarily the point at which the sample will fail. Grain B for instance in figure 30a at 1.5% plastic strain, showed the greatest hardening however, its deformation rate changed and the failure occurred at the triple point next to grain C. This is shown in figure 30f, 31e and 31f as this is where the sample experienced necking. This is because grain C had the higher deformation rate, which caused it to harden more than grain B, and fail. These are important findings for electrical steel as it is important to understand the effect of the grain sizes on the failure mechanism [42]. This study however, does not account for the change in the mechanism at higher temperatures as the local grain hardening and hardening rate behavior can potentially change at a higher temperature. Understanding the effect of the higher temperature is of key importance to the automotive industry as it is important to understand how the microstructure will behave at a higher temperature and under a load. This is a motivating factor in this research.

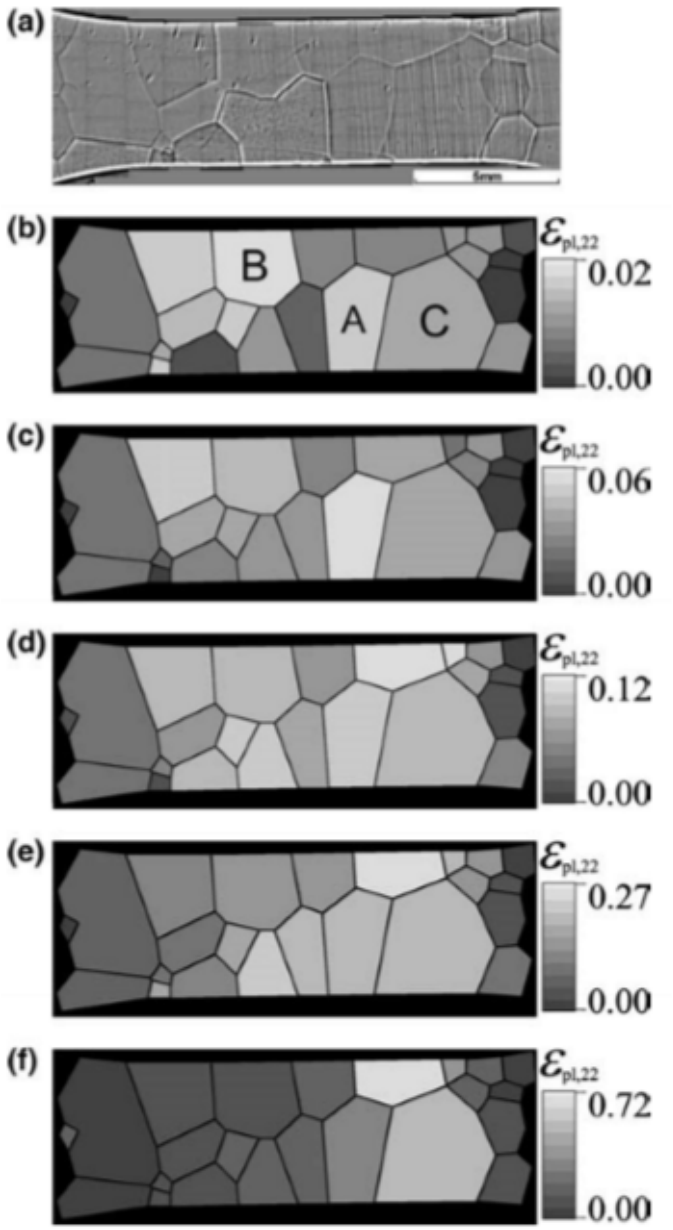

Figure 30: (a) Light-optical micro-graph of the sample before the test. Plastic strain component in axial direction of the least-square fit strain tensor for each grain for (b)–(f) 1.5%, 4%, 10%, 19.5%, 40%. The shape change of the grains is not reflected. [42]

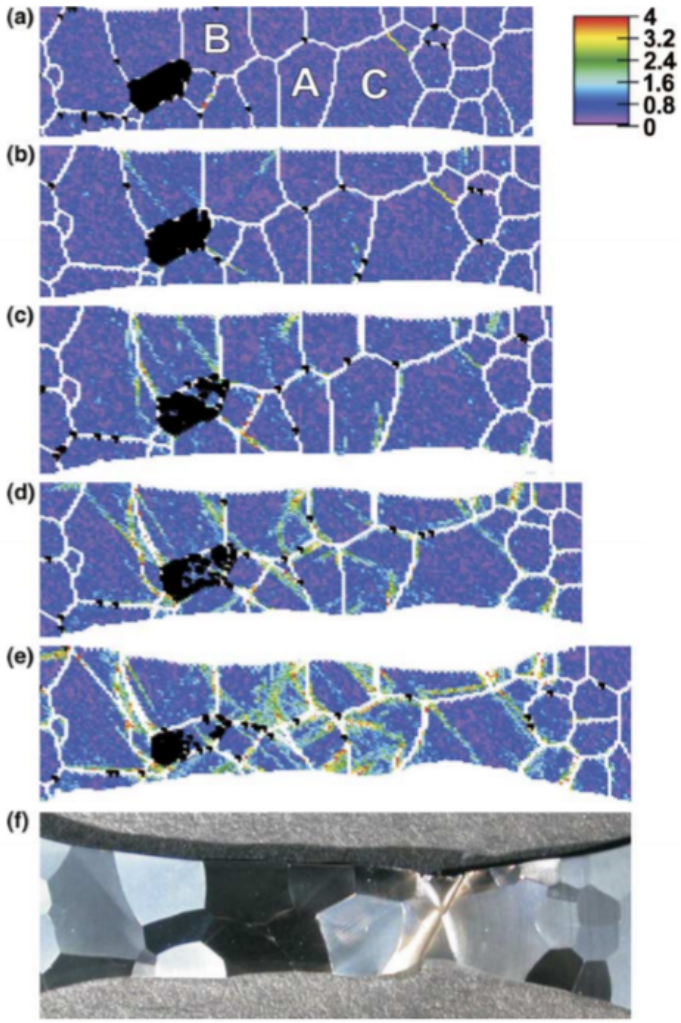

Figure 31: (a)–(e) Grain orientation gradient for plastic strain 0%, 1.5%, 4%, 10%, 19.5%. The regions in black indicate failure of automatic orientation estimation. (f) Optical photograph of the sample with 40% plastic strain showing necking. [42]

Since the electrical steel is manufactured using a rolling process, the mechanical properties can be anisotropic. This means that values such as yield strength and tensile strength vary based on the direction that the sample is oriented. Figure 32 is an illustration prepared by Vandenbossche et al. [43] which shows how the mechanical properties can vary for electrical steel, where the highest strength is seen at the 90° direction. An in-depth study on the effect of the sample orientation and its relation to the mechanical properties of electrical steel has been conducted by a colleague Tolofari et al. [44] to compare the effect of sheet thickness and cutting direction.

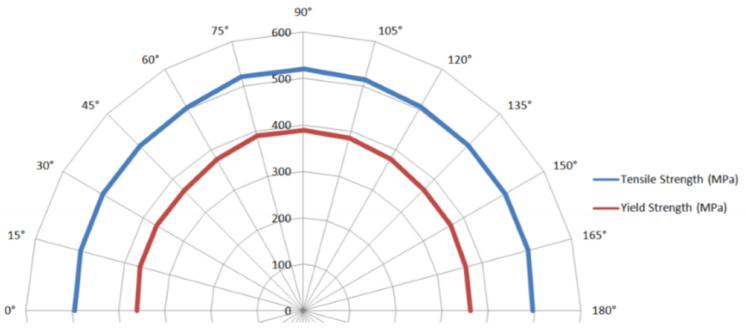

Figure 32: Anisotropy of the mechanical properties of electrical steel [43]

2.6 Cyclic Loading (Fatigue) Analysis

In machines, parts often face cyclic loading, which is variable repeated loading. Even if the stress is below the yield stress, under the right conditions the part in question can still fail due to damage accumulation. This is why it is important to understand the effect of fatigue loading on a part to ensure that the part does not fail under its operating conditions. This section will summarize the stress-based approach to fatigue analysis.

Below in figure 33 is an illustration of a constant amplitude loading on a sample. σ_{max} is the maximum stress and σ_{min} is the minimum stress. σ_a is the stress amplitude, σ_r is the stress range and σ_m is the mean stress. T is the period or the time needed to complete one cycle however, more often the frequency (which is the inverse of the period) is used to indicate the number of cycles completed in a certain time.

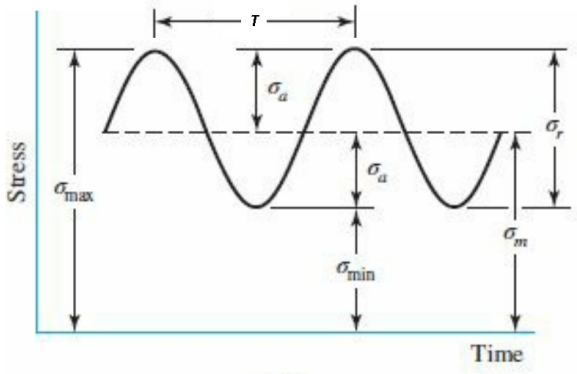

Figure 33: General constant amplitude loading [35]

When a sample goes under fatigue testing, the main parameter that is often provided is the stress amplitude, frequency, and the R ratio. The R ratio is given by the formula below and helps to calculate and consolidate what the maximum and minimum stress is, in relation to the stress amplitude.

$$R = \frac{\sigma_{min}}{\sigma_{max}} \tag{3}$$

Running a test will help to produce a stress-life curve, which is often referred to as an S-N diagram. Below is a characteristic S-N diagram shown in figure 34. Under 10^3 cycles, the region is considered the low cycle region and above 10^3 cycles is the high cycle region on the S-N diagram [35]. There is also important stress values such as S_f which is the fatigue stress or cyclic stress that the sample was tested at, and S_e which is the endurance stress, below which some samples will not fail for an infinite number of cycles.

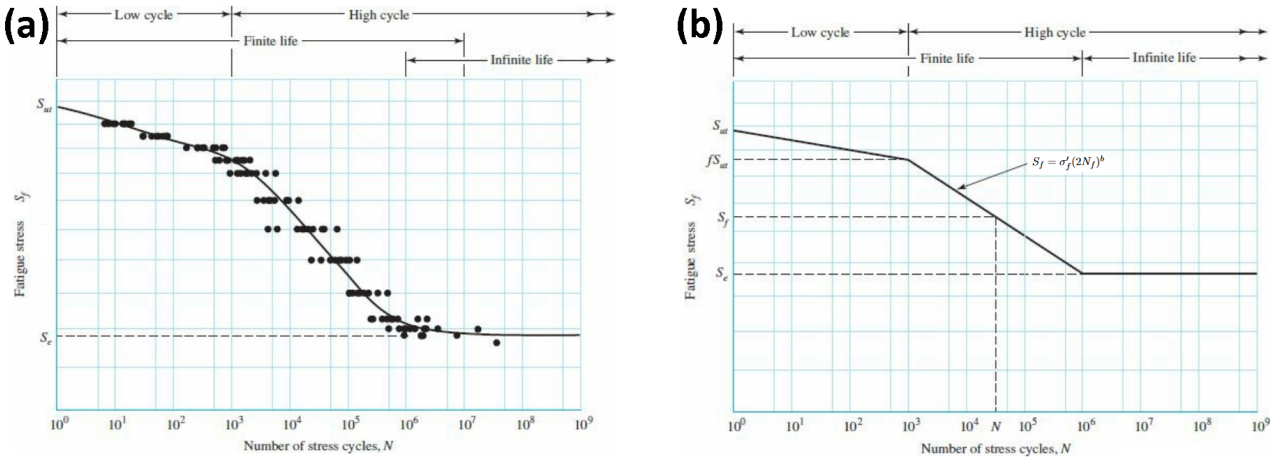

Figure 34: Characteristic S-N diagram (a) plot of sample results (b) resulting line of best fit in results [35]

After a cyclic test is complete, the S-N curve will look like this for a normal steel (the shape may vary for different materials). Using this data, an idealized curve for the material can be made. This is called the Basquin model [45] and is shown in figure 34b. Outside the low life region and within the finite life region of the graph, a linear relationship can be approximated.

The Basquin model is a line of best fit using the following equation, where σ'_f and b are constants,

and N is the number of cycles [35, 45]. The Basquin model is a statistical analysis that assumes a linear relationship between the log of the number of cycles and the log of the fatigue stress, and determines the values of the coefficients of σ'_f and b using a linear regression model that assumes a 50% confidence and reliability interval [45]. After the Basquin model has been derived, the material's life can be accurately estimated under a specified stress amplitude.

Basquin Model

$$S_f = \sigma'_f (2N_f)^b \tag{4}$$

In order to account for the mean stress effect, the Smith Watson Topper mean stress correction is employed. This equation applies a mean stress correction and transforms the results into an equivalent fully reverse stress (σ_{ar}) results (R = -1) [46].

SWT Mean Stress Correction

$$\sigma_{ar} = \sqrt{\sigma_{max}\sigma_a} \tag{5}$$

Once the SWT mean stress correction is applied, design curves can be generated to account for the level of desired reliability and confidence. Owen's [46] design curve is one of the automotive standard methods for generating design curves. The Basquin model is the estimated mean (50% reliability, 50% confidence) curve for the fatigue data. The Owen's [46] Design curve follows the same slope, b, as the Basquin model however, the coefficient $\sigma_f{}'$ is adjusted for the specified confidence level and reliability [46]. The design curve equation is given below. where, $\sigma_{a,RC}$ and $\sigma'_{f,RC}$ are stress amplitude and fatigue strength coefficient for the given reliability (R) and confidence level (C). In this thesis, a 90% reliability and confidence interval will be used.

$$\sigma_{a,RC} = \sigma'_{f,RC}(2N_f)^b \tag{6}$$

The stress-life approach is the approach that will be used in the analysis of electrical steel. There is however, two other common methods to analyze fatigue such as the fracture mechanics method and strain-life method. Fracture mechanics is a field of solid mechanics that studies the propagation of cracks [35]. The theory here is that micro-cracks exist at the beginning of the samples life that eventually propagate through the sample, at which point the sample fails. This method relates the crack length to the number of cycles rather than stress. The reason this method cannot be used for electrical steel is that the crack propagates very quickly and there is a small difference

between the life at which an initial crack is visible, and the life at which the sample fails as per testing done by Dehmani et al. [47]. The strain based method is different than fracture mechanics as it relates the strain of the sample to the number of cycles rather than the crack length [35]. A fatigue failure almost always begins at a notch, crack, or other area of stress concentration. When the stress at this region exceeds the elastic limit, plastic strain will occur, and since the applied strain is cyclic, cyclic plastic strains must exist, as well as elastic strains [48]. The strain-life method evaluates both elastic and plastic strains in the localized area of stress concentration. This method provides a lot of useful information in evaluating the damage that accumulates over the life of the sample. The samples were very thin in this analysis, and because of this, they can be susceptible to buckling in a strain-controlled test, this is why the strain-life method was not chosen.

To conduct the fatigue testing the ASTM standard E466 is used [49]. This standard specifies the general guidelines to follow when conducting the fatigue testing. It specifies that the frequency of the test should be in general between 10^{-2} to 10^{+2}. The specimen geometry that is needed for a fatigue test according to this standard is shown below in figure 35. The radius selected was 90mm and the width was set to 10mm for the fatigue testing. The detailed drawing for the sample is shown in figure 47 in section 3.3.

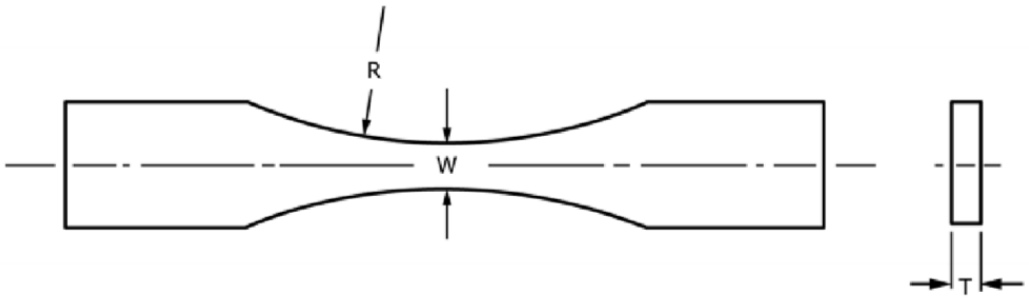

Figure 35: Fatigue test specimen geometry according to ASTM E466 [49]

2.6.1 Fatigue Behavior of Electrical Steel

The fatigue data for a 3.3%Si electrical steel gathered by Bode et al. [38] is presented below in figure 36. This study compared punched and polished samples to see the effect of different surface finishes on the fatigue results. The maximum normalized stress amplitude that the samples could tolerate was 0.42 and the sample appeared to reach run-out at 0.3 for the punched samples. How-

ever, the polished samples could tolerate a higher normalized stress amplitude above 0.44 and could achieve run-out above 0.38 normalized stress. This is due to the induced stress concentration that occurs at the cutting edge which can lead to shorter life for the samples. Various studies confirm that a decrease will occur in fatigue life for punched samples compared to polished samples [26, 50]. The study found that the crack for the punched samples initiated from the cutting edge where the surface was rough. For the polished samples, they found that the crack initiated from a surface defect, and found that the main failure mechanism was cleavage facets [38].

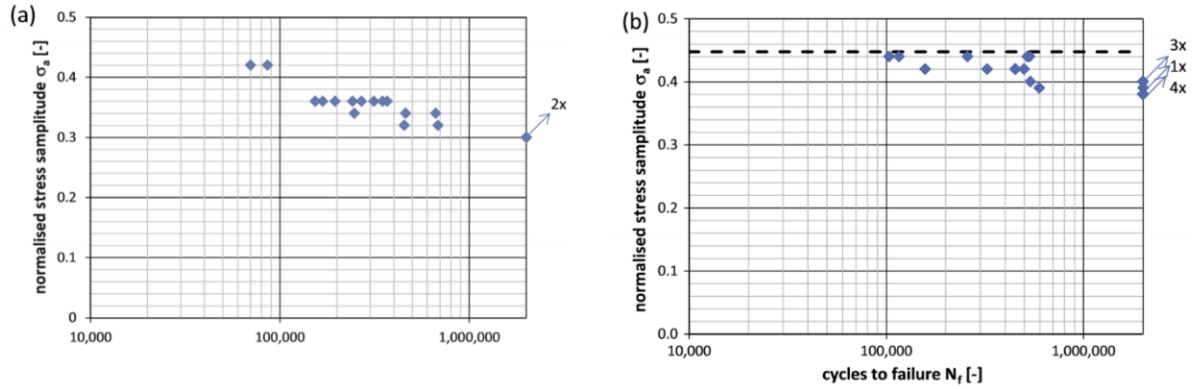

Figure 36: S-N curve normalized to the yield strength, stress amplitude versus number of cycles, for (a) polished sample (R = 0.1) and (b) punched samples (R = 0.005) [38]

Punching is a very cost effective and popular way to cut electrical steel. Below is a picture of the cutting edge of an electrical steel sample, shown in figure 37. This shows the four zones that can be found on the cutting edge, the rollover, shear, fracture zone and burr. According to Dehmani et al. [47], the fatigue crack always appeared in the fracture zone on the cutting edge of the samples, which is due to the stress concentration caused due to the local deformity.

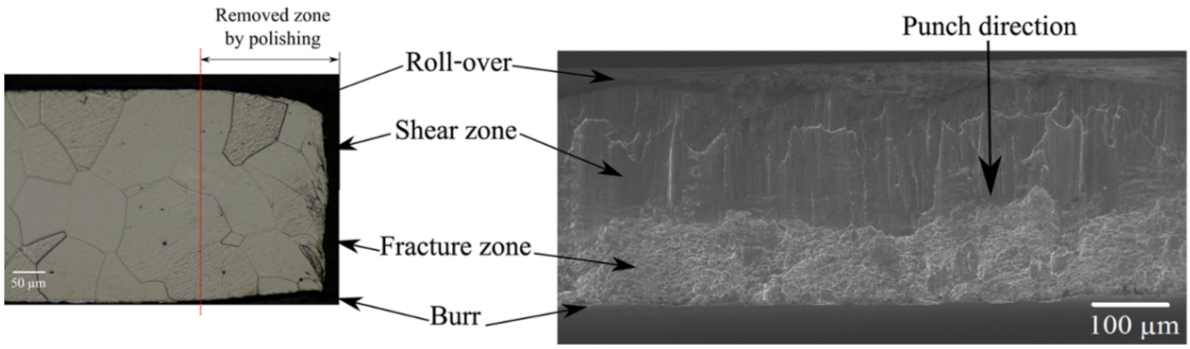

Figure 37: Labeled diagram of the punched edge of an electrical steel sample [47]

Schayes et al. [40] found that the main failure mechanism was a mixed cleavage facet type of failure at room temperature. An in-depth analysis was done on the strain to see how the failure mechanism changes. This study found that in low cycle regime, the crack initiation was trans-granular as shown in figure 38a. This failure mechanism then transitioned to inter-granular cracks at around 1% strain (figure 38b). The study then found that once the sample reached the critical crack length, the sample had a brittle fracture with a wavy fracture surface shown in figure 38c. This is a very important study as it shows in great detail the different failure mechanisms of electrical steel.

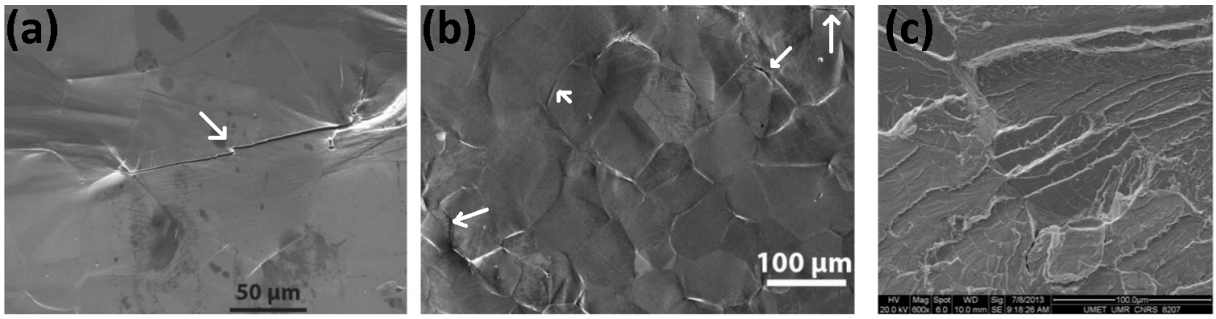

Figure 38: SEM image of the fracture surface at (a) 0.5% strain, where trans-granular crack initiation is found (b) 1% strain where inter-granular crack initiation is found and (c) above 1% strain where brittle crack propagation occurs. [40]

In terms of the crack length as a function of the number of cycles of a sample, Dehmani et al. [47] found that there is only a small difference between the initial crack and the failure of the sample. Figure 39 shows the growth of the crack is very fast for the electrical steel samples [47, 27]. It is for this reason that fracture mechanics is not the ideal choice to quantify the fatigue behav-

ior of electrical steel, and why the stress-based approach was chosen for this material. This is an important finding as it shows that the critical crack length is quite small, and it propagates suddenly.

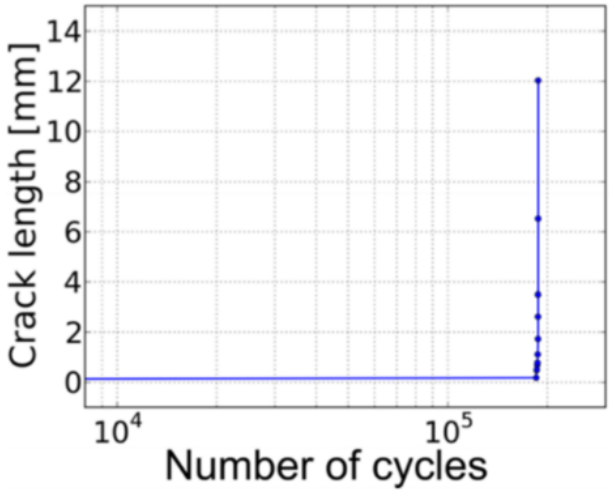

Figure 39: Crack length of stamped electrical steel M330-35A as a function of number of cycles, fatigue tested at room temperature, R = 0.1, 64Hz, Nf = 187,595 [47]

Aluminum nitride is a common impurity that can come in the electrical steel as it is used to control secondary re-crystallization [6, 7]. However, this impurity can also act as a point of stress concentration where a crack can initiate as shown in figure 40 [38, 27]. It has a high melting temperature of 2800°C and if it is present during the heat treatment, then it cannot be removed and often remains in the grain structure [38]. This point was mentioned above in section 2.2 and it is important to understand this as it can be a point of crack initiation for secondary cracks, leading to an overall shorter life of the electrical steel.

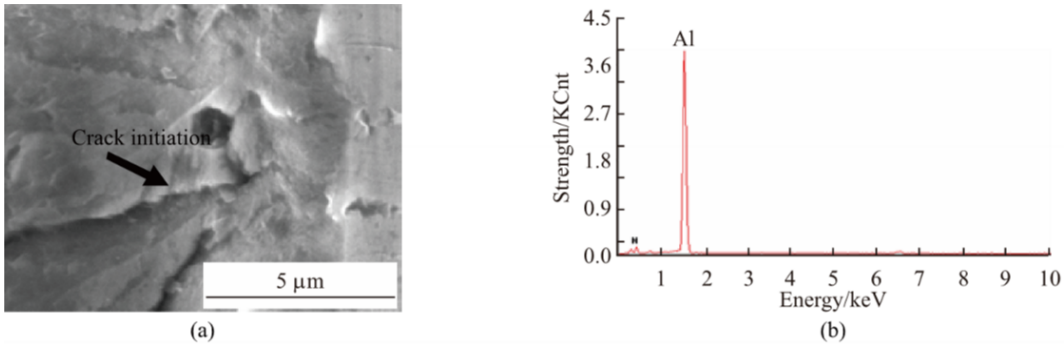

Figure 40: Fatigue sample of 30WGP1600 with Nf = 62400 cycles (a) fatigue crack initiation from a surface inclusion (b) energy spectrum of inclusion indicating that this inclusion is aluminum nitride [27]

There is little literature regarding the high temperature fatigue behavior of electrical steel. Dehamni et al. [47] conducted a study to compare sample life for electrical steel samples at both 20°C and 180°C to see the effect of higher temperatures on the life of the samples. The results of this testing is shown below in figure 41. It shows that there is a measurable decrease in the life of the samples at 180°C. One of the motivations for the fatigue research is a deeper understanding in the fracture surface that results from the higher temperature, as this is missing from this study. This is a goal of this research, to conduct an in-depth analysis on the fracture surface at high temperature to see the difference in the failure mechanisms of the electrical steel and to see how the material is behaving at the higher temperatures. This is critical knowledge needed for the design of electric motors as they can, under a high load experience high temperatures over their life.

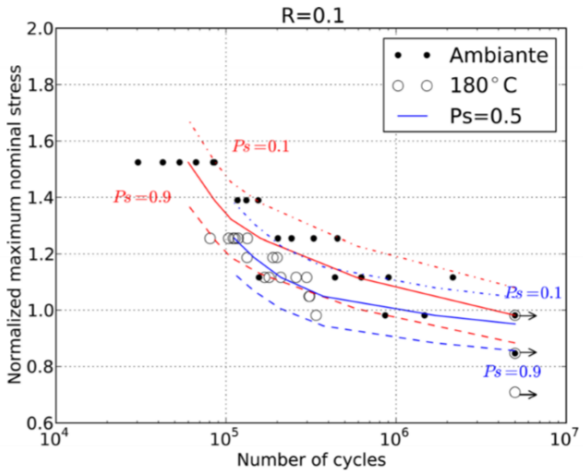

Figure 41: Stress-life curves for electrical steel recorded at 20°C and 180°C [47]

Chapter 3: Methodologies

This chapter will discuss the steps take to do the microstructural analysis of electrical steel as well as the methodologies used to conduct the mechanical characterization of the electrical steel sheets. This chapter will detail the parameters used in the microstructural analysis conducted (scanning electron microscope setup and micro-hardness setup), the parameters used in the quasi-static testing and the fatigue testing parameters.

3.1 Material Characterization

The scanning electron microscope (SEM) used is the Zeiss LEO 1530 FE-SEM with EDX and EBSD, where the images were captured at up to 300X magnification. This scanning electron microscope is shown in figure 42. This is the setup that was used to take a close up pictures of the fracture surfaces for the quasi-static and fatigue samples. To obtain the micro-graph of the electrical steel the samples were first mounted, and then prepared by grinding and polishing the conductive hot mounted sample up to 1 m using diamond suspension. A 5% Nital solution was used to etch the samples to reveal microstructure under the SEM. For some of the images, an optical microscope (OM) was also used. This is the Keyence VK-X250 confocal microscope. It has a resolution of 0.5 nm (height), by 1 nm (width) and is shown below in figure 43. The SEM was not only used to visually examine the surface of the samples, it was also used to calculate the area reduction of the single sheet samples.

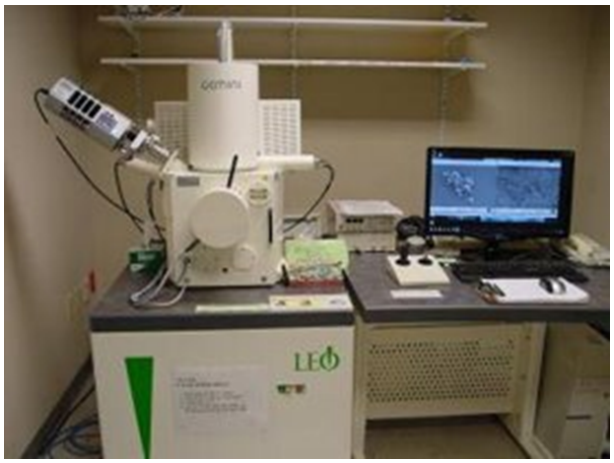

Figure 42: Zeiss LEO 1530 FE-SEM

Figure 43: Keyence VK-X250 [51]

The SEM images were used to measure the final area and calculate the area reduction of the sample as per ASTM E345 [37]. Using the scale on the images, the software ImageJ was used to calculate the final surface area on the cross section. This is shown below in figure 44. The initial area was approximated as the width multiplied by the thickness of the sample in gauge section, measured before the test started.

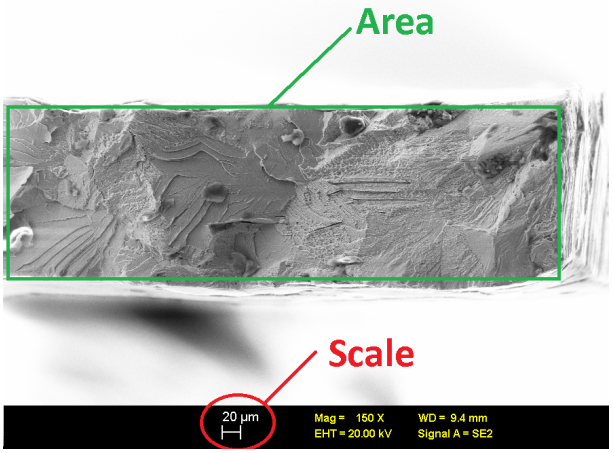

Figure 44: Measurement of final cross sectional area using ImageJ

The microhardness was measured using the Clemex CMT (version 8.0.197) with an indentation load of 100 gf and a 10 s dwell time, by following ASTM E384 standard [52]. The micro-hardness was measured to measure the local grain hardening near the cutting edge of the electrical steel samples.

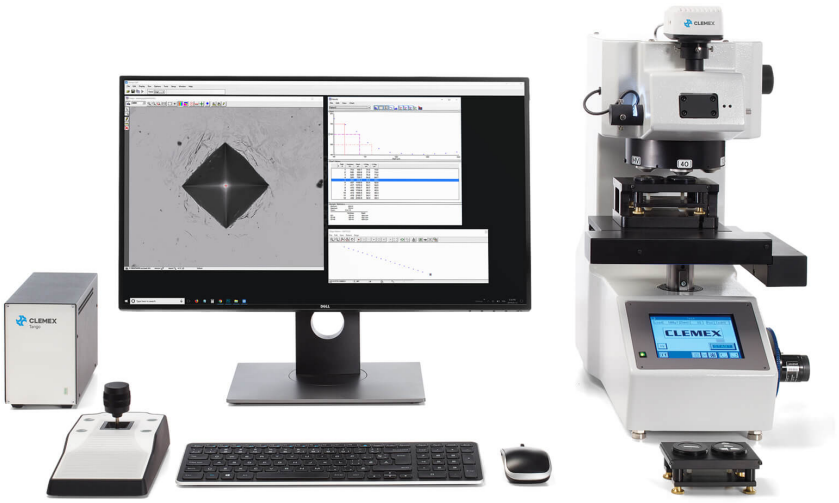

Figure 45: Clemex CMT (version 8.0.197) [53]

3.2 Mechanical Characterization

3.2.1 Quasi-Static Testing Method

Room temperature quasi-static and fatigue testing was conducted on Instron 8874 servo-hydraulic load frame, shown in figure 46b. Quasi-static tests were performed in displacement-control mode at a displacement rate of 1.2 mm/min. The strain was measured using the Aramis/GOM DIC system equipped with two high-resolution CCD cameras of 5M pixels and a maximum frame rate of 15fps. The high-temperature tests were conducted at 150°C using the Instron environmental chamber (Model 3119-609), shown in figure 46a. The temperature of the sample was confirmed to be 150°C by using the Extech 42510A infrared thermometer, which has a repeatability of ±1.8°C. The samples were first set in the chamber and were given one hour before the test was conducted to ensure that the sample reached 150°C and to ensure that all samples were given the same time regardless if they are laminated or single sheet samples. The test setup follows ASTM E8 [36] and ASTM E345 [37] however, the geometry does not as explained below in section 3.3.

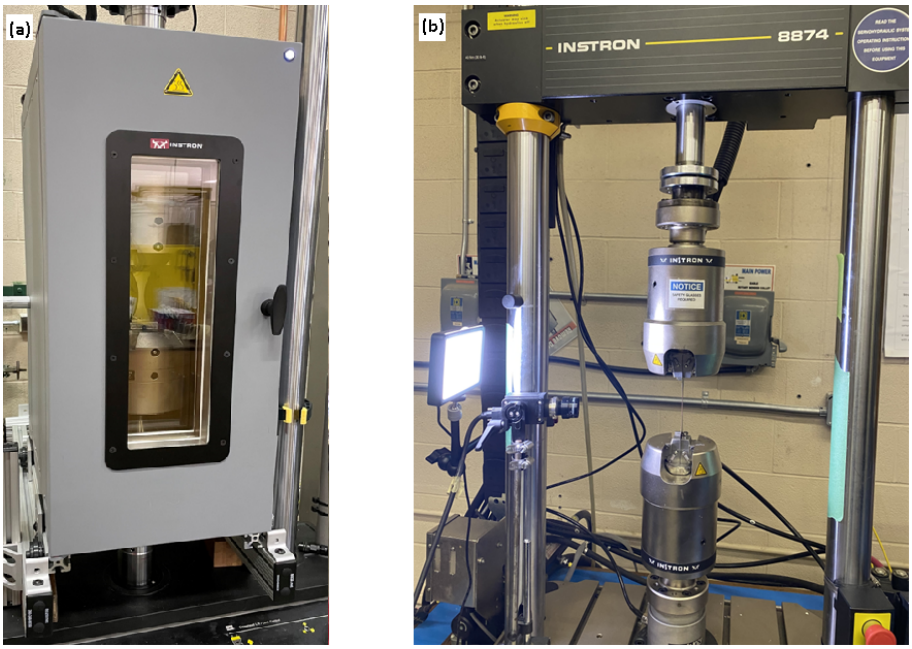

Figure 46: MTS 810 with Instron environmental chamber (a) and Instron 8874 (b)

3.2.2 Fatigue Testing Method

Uniaxial fatigue tests were conducted in force-controlled mode using the hydraulic machines shown in figure 46, with an R-ratio of R = 0.1, using a sinusoidal waveform and varying frequency from 0.5 Hz to 10 Hz, depending on the load level. Tests were stopped after two million cycles and were considered run-out. The Aramis/GOM DIC system was used for fatigue crack detection to better understand the fracture surface when examining it under the scanning electron microscope (SEM). The testing follows ASTM E466 for fatigue testing of metal sheets [49].

3.3 Sample Preparation

The electrical steel sheet samples shown in figure 50 are the samples that have been used in this testing, which were provided by the sponsor company. This sample geometry is used for both the quasi-static testing and the fatigue testing. The first set of samples are the single sheet samples, which are dog bone samples. This material is an electrical steel with a thickness of 0.27 mm. The second set of samples were the laminated electrical steel samples. These samples are made of the same material however, these samples are comprised of 8 single sheets stacked and laminated together. The sample geometry for quasi-static and fatigue tests is shown in figure 47. All of the samples were provided by the vendor in as-stamped form, in the rolling direction.

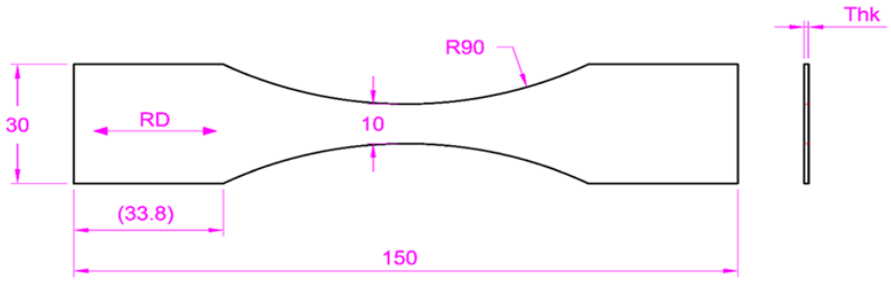

Figure 47: Sample geometry used for both the single sheet samples and the laminated samples. Thk = 0.27mm for single sheet samples, Thk = 2.16mm for laminated samples

It is important to note that the geometry for the samples follows the ASTM E466 standard [49] for fatigue testing of metallic sheets, however, this geometry does not comply with quasi-static testing standards, i.e., ASTM E8 [36] and ASTM E345 [37]. This is illustrated in figure 48. The sample geometry was consolidated to ensure only one die was needed to produce all the samples needed for both quasi-static and fatigue testing. Since the main focus of this research was the investigation of fatigue behavior, the fatigue specimen geometry was chosen. The quasi-static testing was done simply to gather some baseline measurements using the fatigue ASTM E466 geometry. A colleague in our research group performed quasi-static testing on ASTM E8/E345 standard samples machined from the same electrical steel sheet to obtain the quasi-static properties [44]. It is these properties that are used to normalize data shown in this thesis.

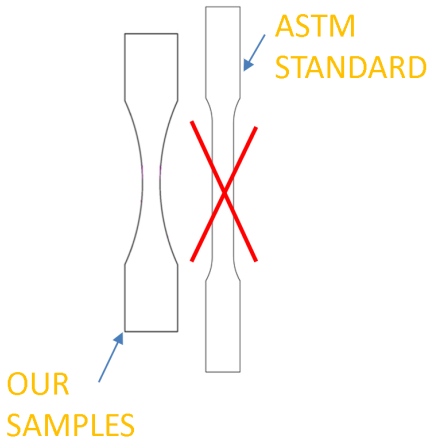

Figure 48: Illustration of the sample's geometries

Before the testing began however, each sample was painted and speckled for both room temperature and high temperature testing. This is shown below in section 4.2.1, figure 59. The grip section of the samples were masked and the gauge section of the samples were painted with white paint and speckled with black paint. This was to ensure the DIC could measure the strain of the sample.

One important point to note regarding the high temperature tested laminated samples is that they were prepared differently. Using the normal geometry was not viable for the laminated samples at high temperature. The grips for the MTS 810 are manual grips and work fine for single sheet samples (at any temperature) and the laminated samples at room temperature. However, at high temperatures the laminated samples de-laminated. In order to proceed with the testing, holes were drilled in the center of the samples and custom grips were machined in order to conduct the tests. The setup used for this testing is shown below. This method of preparation was used for the high temperature quasi-static and fatigue testing of the laminated samples. While the hole does create a point of stress concentration, the overall area of highest stress concentration is still the middle of the gauge section as this is the location with the smallest cross sectional area.

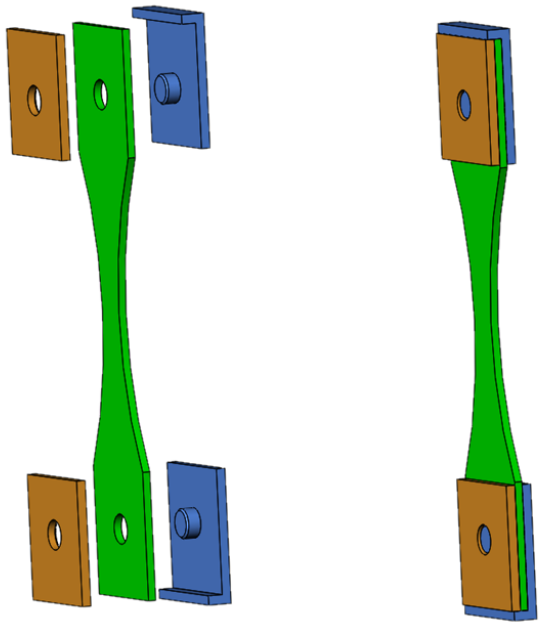

Figure 49: High temperature quasi-static test setup for laminated samples

Figure 50: (a) Single sheet sample (b) laminated sample

3.4 Quasi-Static Test Setup

The parameters for the quasi-static testing are as follows. The room temperature quasi-static testing was conducted on the Instron 8874 biaxial testing machine while the high temperature testing was conducted on the MTS 810 uniaxial testing machine. Both of these machines are shown in figure 46. The DIC used for measuring the strain of each sample is the Aramis/GOM DIC system.

3.5 Fatigue Test Setup

The room temperature fatigue testing was conducted on the Instron 8874 biaxial testing machine while the high temperature testing was conducted on the MTS 810 uniaxial testing machine. The same Aramis/GOM DIC was also used here. However, in this case, it was not used for strain measurement, it was used for crack detection. The aim here was to know which side of the sample the had crack initiated from. This way, when the samples were examined under the SEM, the fracture surface could be better understood.

Chapter 4: Quasi-Static Behavior of Electrical Steel at Room and High Temperature

Quasi-static tests were conducted on the single sheet electrical steel samples to determine their quasi-static properties such as yield strength, elongation and elastic modulus. These tests were performed at room temperature and 150°C, and after the tests a fracture analysis was conducted to analyze the differences in the fracture mechanisms of these samples. A comparison was conducted to see the effects temperature on the quasi-static properties of electrical steel and these findings are discussed in this chapter.

4.1 Material and Methods

The setup used for the SEM and EBSD is detailed in section 3.1. Phase identifications and texture of the steel sheet was carried out using a Bruker D8-Discover X-ray diffraction (XRD) equipped with a VÅNTEC-500 area detector and Cr-K radiation (=2.28970 Å) at an operating condition of 30 kV and 45 mA. The testing method used for the quasi-static testing of the electrical steel at room and high temperature is outlined in section 3.2.1. The details for the sample preparation are outlined in section 3.3. The test setup used for the quasi-static testing at both room temperature and high temperature is outlined in section 3.4.

4.2 Results

4.2.1 Microstructural Analysis

Before the testing began, a microstructural analysis was done on the electrical steel. This was done to gather some fundemental knowledge of the material. The electrical steel used in this analysis was a 3% silicon alloy steel, non-oriented, fully processed and are all oriented in the rolling direction.

Figure 51 below shows a micro-graph of the cross section of electrical steel taken in the rolling direction. Material characterization and in particular, micro-graphs were made with the help of Dr Dulal Saha of the FATSLAB research group [54]. Here the grain sizes are quite large where, in some cases, only 2-3 grains extend the entire cross section. Using the mean linear intercept method

[55], the grain size was measured to be 72 µm. This image is very similar to the findings of Bode et al. [38] as the grains are large in size and in some cases can span the entire thickness of the part.

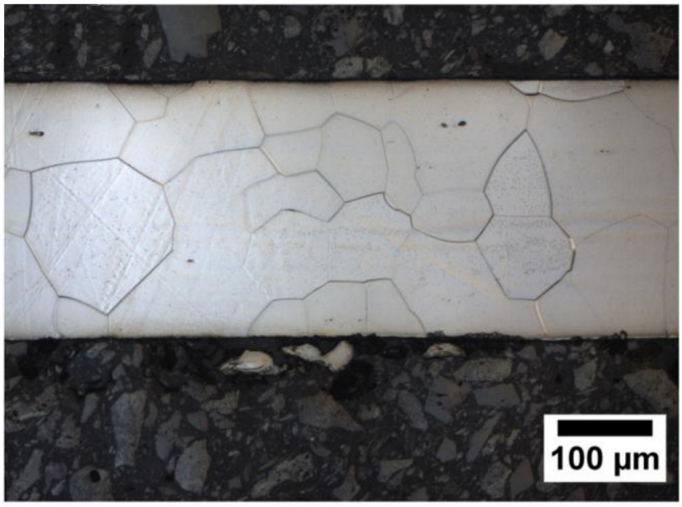

Figure 51: Micro-graph of electrical steel in the rolling direction

To further understand the microstructure of the electrical steel a phase identification study was conducted [54]. It was found that the electrical steel is almost 100% body-centered cubic (BCC). The result of this phase identification is shown below in figure 52. According to the phase diagram given in figure 53 a 3% silicon alloy steel is expected to be 100% BCC and this phase identification confirms this.

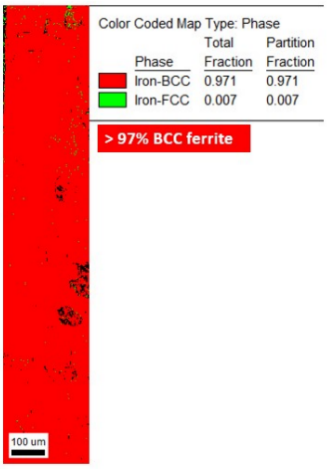

Figure 52: Phase identification of the electrical steel in the rolling direction

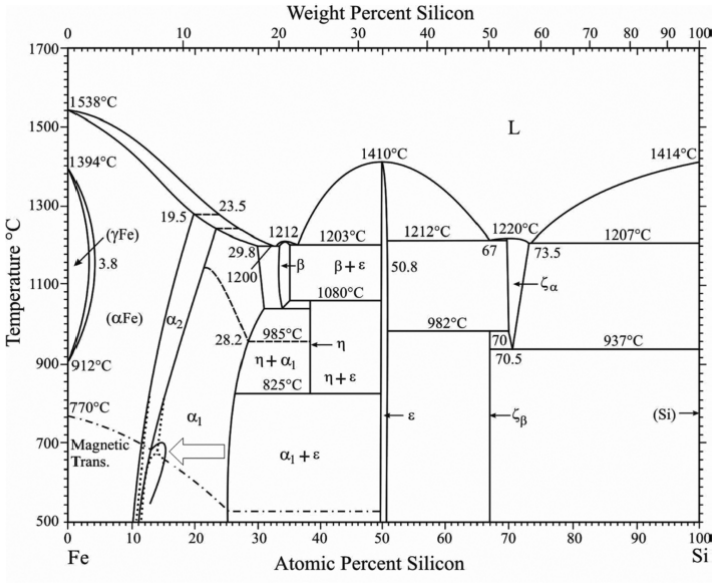

Figure 53: Fe-Si phase diagram [56]

The orientation of the grains analyzed using the EBSD and the results are displayed in figure 54a and the measured misalignment angles are graphed in figure 54b. These results show that the grains on average have a misalignment of approximately 2.5°. This is what is to be expected as this material is supposed to be a non-oriented electrical steel, and these findings help to confirm this.

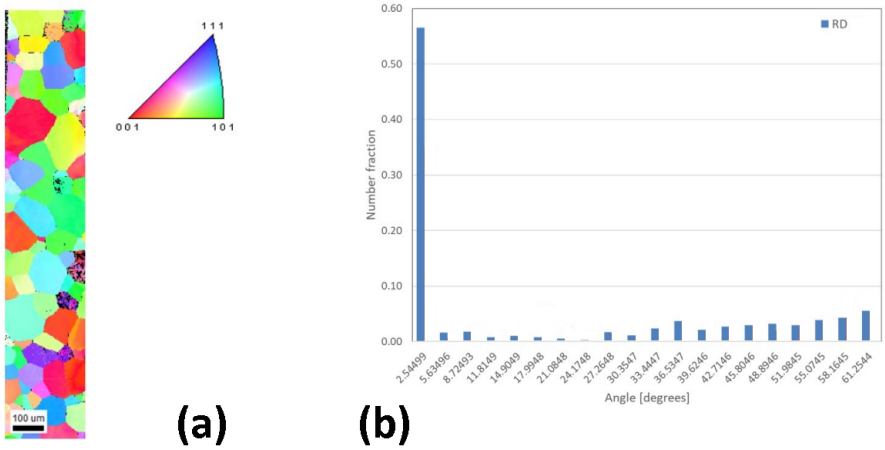

Figure 54: (a) Grain orientation of electrical steel in the rolling direction, (b) graph showing the angular misalignment of the grains

The EBSD analysis also measured the crystallographic texture of the electrical steel which is shown in figure 55.

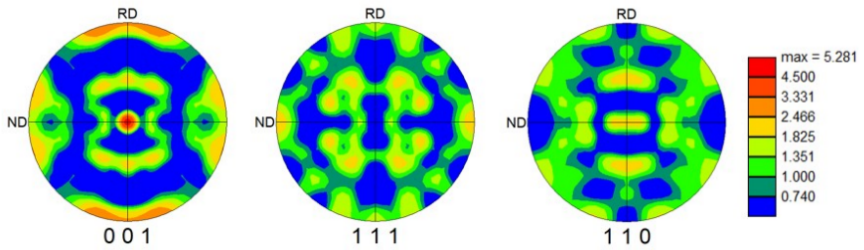

Figure 55: Crystallographic texture of the electrical steel

To confirm that this was indeed a 3% silicon alloy steel, an EDS compositional analysis was conducted to further understand the material. From this EDS compositional analysis, the elemental composition of this material was measured and is tabulated below in table 1. The silicon content was measured to be 2.9% which confirms that the silicon content is correct.

Table 1: Material composition of electrical steel used in testing

C	Al	Si	Fe
6.7%	0.7%	2.9%	89.7%

In literature, it is known that for electrical steel, some impurities are used to control grain growth such as manganese sulfide and aluminum nitride [6, 7, 57]. This EDS compositional analysis confirms the presence of aluminum nitride in the microstructure. It was found at both the grain boundaries and within grains of the microstructure. A picture of these precipitates is shown in figure 56.

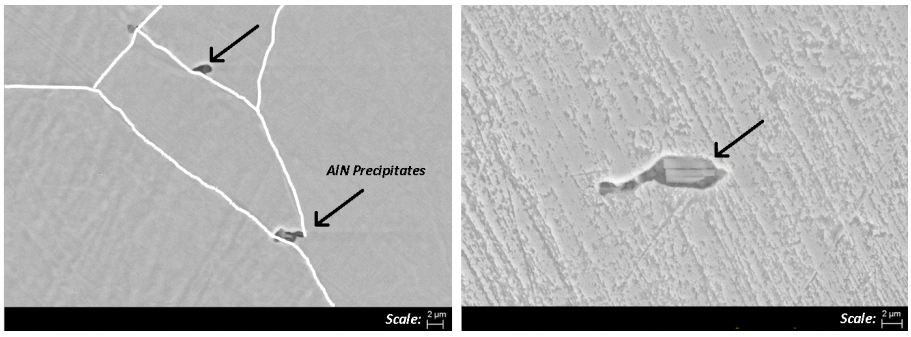

Figure 56: Aluminum nitride precipitates shown (a) along the grain boundaries and (b) within the grains

Finally this EDS compositional analysis helped to identify the top layer of the sample. The top layer of the sample was comprised of an insulation layer that is meant to electrically isolate each layer of electrical steel and improve the chemical and thermal resistivity of the electrical steel. The analysis confirms that there is a thin layer of oxidation from the manufacturing process that is present in the form of silicon oxide and there is also a high amount of phosphorus in the insulation layer. This layer on the top of the samples is about 0.5 to 1 µm thick and is shown in figure 57.

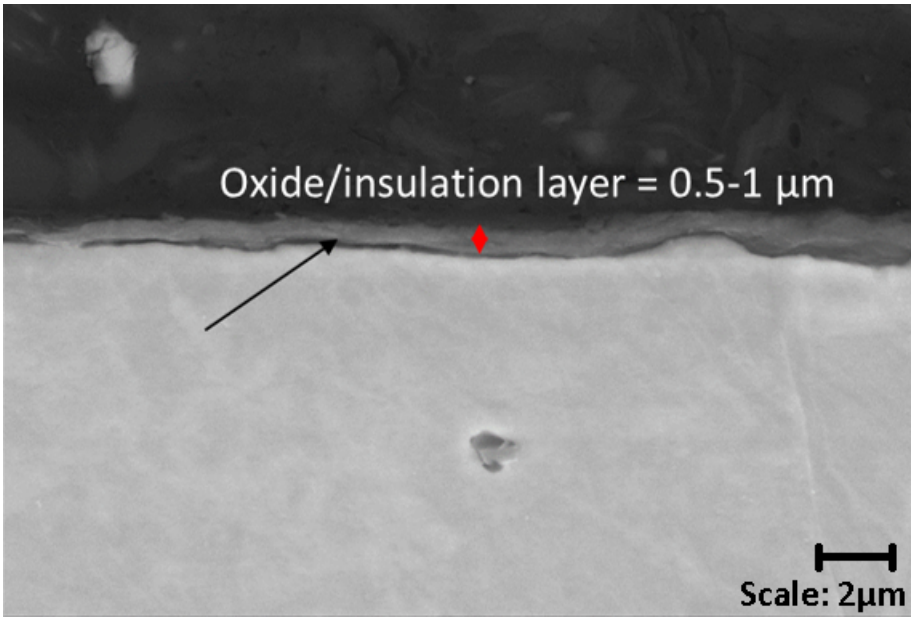

Figure 57: Top layer of the sample showing a mixture of the silicon oxide layer and insulation layer, totalling to 0.5-1 µm in thickness

4.2.2 Quasi-Static Testing Room Temperature

The results for the quasi-static testing at room temperature for the samples are shown in figure 58 and table 2. Three quasi-static tests were conducted and their results were averaged to estimate the quasi-static properties of the material. The results have been normalized by the yield strength of the electrical steel obtained at room temperature by Tolofari et al. [44] using ASTM E8/E345 samples [36, 37].

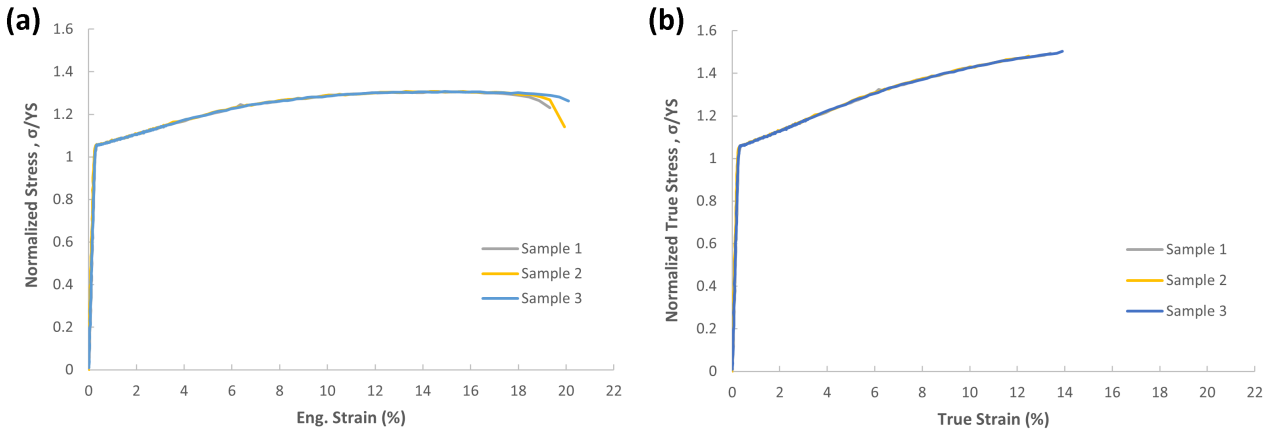

Figure 58: Room temperature quasi-static test results for single sheet samples (a) engineering, and (b) true stress-strain curves

Table 2: Normalized quasi-static test results at room temperature for the single sheet samples

Mechanical Properties	Sample 1	Sample 2	Sample 3	Average	Standard Dev.
Elastic Modulus [MPa/MPa]:	396	412	388	398	11
Yield Strength (0.2% offset) [MPa/MPa]:	1.06	1.06	1.07	1.06	0.01
True Ultimate Strength [MPa/MPa]:	1.49	1.48	1.50	1.49	0.01
Engineering Ultimate Strength [MPa/MPa]:	1.31	1.31	1.31	1.31	0.00
Engineering Fracture Strain [%]:	19	20	23	21	2
Reduction in area (RA) [%]:	/	19	/	19	/
Strength coefficient, H [MPa/MPa] (*):	1.99	1.96	1.99	1.98	0.01
Strain hardening exponent, n (*):	0.14	0.14	0.14	0.14	0.00
Poisson's Ratio	0.28	0.26	0.27	0.27	0.01

The samples before and after the room temperature quasi-static test are shown below.

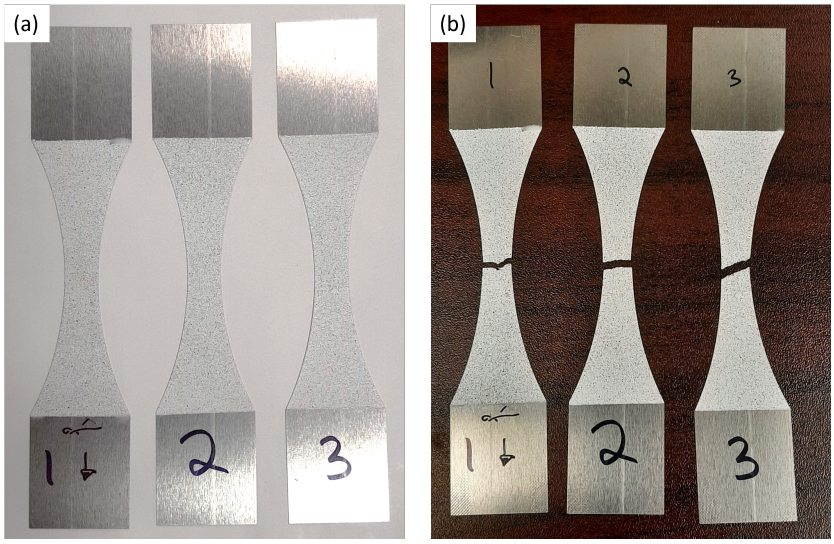

Figure 59: Room temperature quasi-static tested single sheet samples, painted and speckled for strain measurement using DIC (a) before and (b) after testing

4.2.3 Quasi-Static Testing High Temperature

The results for the quasi-static testing at 150°C for the samples are shown in figure 60, and the detailed properties are given in table 3. Three quasi-static tests were conducted and their results were averaged to estimate the quasi-static properties of the material. The results have been normalized by the yield strength of the electrical steel obtained at room temperature by Tolofari et al. [44] using ASTM E8/E345 samples [36, 37].

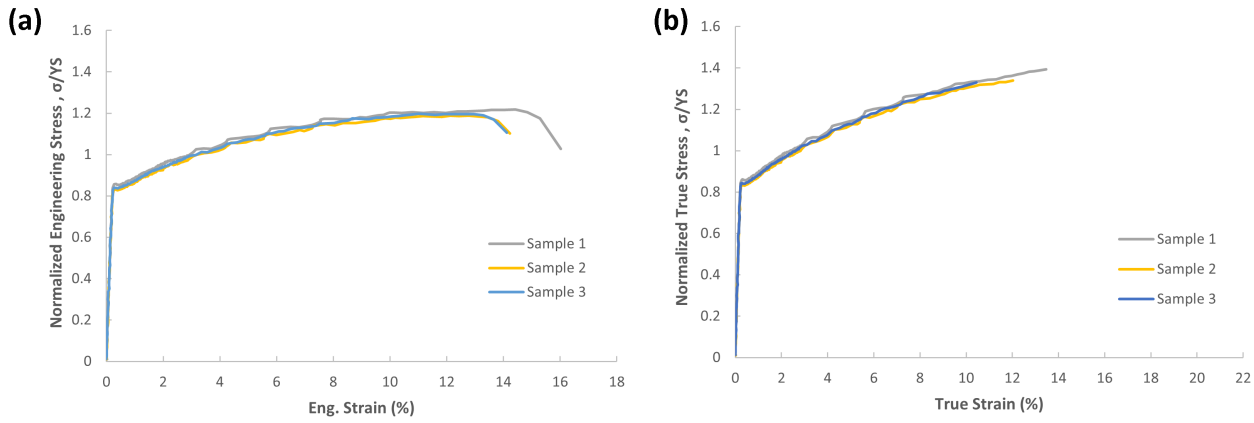

Figure 60: High temperature quasi-static test results for single sheet samples (a) engineering and (b) true stress-strain curves

Table 3: Normalized quasi-static test results at elevated temperature for the single sheet samples

Mechanical Properties	Sample 1	Sample 2	Sample 3	Average	Standard Dev.
Elastic Modulus [MPa/MPa]:	387	369	377	378	9
Yield Strength (0.2% offset) [MPa/MPa]:	0.85	0.82	0.85	0.84	0.02
True Ultimate Strength [MPa/MPa]:	1.39	1.34	1.33	1.35	0.03
Engineering Ultimate Strength [MPa/MPa]:	1.22	1.19	1.20	1.20	0.01
Engineering Fracture Strain [%]:	16	14	14	15	1
Reduction in area (RA) [%]:	/	100	/	100	/
Strength coefficient, H [MPa/MPa] (*):	2.00	1.99	2.01	2.00	0.01
Strain hardening exponent, n (*):	0.18	0.18	0.20	0.19	0.01
Poisson's Ratio	0.27	0.27	0.27	0.27	0.00

The samples before and after the elevated temperature quasi-static test are shown below.

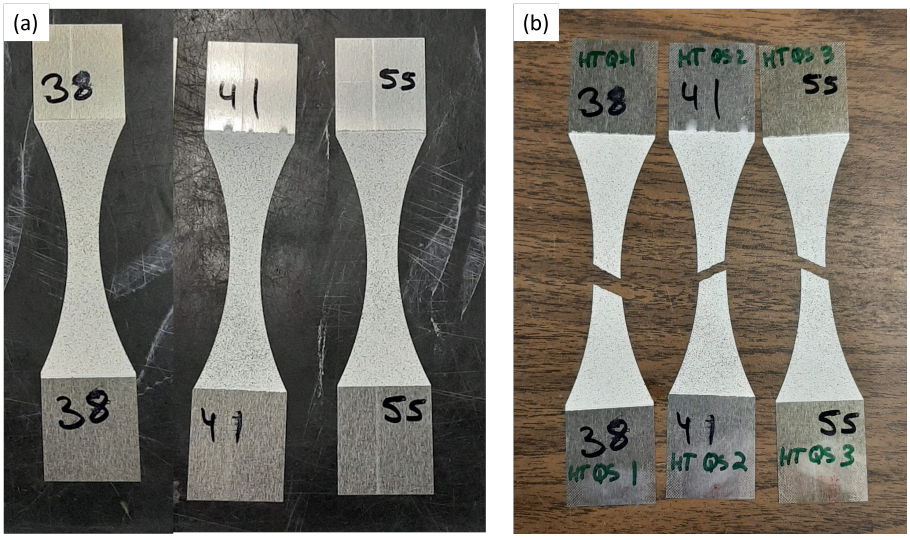

Figure 61: High temperature quasi-static tested single sheet samples, painted and speckled for strain measurement using DIC (a) before and (b) after testing

4.3 Analysis

The results of the testing done at both temperatures are compared below in figure 62 and in table 4.

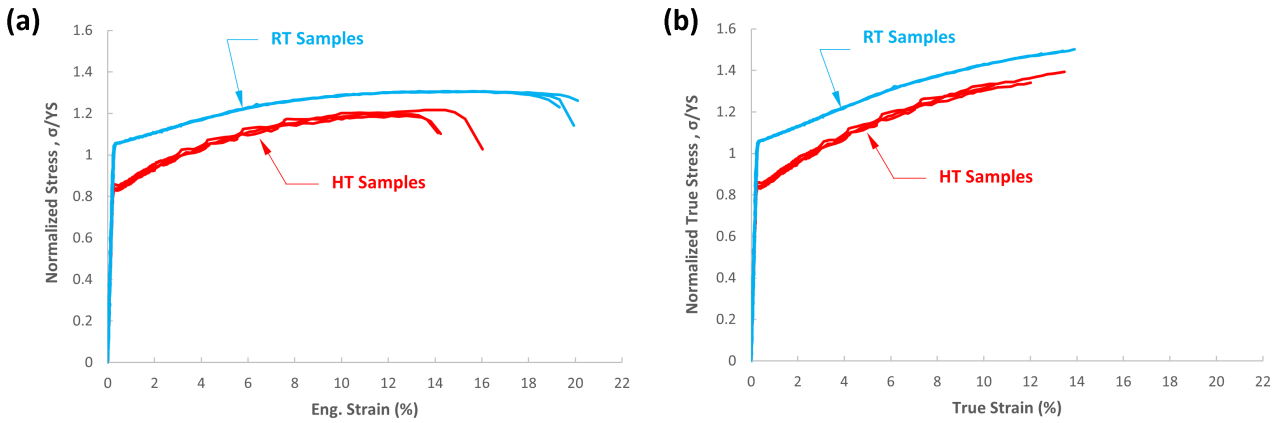

Figure 62: Quasi-static stress-strain curves of single sheet samples (a) engineering stress (b) true stress

Table 4: Normalized quasi-static test results for the electrical steel single sheet samples

Mechanical Properties	Room Temperature	High Temperature	% difference
Elastic Modulus [MPa/MPa]:	399 ± 11	378 ± 9	-5.3
Yield Strength (0.2% offset) [MPa/MPa]:	1.06 ± 0.01	0.84 ± 0.02	-21
True Ultimate Strength [MPa/MPa]:	1.49 ± 0.01	1.35 ± 0.03	-9.4
Engineering Ultimate Strength [MPa/MPa]:	1.31 ± 0.00	1.20 ± 0.01	-8.4
Engineering Fracture Strain [%]:	21 ± 2	15 ± 1	-29
Reduction in area (RA) [%]:	19%	100%	426%
Strength coefficient, H [MPa/MPa] (*):	1.98 ± 0.01	2.00 ± 0.01	1.0
Strain hardening exponent, n (*):	0.14 ± 0.00	0.19 ± 0.01	36
Poisson's Ratio	0.27 ± 0.01	0.27 ± 0.00	0.0

These results show a visible decrease in the strength of the electrical steel at the elevated temperature. There is a drop in the elastic modulus, yield strength, ultimate tensile strengths, and the fracture strain. There is also a very significant increase in the area reduction % at 150°. This shows that while the elongation shows that the ductility decreased at the higher temperature, the overall ductility did in-fact increase drastically when factoring in the increase of the reduction in area %. This is unexpected as the current literature does not discuss this phenomenon. The deformation was very localized (which is reflected in area reduction) and more strain was accommodated in smaller region. The method used to calculate the reduction in area is detailed in section 3.1.

4.3.1 Fracture Analysis

The fractured surface of a quasi-static sample from the room temperature testing is shown below in figure 63. It appears that the failure initiated on the left side of the sample in the yellow highlighted region (figure 63e) indicated by the white arrow. There are a mix of inter-granular and trans-granular cleavage facets in this region, indicated with green arrows shown in figure 63e. Further to the right of the sample, the crack propagation zone is shown (figure 63f). This is the location where the sample overloaded and this is where the sample transitioned to local necking as seen in figure 63g. This region of local necking extends from figure 63g to figure 63b. In the red highlighted region, the sample had a sudden overload failure. It is here where some local necking (figure 63b and 63c) on the fracture surface appears, indicated by the red arrows. At figure 63c there is another transition where the sample is no longer necking. Here there is also some mixed cleavage facets, and this is at the other end of the sample (figure 63d). It is important to note that the 'local necking' is thinning that is occurring along the thickness of the sample, and is not to be confused with the typical necking that is seen in steel, that occurs along the width of the sample.

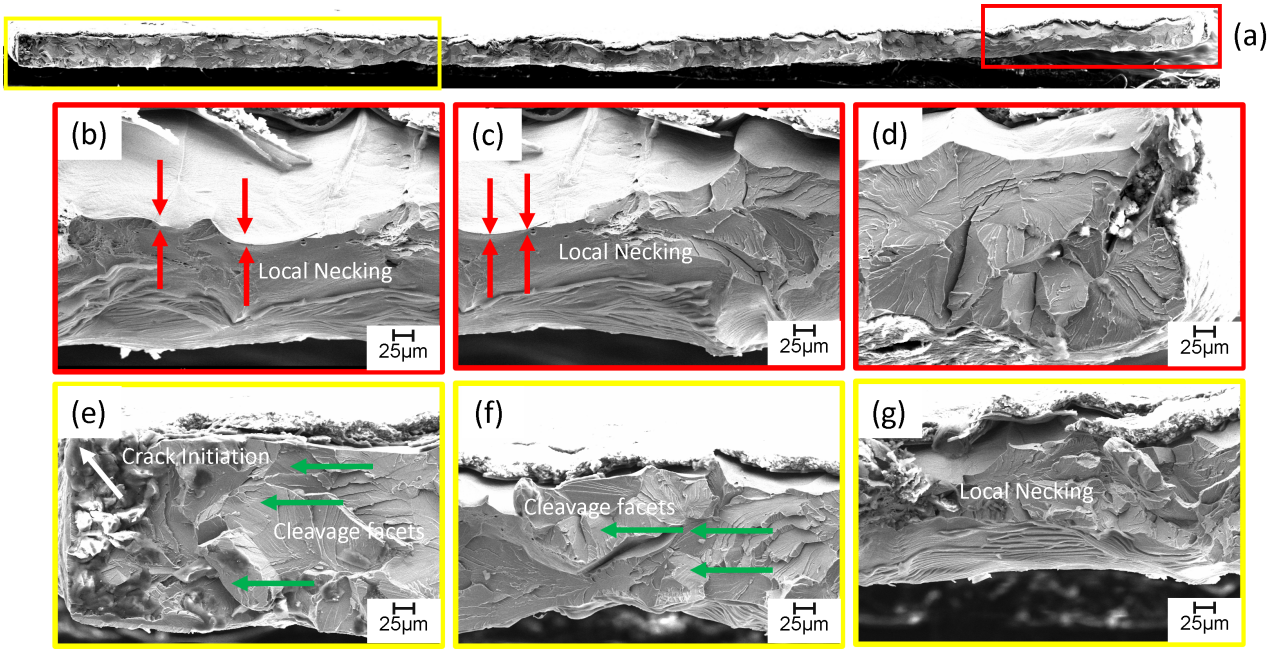

Figure 63: Fracture surface of room temperature quasi-static tested single sheet (a) overall view of fracture surface (b) local necking (c) local necking-transition zone (d) edge of sample (e) crack initiation zone with inter-granular cleavage facets (f) crack propagation zone with inter-granular cleavage facets (g) transition zone to local necking

A fractured quasi-static sample from the high temperature testing is shown below in figure 64. The crack initiated on the left side, shown in figure 64b. Here the crack propagation zone is much smaller in comparison to the room temperature sample. The crack did not advance too far before the sample overloaded, as right after this region, there is some severe necking visible in figure 64a. A close-up of the right side of the sample is shown in the bottom right of the figure 64c. Here some local necking is shown on the fracture surface. On the right side of the sample there is also some deformation twinning. This twinning is a significant finding as it shows that the grains are stretched under the axial loading and, to accommodate for the severe thinning, the crystal lattice deforms to prevent the fracture of the sample.

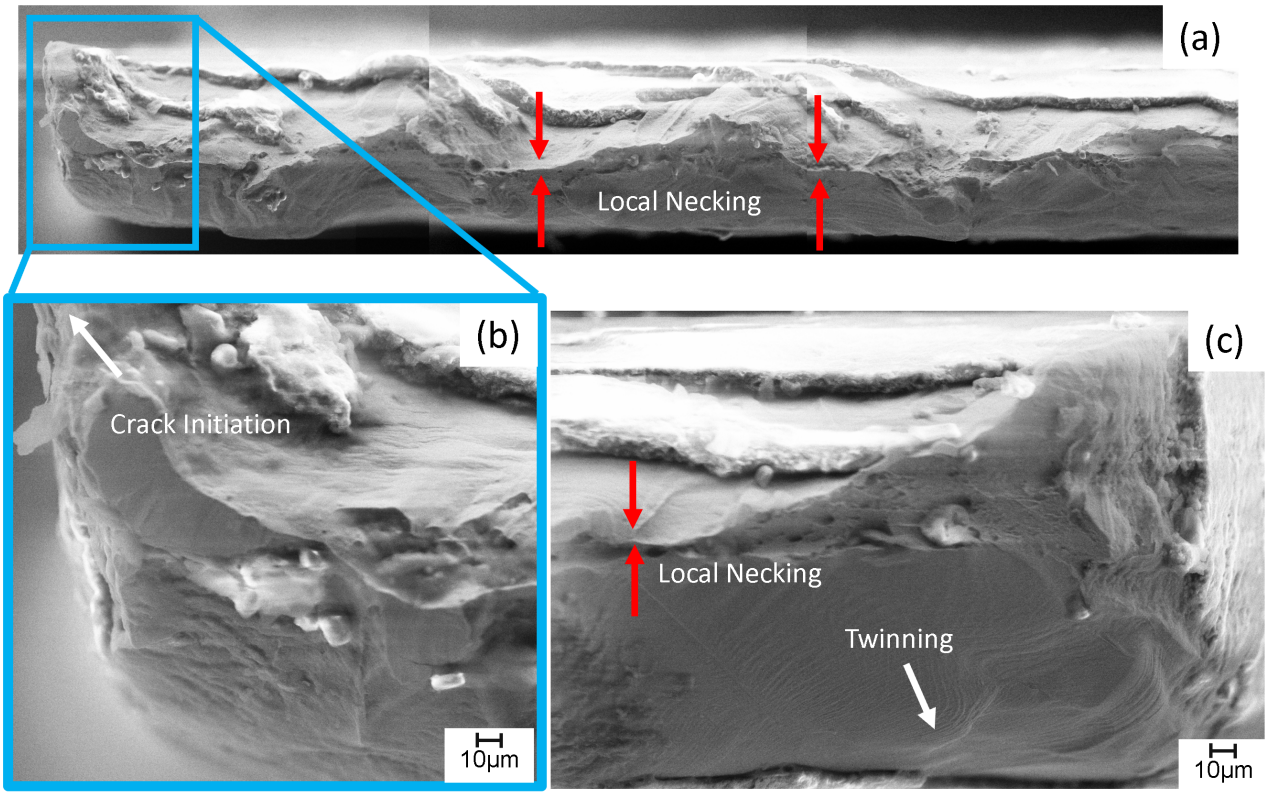

Figure 64: Fracture surface of high temperature quasi-static tested single sheet (a) fatigue damage zone showing some severe thinning (b) crack initiation zone (c) other side of fracture surface showing some deformation twinning and severe thinning

The thinning that occurred at both room temperature and high temperature is illustrated in figure 65, where figure 65a shows the thinning of the sample at room temperature, and figure 65b shows the thinning of the sample at high temperature. A close-up top view of the sample is also shown

to better visualize the deformation that is occurring and to better understand the fracture surface of the samples. In figure 65a the flat region represents the cleavage facets and the thinner area represents the local necking that is occurring. Similarly figure 65b shows the entire top view of the sample with a thin section to represent the severe thinning. It is important to emphasize that this is not the same necking that occurs along the width of the sample, which is typical for steel.

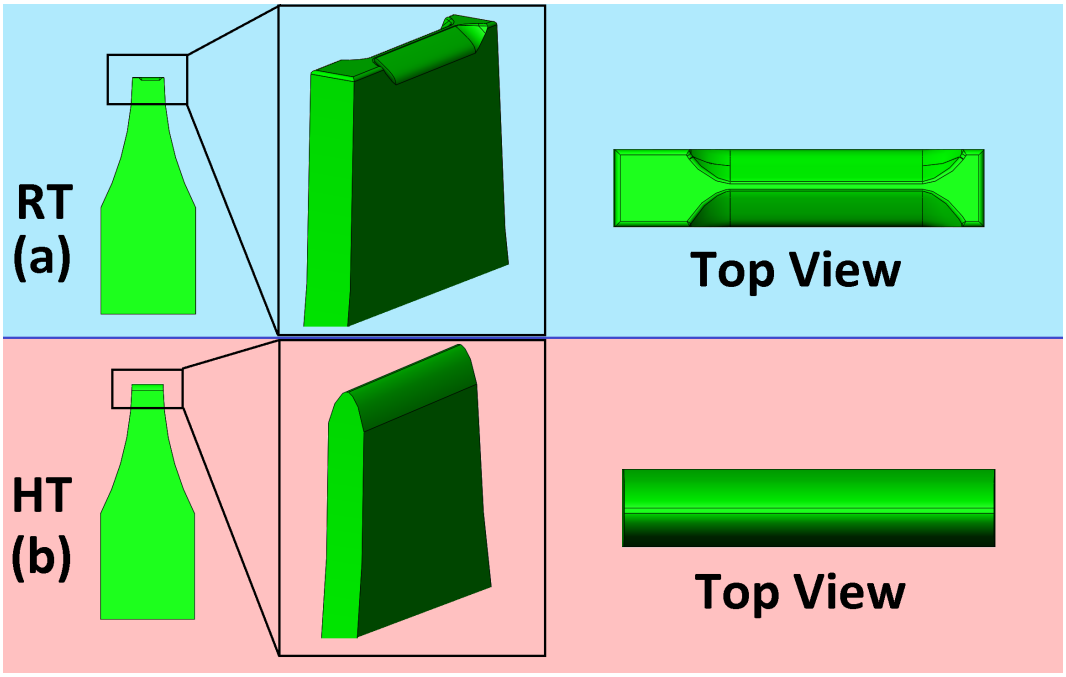

Figure 65: Fracture surface CAD drawing of a quasi-static tested sample at (a) room temperature (b) high temperature

4.3.2 Further Failure Analysis

Below is the side view of the fracture zone of the room and high temperature samples. Figure 66 shows some trans-granular cleavage facets along the polished edge of the samples indicated by the green arrows. For the high temperature sample in figure 67 more local necking (ductile fracture) is shown compared to the room temperature samples which show more of a sudden brittle fracture. This helps to better understand the grain deformation that is occurring at the center of the samples, where they fracture. Figure 67 shows an interesting behavior for the electrical steel. It shows that there is some great elongation that is occurring at the microscopic level however, only the few grains closest to the fracture surface are elongating, the remaining grains do not seem to be elongating as greatly as seen in figure 64c. This can help to explain the phenomenon seen in figure

62. For a normal steel, greater ductility and greater elongation is expected at the high temperature. However, the results showed a lower overall fracture strain at the higher temperature. Here, the fracture surface shows that there is a greater elongation occurring however, it is concentrated in only a few grains. This proves that the ductility is very high at 150°C and while the fracture strain decreased by 29%, the reduction in area increased by 426%, proving that the ductility overall increases as the temperature of the sample increases. Figure 64c also shows some grain separation occurring as indicated by the purple arrows. This grain separation is important to the research as it confirms that the main failure is trans-granular. Both figures 63b and 64c show slips bands shown by the blue arrows indicating that slip bands appear at both room temperature and high temperature.

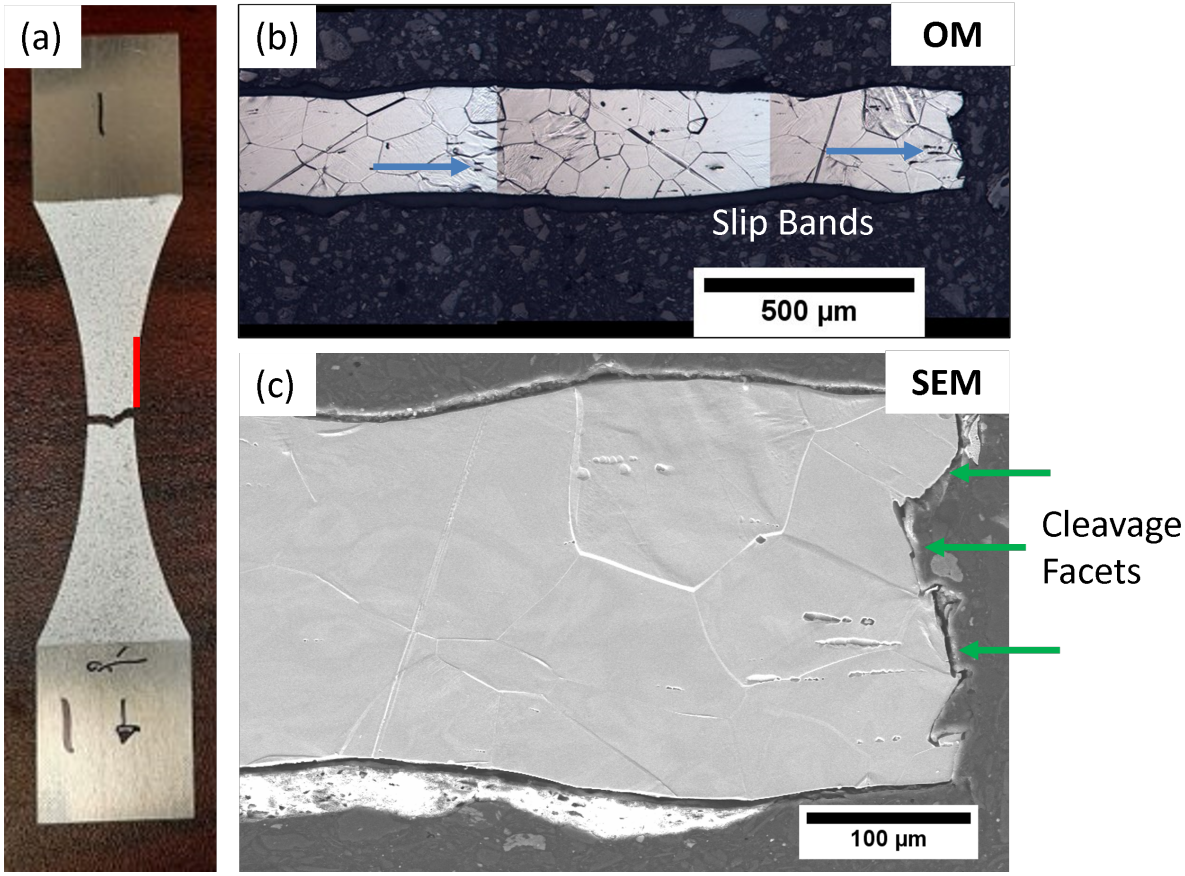

Figure 66: Side view of the fracture zone of room temperature quasi-static tested single sheet (a) overall sample (b) highlighted (red line in (a)) edge under OM (c) highlighted edge under SEM, showing trans-granular failure

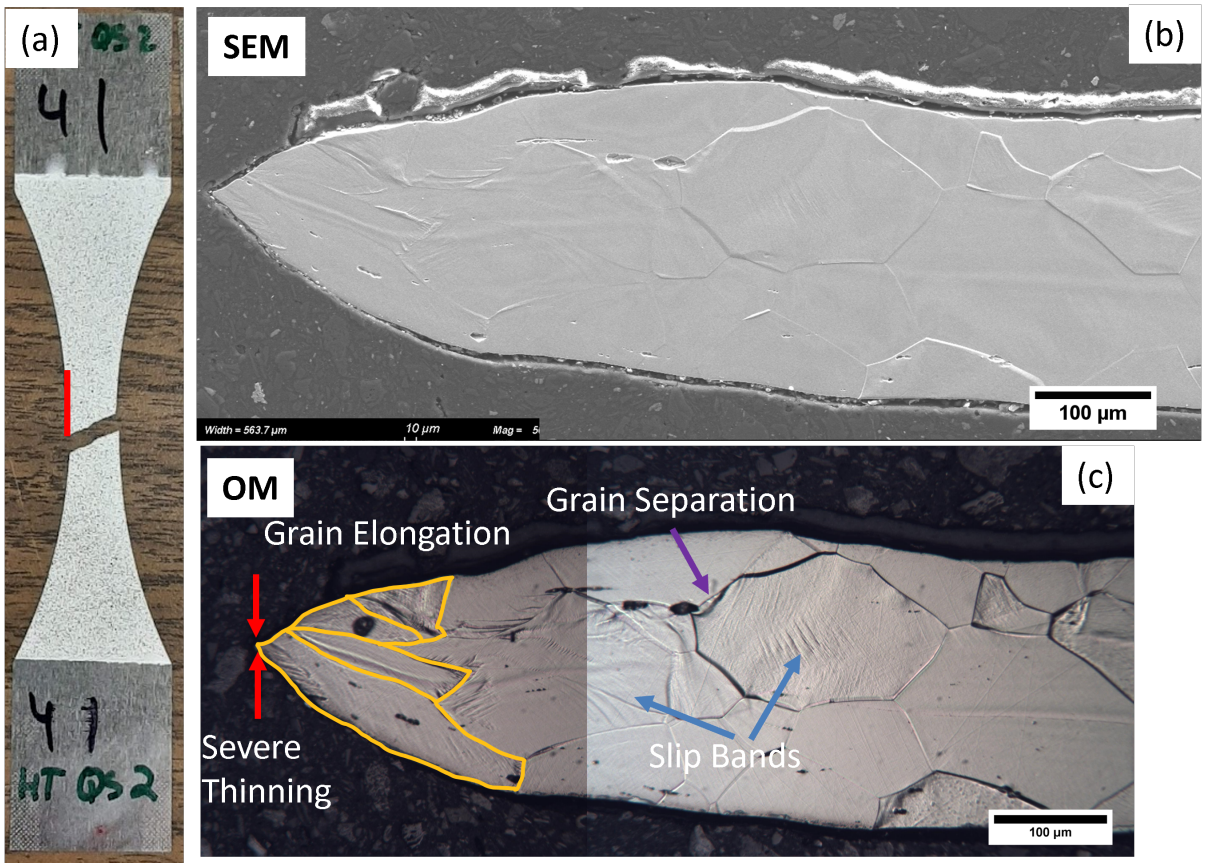

Figure 67: Side view of the fracture zone of high temperature quasi-static tested single sheet (a) overall sample (b) highlighted (red line in (a)) edge under SEM (c) highlighted edge under OM, with grains showing considerable elongation (highlighted in blue)

4.4 Discussion

The high temperature results for the quasi-static testing are very different than the room temperature results. At the elevated temperature, a decrease in the overall strength of the electrical steel is observed. Figure 62 and table 4 show that the elastic modulus, yield strength, ultimate tensile strength and fracture strain all decrease drastically, while the reduction in area increased. Fortese et al. [41] observed a similar decrease in the elastic modulus by 4.4% and yield strength by 15.3% which corroborates the results of the tensile testing that was conducted here. Fortese et al. measured the ultimate tensile strength of 1.2 normalized stress, and similarly, Bode et al. [38] measured a normalized stress that is very close to the room temperature results of approximately 1.28 normalized stress and a fracture strain of 16% at room temperature of a Fe-3.3%Si. Schayes et al. [40] measured a fracture strain of 28% and an ultimate tensile strength of 1.36 normalized

stress for a Fe-3Si, which indicates that there is variation for similar alloys of electrical steel that share similar Si content.

Additionally the global necking that was seen in figure 63 is also what was presented in literature by Bode et al. [38], where they found that under quasi-static loading, the specimens undergo a ductile failure, show trans-granular cleavage facets and show that the failure mechanism transitions to global necking. The new findings shown in figure 64 extend the findings of Bode et al. [38]. At 150° the entire sample undergoes global necking, rather than a localized region. This change in failure mechanism is related to the change in ductility seen at 150°. At 150° the fracture strain decreases and the reduction in area increases drastically. The ductility of electrical steel does increase as the temperature increases however, rather than the entire sample elongating, the sample locally elongates, and thins as shown in figure 67.

The reason for this ductility behavior of electrical steel at 150°, can be attributed to additional slip systems activating at this temperature. To understand this mechanism, the two figures 66 and 67 are key. Here, both figures show slip bands that are present near the location of fracture. However, figure 67 and the high temperature samples are showing more grain elongation than the room temperature samples. Here the slip bands also change their orientation as the grain elongates (figure 67) due to the higher temperature, resulting in a lower tolerable stress. The room temperature samples do have some grain elongation occurring however, it is in a localized region, rather than the entire cross section. This means that when slip systems are available, the sample experiences global necking, and when these slip systems are not present, the sample failure mode is trans-granular. This theory is corroborated by the findings of Henning et al. [42]. At room temperature the failure location occurs at triple points, in trans-granular nature, near the grains that have the highest hardening rate. The failure does not necessarily occur at the location where local hardening is highest at the beginning of the test. This study does not analyze the strain behavior at higher temperatures however, since there is no trans-granular cleavage facets at this temperature, the mechanism does appear to be changing. Since the grains are softening at the higher temperature, they will not fail at triple points, rather the failure is ductile and the grains elongate instead, and more slip systems activate as result, overall decreasing the mechanical properties of the material.

4.5 Chapter Conclusion

This chapter investigated the microstructural properties of the electrical steel.The electrical steel single sheet samples were then tensile-tested at room temperature and at an elevated temperature of 150°. After analyzing the results the following conclusions can be made based off the findings of the research.

- The microstructure of this material contains very large grains that are of similar magnitude to the thickness of the samples. The grain size was measured to be 72 µm.
- The crystal structure of the sheets is 97.1% BCC (body centered cubic).
- The grains are randomly oriented and not oriented in any particular direction. This confirms that the material is non-oriented.
- The material's silicon content was measured to be 2.9% and aluminium nitride precipitates were detected in the microstructure. Additionally the insulation layer was found to contain a high phosphorus content, and some oxidation was also detected in this layer.
- The quasi-static results show a decrease in the elastic modulus, yield strength, ultimate tensile strength, and fracture strain as well as an increase in area reduction at 150°C compared to the room temperature.
- The fracture surface shows that the main failure mechanism at room temperature is trans-granular cleavage facets, which transitions to global necking, while at 150°C the results show that the main mechanism is global necking. At 150°C there is an increase in ductility however, it is locally concentrated near the fracture surface through grain elongation.
- At 150°C there is a greater number of available slip systems, and due to the higher temperature and softening of the grains, the grains elongate, and the slip systems orient to fracture the sample at a lower fracture strain, and lower overall stress.

For automotive manufactures, this information is very important to know as under high speeds and extreme loading, the motor can heat up considerably. It is important as such to adjust design criteria to avoid premature failure of the electric motor stator or rotor core.

Chapter 5: Fatigue Behavior of Electrical Steel (Room and High Temperature)

Cyclic tests were conducted on the single sheet electrical steel samples to determine their fatigue properties. The goal was to determine the correlation between life of the samples at different stress amplitudes. The goal was to create the Basquin model for the electrical steel at room temperature and 150°C and to see the effect of the temperature on the fatigue of electrical steel. After the tests a fracture analysis was conducted to analyze the differences in the fracture mechanisms of these samples and these findings are discussed in this chapter. A condensed analysis on this chapter was approved for publication by SAE International for WCX 2023 [58].

5.1 Material and Methods

The testing method used for the fatigue testing of electrical steel at room and high temperature is outlined in section 3.2.2. The details for the sample preparation are outlined in section 3.3. The test setup used for both the fatigue testing at both room temperature and high temperature is outlined in section 3.5.

5.2 Results

5.2.1 Fatigue Testing Room Temperature

A total of 28 fatigue tests were conducted at room temperature. The normalized stress amplitude was varied between 0.57 to 0.37 with 3-5 samples tested at each load level. The results from the fatigue testing done at room temperature are shown below in table 5. The plot for this fatigue data is shown below in figure 68. The results have been normalized by the yield strength of the electrical steel obtained at room temperature by Tolofari et al. [44] using ASTM E8/E345 samples [36, 37].

Table 5: Normalized room temperature fatigue results for single sheet samples

Test #	Sample #	R-ratio	Stress Amplitude (MPa/MPa)	Loading Freq (Hz)	Total life, Nf (cycles)	Failure Location
1	28	0.1	0.57	0.5	682	within gauge section
2	27	0.1	0.55	0.5	7546	within gauge section
3	29	0.1	0.55	0.5	3962	within gauge section
4	58	0.1	0.55	0.5	3336	within gauge section
5	26	0.1	0.54	0.5	13608	within gauge section
6	25	0.1	0.53	0.5	11526	within gauge section
7	6	0.1	0.51	2	33331	within gauge section
8	5	0.1	0.51	2	27728	within gauge section
9	14	0.1	0.51	2	22174	within gauge section
10	4	0.1	0.48	2	72857	within gauge section
11	10	0.1	0.48	3	69149	within gauge section
12	13	0.1	0.48	3	77059	within gauge section
13	22	0.1	0.48	3	79914	within gauge section
14	30	0.1	0.48	3	71302	within gauge section
15	12	0.1	0.44	4	126986	within gauge section
16	19	0.1	0.44	5	119428	within gauge section
17	20	0.1	0.44	5	115033	within gauge section
18	23	0.1	0.44	5	254535	within gauge section
19	16	0.1	0.44	5	178740	within gauge section
20	9	0.1	0.40	10	344764	within gauge section
21	11	0.1	0.40	10	313461	within gauge section
22	17	0.1	0.40	10	557532	within gauge section
23	18	0.1	0.40	10	343511	within gauge section
24	21	0.1	0.40	10	293697	within gauge section
25	43	0.1	0.40	10	309432	within gauge section
26	8	0.1	0.37	10	2384143	Run-out
27	15	0.1	0.37	10	2001279	Run-out
28	7	0.1	0.37	10	2460170	Run-out

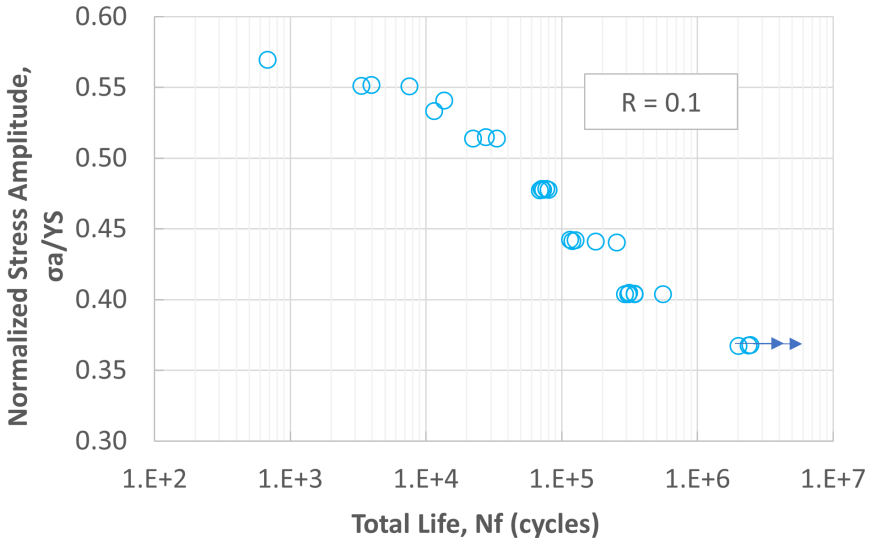

Figure 68: Fatigue results for room temperature tested single sheet samples

Here the samples are able to achieve runout at 0.37 normalized stress and are able to tolerate a

max stress level of 0.57 normalized stress. Here there is also very good repeatability of life at each load level tested at room temperature. The samples from the room temperature tests are shown below in figure 69. All samples that did not reach run-out, completely separated upon failure, with the exception of samples 22 which reached the displacement limit of 5mm.

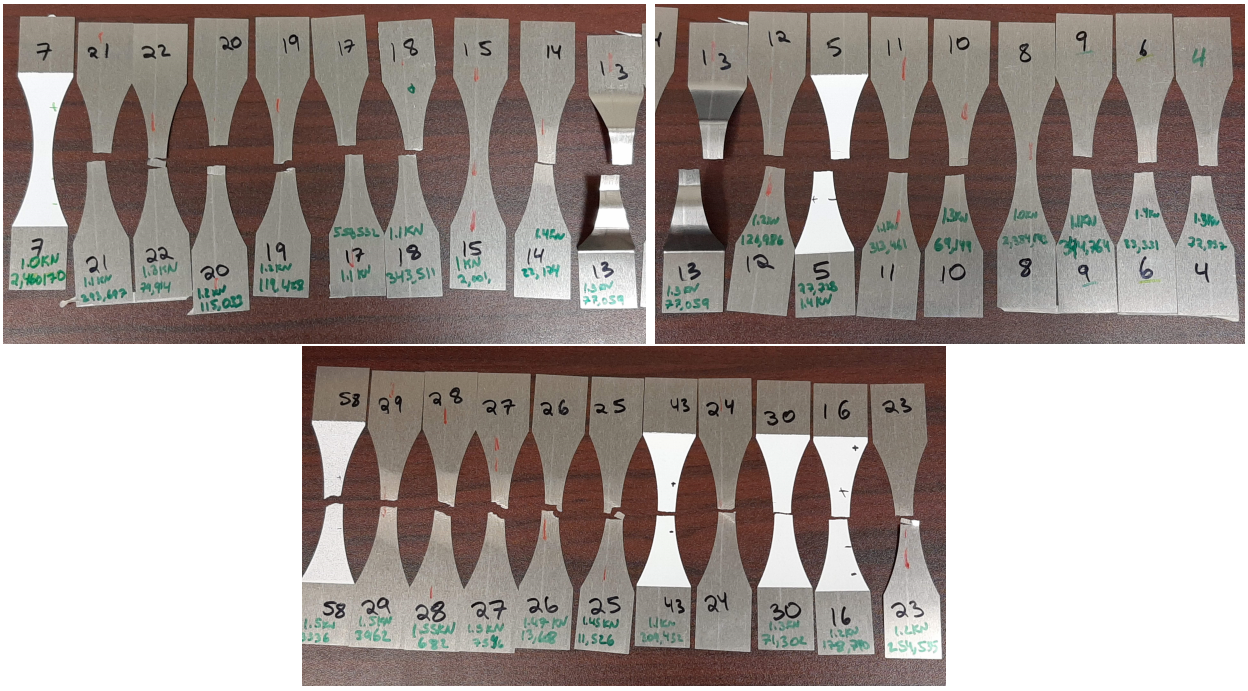

Figure 69: Fatigue samples for room temperature tested single sheet samples

5.2.2 Fatigue Testing High Temperature

The results from the fatigue testing done at high temperature are shown below in table 6 and the plot for the fatigue data is shown below in figure 70. Here a total of 17 tests were conducted and the stress amplitude was varied between 0.55 and 0.37. 2-3 tests were conducted at each load level and the samples reached run-out at a normalized stress of 0.37. The results have been normalized by the yield strength of the electrical steel obtained at room temperature by Tolofari et al. [44] using ASTM E8/E345 samples [36, 37].

Table 6: Normalized high temperature fatigue results for single sheet samples

Test #	Sample #	R-ratio	Stress Amplitude (MPa/MPa)	Loading Freq (Hz)	Total life, Nf (cycles)	Failure Location
1	42	0.1	0.55	0.5	3	within gauge section
2	44	0.1	0.53	0.5	8211	within gauge section
3	45	0.1	0.53	0.5	6903	within gauge section
4	46	0.1	0.51	2	25583	within gauge section
5	47	0.1	0.51	2	13270	within gauge section
6	56	0.1	0.51	2	27174	within gauge section
7	31	0.1	0.48	3	53503	within gauge section
8	40	0.1	0.48	3	43930	within gauge section
9	54	0.1	0.48	3	54134	within gauge section
10	33	0.1	0.44	5	94957	within gauge section
11	36	0.1	0.44	5	81466	within gauge section
12	39	0.1	0.44	5	65437	within gauge section
13	48	0.1	0.40	10	201798	within gauge section
14	49	0.1	0.40	10	167325	within gauge section
15	50	0.1	0.40	10	119418	within gauge section
16	57	0.1	0.37	10	2000000	Runout
17	59	0.1	0.37	10	2000000	Runout

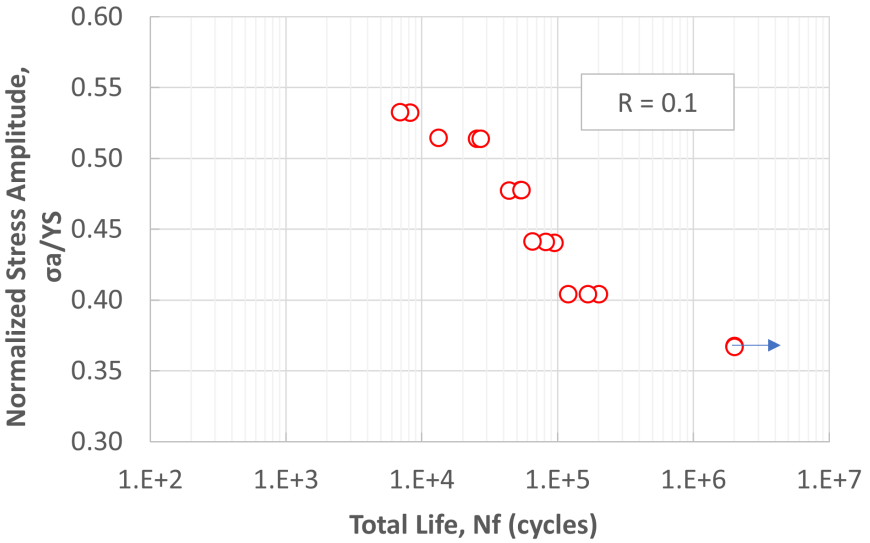

Figure 70: Fatigue results for high temperature tested single sheet samples

The samples used in the testing are shown below in figure 71. All samples that did not reach run-out, completely separated upon failure.

Figure 71: Fatigue samples for high temperature tested single sheet samples

5.3 Analysis

A comparison of the S-N curves for both the room temperature testing and high temperature testing is shown below in figure 72.

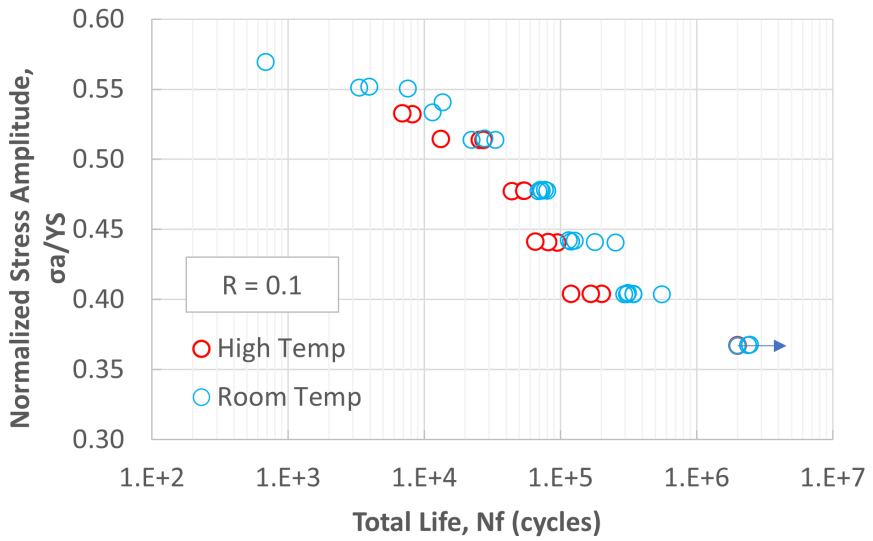

Figure 72: Fatigue results for room and high temperature tested single sheet samples

The Basquin model and Owen's Design curve was drawn for both the room temperature and high temperature results for the cyclic testing. Below is the line of best fit drawn for the room temperature results shown in figure 73.

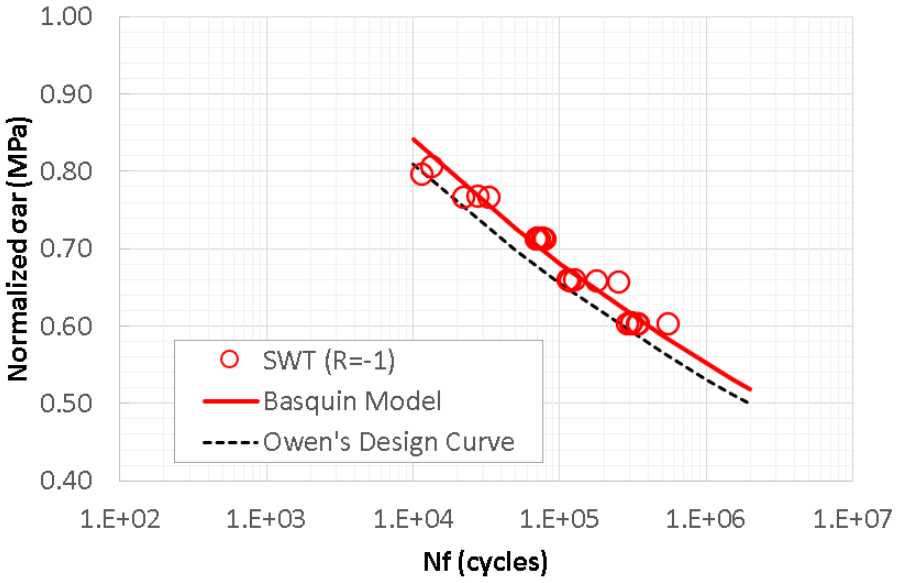

Figure 73: Fatigue properties for room temperature tested single sheet samples

The resulting equation for the Basquin Model is shown below.

$$\sigma_{ar} = 2.08(2N_f)^{-0.091} \tag{7}$$

The resulting equation for the Owen's Design Curve is shown below using 90% reliability and 90% confidence.

$$\sigma_{ar,90/90} = 2.00(2N_f)^{-0.091} \tag{8}$$

The resulting line of best fit that can be drawn for the high temperature results for the cyclic testing is shown in figure 74.

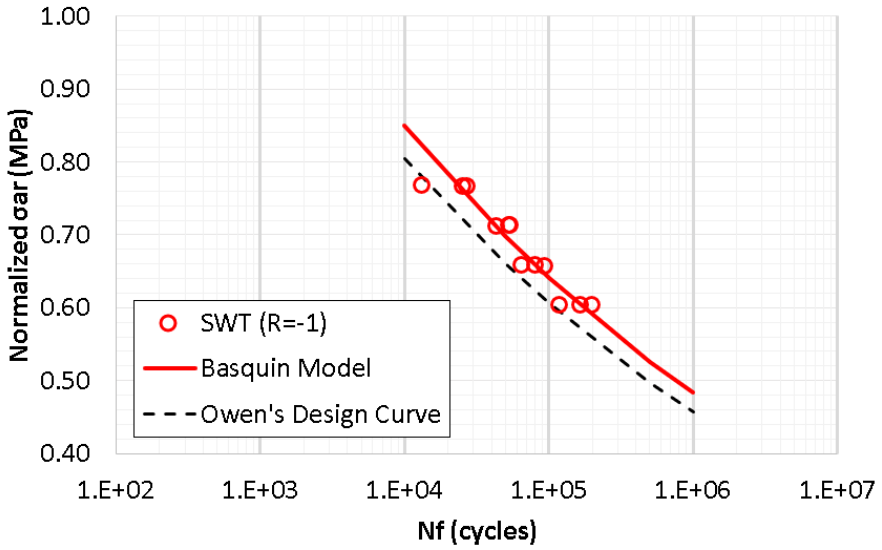

Figure 74: Fatigue properties for high temperature tested single sheet samples

The resulting equation for the Basquin Model is shown below.

$$\sigma_{ar} = 2.87(2N_f)^{-0.123} \tag{9}$$

The resulting equation for the Owen's Design Curve is shown below.

$$\sigma_{ar,90/90} = 2.72(2N_f)^{-0.123} \tag{10}$$

Stamped samples at room temperature appear to have a better fatigue curve and Owens design curve in comparison to the high temperature samples. As the number of cycles increases, the two curves diverge indicating that room temperature samples have a greater life as the stress amplitude decreases. This is a normal trend that is expected at higher temperatures.

5.3.1 Fracture Analysis

To understand the failure mechanisms occurring during cyclic testing, two samples at room temperature and two samples from the high temperature cyclic testing will be compared. At each temperature, one sample from the LCF and one sample from the HCF-regime will be compared to see the differences in the failure mechanism.

The fracture analysis will first focus on the room temperature cyclic testing. Below in figure 75 is the fracture surface of sample 5. The life of this sample was 27,728 cycles, and this sample had a very short life. Using the DIC, it is known that the crack initiated from the left side of the fracture surface. This area is highlighted in figure 75a and 75b. The sample has some striations in the fatigue damage zone, indicated by the blue arrows shown in figure 75b, and outside the fatigue damage zone, there is some trans-granular cleavage facets indicated by the green arrows shown in figure 75c. Trans-granular cleavage facets are a common failure mechanism for silicon steels [47]. The fatigue damage zone was measured to be 0.66mm.

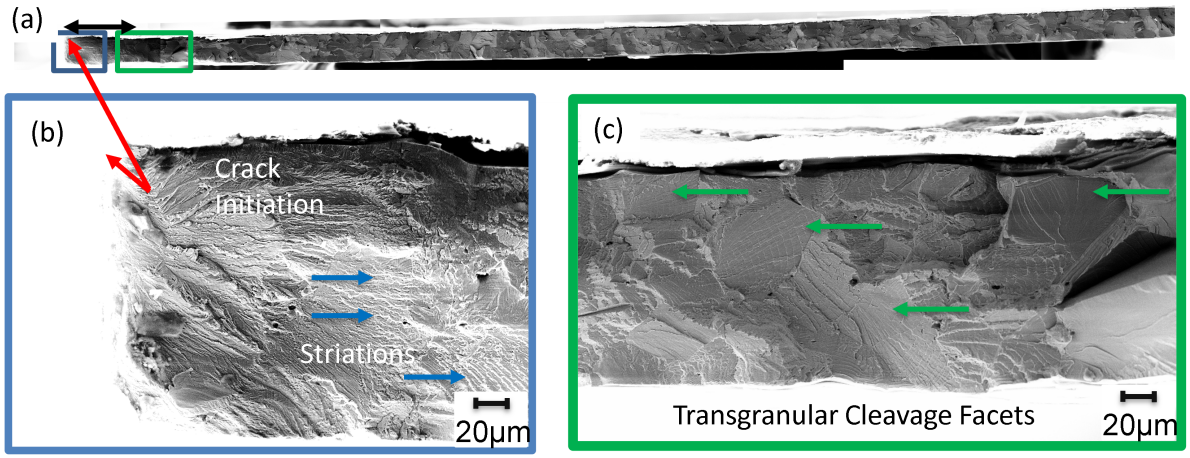

Figure 75: Fracture surface of single sheet sample at room temperature, low cycle fatigue, Nf = 27,728 cycles, (a) overall fracture surface (b) crack initiation zone with visible striations (c) trans-granular cleavage facets

Below in figure 76 is the fracture surface of sample 17. The life of this sample was 557,532 cycles, and this has much higher life. The crack initiated from the right side of the sample and its location has been highlighted in figure 76a, 76b and 76c. In the fatigue damage zone, there is some inter-

granular cleavage facets, which are outlined in red and shown in figure 76c. Outside of this zone, there is some trans-granular cleavage facets indicated by green arrows and shown in figure 76d. In comparison to sample 5 above, the fatigue damage zone is a larger here at 1.2mm.

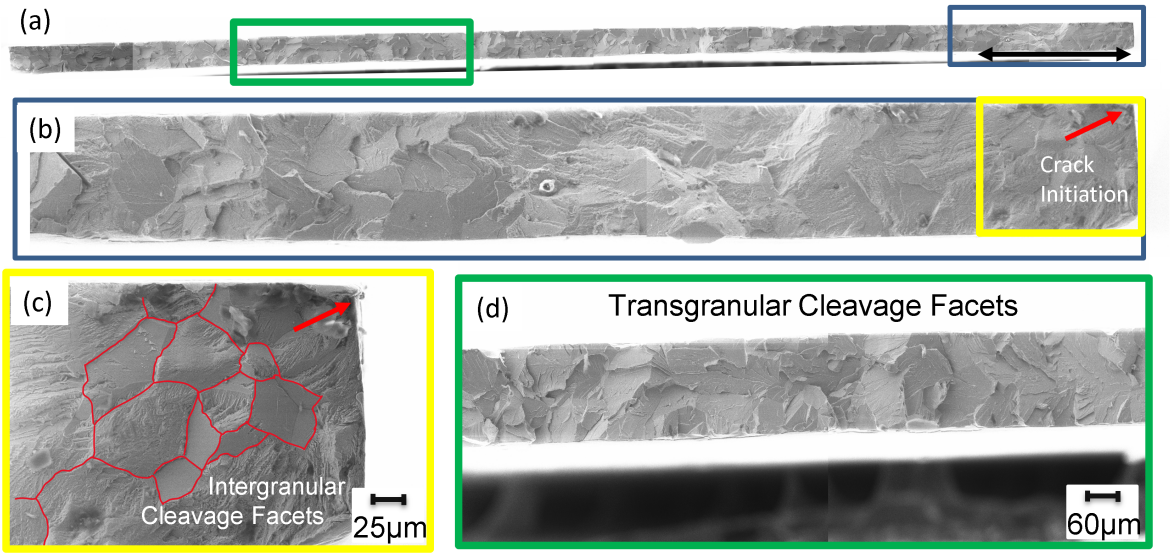

Figure 76: Fracture surface of single sheet sample at room temperature, high cycle fatigue, Nf = 557,532 cycles, (a) overall fracture surface (b) fatigue damage zone (c) crack initiation zone (c) trans-granular cleavage facets

The fracture analysis will now focus on the fracture surfaces of the high temperature cyclic tested samples. Below in figure 77 is the fracture surface of sample 46. The life of this sample was 25,583 cycles, and this sample was a part of the low cycle regime on the stress life curve. This sample was tested at the same load level as samples 5 shown in figure 75. The crack initiated from the right side of the sample and its location has been highlighted in figure 77a, 77b and 77d. In the fatigue damage zone there is some river like striations that are located near the point of crack initiation indicated by the blue arrows shown in figure 77d. Here the fatigue damage zone was shown to be about 0.33mm. Outside of the fatigue damage zone the failure mechanism changes to severe necking that extends across for the rest of the sample shown in figure 77c, indicated by the red arrows.

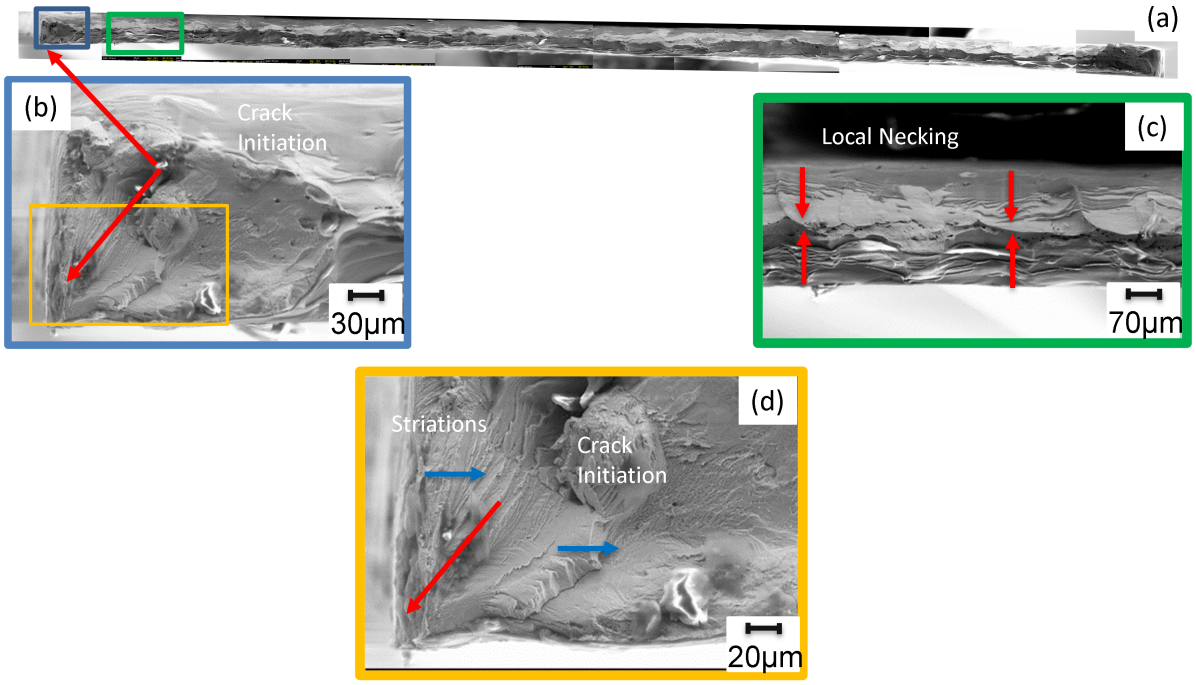

Figure 77: Fracture surface of single sheet sample at high temperature, low cycle fatigue, Nf = 25,583 cycles, (a) overall fracture surface (b) fatigue damage zone (c) trans-granular cleavage facets (d) crack initiation zone with visible striations

Below in figure 78 is the fracture surface of sample 48. The life of this sample was 201,798 cycles. This sample was a part of the high cycle regime of the stress life curve and tested at the same load level as samples 17 shown in figure 76. The crack initiated from the left side of the sample and its location has been highlighted in figure 78c. In the fatigue damage zone there is some river like striations (indicated by blue arrows) that are located near the point of crack initiation (indicated by the red arrow) shown in figure 78c. Here the fatigue damage zone was shown to be about 1.73mm and is shown in figure 78d. Outside of the fatigue damage zone the failure mechanism changes to severe necking that extends across for the rest of the sample shown in figure 78b.

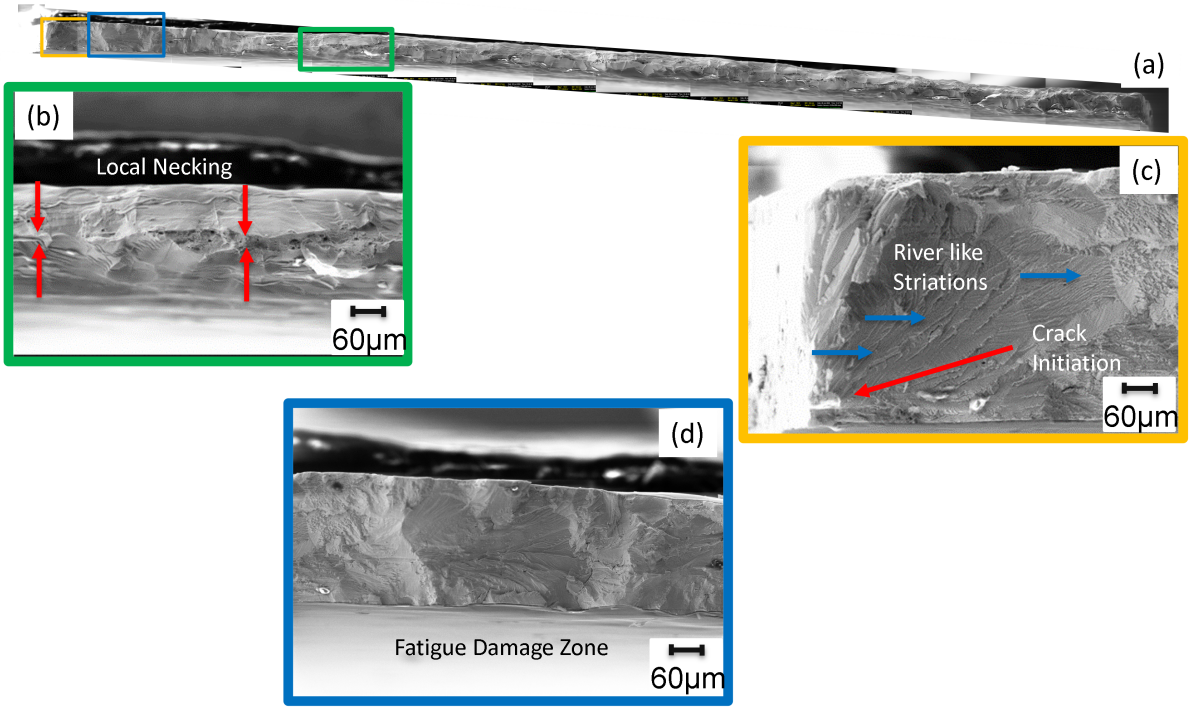

Figure 78: Fracture surface of single sheet sample at high temperature, high cycle fatigue, Nf = 201,798 cycles, (a) overall fracture surface (b) severe necking (thinning) (c) crack initiation zone (d) fatigue damage zone

5.4 Discussion

The results of the testing show that as the temperature increases, the fatigue life decreases. This is shown when comparing the Basquin model for both the room temperature and high temperature results, as the high temperature curve diverges away from the room temperature curve, indicating a decrease in the overall strength of the material. This is a result of the bias that originates in the room temperature results from a few points at the higher stress amplitudes tested. Looking at figure 34, the ideal fatigue data shows some overlap in the low life regime and branches out as the number of cycles increases. Since the electrical steel at room temperature can tolerate a higher stress amplitude, and since these points near the low-cycle region were included in the Basquin model, this can explain the difference in the slope of the room and high temperature Basquin models. The fatigue data is also similar to what is found in literature. Bode et al. [38], where the punched samples achieved the same run-out (2 million cycles) at 0.3 normalized stress and peaked at 0.42 normalized stress at room temperature. The single sheet samples achieved run-out at 0.37

normalized stress and could tolerate 0.53 normalized stress so the alloy in this research is exhibiting stronger but comparable behavior. A similar study done by Dehmani et al. [47] where the same R ratio was used. In this study, the maximum stress amplitude was 0.69 at room temperature and 0.56 normalized stress at 180°C. In this same study, the minimum stress amplitude was 0.38 at room temperature and 0.32 normalized stress at 180°C. While the high temperature testing was conducted at a different temperature than this study, the results do indicate that both alloys behave similarly.

The resulting normalized Owen's Design Curve can be used with similar electrical steels of similar composition as a starting point to help understand the expected change in behavior between room temperature and 150°C. Since the data is normalized it can be appropriately used in the design of a different material given its yield strength to help approximate the expected fatigue behavior.

A trend in the results is that as the temperature increases, the fatigue damage zone appears to decrease. This is due to the decrease in strength at elevated temperature, that was evident from the quasi-static testing shown in figure 62. Since the strength of the electrical steel decreases, a smaller crack, and therefore, a smaller reduction in area, is required to achieve the sudden tearing that occurs once the sample fractures. This fatigue damage zone is the area where the crack initiation and crack growth is visible, before the crack propagates to fracture the sample.

Another trend is the change in the fracture mechanism. At room temperature, the main failure mechanism is the trans-granular cleavage facets. This is a ductile-brittle fracture. Schayes et al. [40] also found that the main failure mechanism at room temperature was both trans-granular and inter-granular in nature, which transitioned to a sudden brittle fracture of the material. The failure mechanism at high temperature is severe thinning outside the fatigue damage zones, which are smaller in size compared to the room temperature samples. This change in the failure mechanism is present for electrical steel because the higher temperature can help to release residual stresses and reduce dislocation density induced during the sheet manufacturing and sample preparation. This can result in a shorter fatigue life. This decrease in overall life is confirmed by Dehmani et al. [47] as he tested electrical steel at 180°C and saw a similar decrease in the overall life of the samples. However, this change in the failure mechanism was not shown in these results. The failure mechanism changes here as at a higher temperature, there is more available slip systems, and due

to the higher temperature and softening of the grains, the grains can elongate, and the slip systems orient to fracture the sample sooner, and through the global necking that is shown in the fracture surface.

Bode et al. [38], compared the effect of punching on the fatigue of electrical steel and found that the life of the material is lower due to a higher surface roughness, residual stresses and work hardening that occurs at the cutting edge. Compressive residual stresses slow crack growth, and tensile residual stresses accelerate crack growth. Work hardening can yield the material and can also make the material brittle and accelerate crack propagation. The surface roughness can cause a stress concentration on the cutting edge. Below is the micro-hardness measurements taken near the edge of the electrical steel sample, shown in figure 79. As the measurement of micro-hardness approaches the punched edge, the micro-hardness values increase. This also increases even further (looking at line 4) the surface hardness near the burr of the sample is measured. It is important to note that residual stress was not measured for this material, only the micro-hardness. However, the trend in the micro-hardness agrees with what is known for punched samples [23, 24, 25]. This point is significant and leads into another trend.

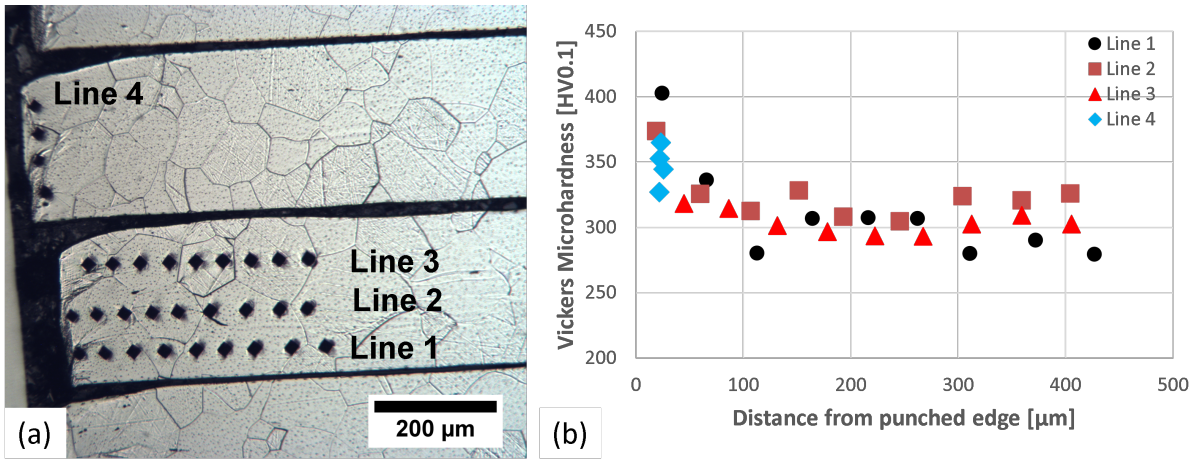

Figure 79: Laminated sample micro-hardness

A significant trend that was observed was that the crack always initiated from the burr region of the cutting edge regardless of load level or temperature. When the electrical steel is punched, the cutting edge is split into two distinct zones. When the die comes down to punch the sample, there is first some bending that occurs, this is the rollover region. The force of the die then causes

the electrical steel to shear, which gives a shear zone. However, the die does not shear the entire thickness of the electrical steel. Once the die has travelled about halfway down the thickness of the sample, a sudden fracture occurs where the sample separates from the sheet, and this is categorized as the tear/fracture zone. This is illustrated in figure 80 below. At the tip of this tear zone is a burr, and this is the area where the crack always initiates, as it is a point of stress concentration. Plastic deformation occurs in this area and causes the formation of micro-cracks that eventually propagate to fracture the sample [38]. This trend of increasing micro-hardness near the cutting edge of the electrical steel was also noted by Baudouin et al. [22] as he measured a peak of 280 HV near the cutting edge. He also found that the increase in silicon content increased the hardness of the overall material. Here the micro-hardness is much higher. However, if the cutting edge of the stamped samples are polished, this drastically increases the fatigue life, by eliminating the area of stress concentration and work hardening [47]. This finding is very similar to the findings of Schayes et al. [40] as the crack in their study always initiated from the tear zone.

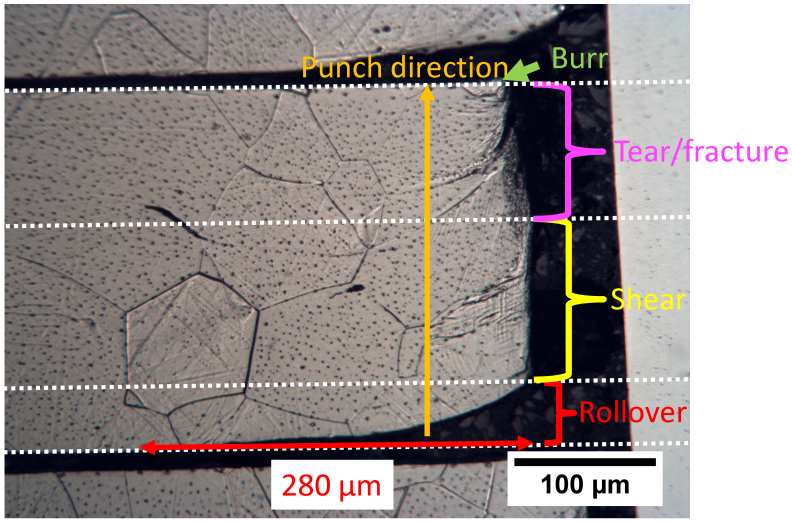

Figure 80: Cutting edge of punched electrical steel

Typically the stamped samples are known to have tensile residual stresses in the rollover and shear region and it transitions to a compressive residual stress in the tear/fracture region [21]. The stress distribution is not uniform in the thickness. It peaks in compressive stresses at the burr and reaches a maximum in tensile stresses in the rollover region [21]. It is important to note that the compressive residual stresses reside in the breakaway region of the cutting edge which is the tear/fracture region and extends to the burr of the sample. When the temperature increases, the

residual stresses will relax, and when the compressive residual stresses relax, there is a lower force closing the crack mouth, causing the overall life the of the sample to decrease here. This is another reason why the overall life decreases at 150°C. It is important to note that residual stresses were not measured in this study however.

5.5 Chapter Conclusion

The electrical steel single sheet samples were cyclic-tested at room temperature and at an elevated temperature of 150°. After analyzing the results the following conclusions can be made based off the findings of the research.

- As the temperature increases, the fatigue strength of the electrical steel decreases.
- The fracture surface shows that as the temperature increases, the fatigue damage zone decreases. The results also show a change in the failure mechanism changes where the room temperature samples show trans-granular cleavage facets as the main failure mechanism, and the high temperature samples show necking as the main failure mechanism.
- The reason that the life of the samples decreases at 150°C is because more available slip systems are present and grain softening is occurring. It is theorized that the residual stresses at this temperature decrease and the effect of the work hardening also decreases, which reduces the force closing the crack mount, resulting in a lower life.
- It was also noted that the crack always initiates at the burr for each sample, regardless of temperature.

Electric motors can achieve high temperatures. Over the life of the electric motor, the motor will be loaded and unloaded a countless number of times, and it is important to know this behavior of the electrical steel as it can help to prevent premature failure in the electric motor.

Chapter 6: Laminated Electrical Steel Quasi-Static and Fatigue Testing Behavior

Both quasi-static and cyclic tests were conducted on the single sheet electrical steel samples to understand the mechanical behavior and failure mechanisms of the electrical steel at room temperature and 150°C in chapters 5 and 6. The same quasi-static and cyclic tests were conducted on the laminated samples under the same conditions. The stress-strain curves, S-N curves, and fracture mechanisms have been analyzed and will be discussed in this chapter. The goal of this chapter is to determine the effect of laminating on the quasi-static and fatigue properties of electrical steel and compare the results to what was found in the single sheet electrical steel in chapters 5 and 6.

6.1 Methods and Materials

The testing method for the quasi-static testing at room temperature and high temperature follows the method described above in section 3.2.1. The testing method for the fatigue testing at room temperature and high temperature follows the method described above in section 3.2.2. The sample preparation for the quasi-static testing and the fatigue testing at both room and high temperature follows the method described above in section 3.3. The test setup for the quasi-static testing at both room temperature and high temperature follows the method described above in section 3.4. The test setup for the fatigue testing at room temperature and high temperature follows the method as described above in section 3.5.

6.2 Results

6.2.1 Quasi-Static Testing Room Temperature

The results for the quasi-static testing at an room temperature for the laminated samples are shown below. Three quasi-static tests were conducted and their results were averaged to estimate the quasi-static properties of the material. The results have been normalized by the yield strength of the electrical steel obtained at room temperature by Tolofari et al. [44] using ASTM E8/E345 samples [36, 37].

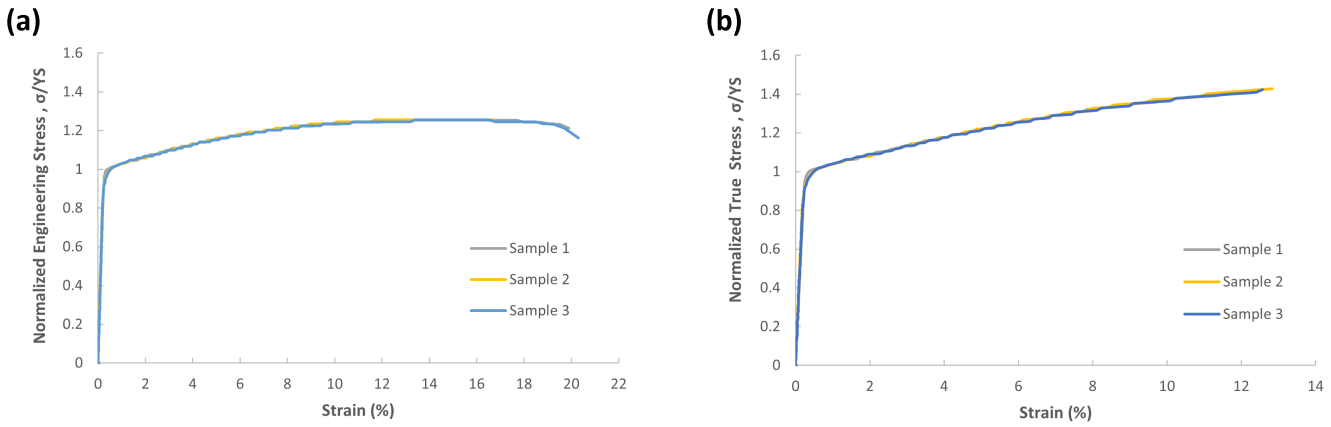

Figure 81: Room temperature quasi-static test results for laminated samples (a) engineering and (b) true stress-strain curves

Table 7: Normalized quasi-static test results at room temperature for the laminated samples

Mechanical Properties	Sample 1	Sample 2	Sample 3	Average	Standard Dev.
Elastic Modulus [MPa/MPa]:	410	413	416	413	3
Yield Strength (0.2% offset) [MPa/MPa]:	0.98	0.97	1.02	0.99	0.03
True Ultimate Strength (MPa/MPa)	1.42	1.43	1.42	1.42	0.00
Engineering Ultimate Strength (MPa/MPa)	1.25	1.26	1.26	1.25	0.00
Engineering Fracture Strain [%]:	20	21	20	20	0
Strength coefficient, H [MPa/MPa] (*):	1.93	1.95	1.94	1.94	0.01
Strain hardening exponent, n (*):	0.15	0.15	0.15	0.15	0.00
Poisson's Ratio:	0.31	0.32	0.28	0.30	0.02

The samples before and after the room temperature quasi-static test are shown below.

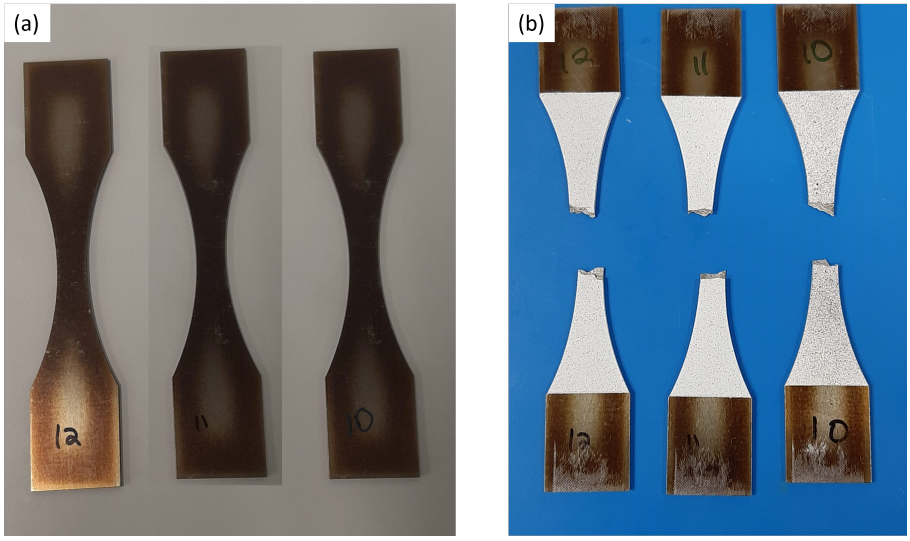

Figure 82: Room temperature quasi-static tested laminated samples, painted and speckled for strain measurement using DIC (a) before and (b) after testing

6.2.2 Quasi-Static Testing High Temperature

The results for the quasi-static testing at 150°C for the laminated samples are shown below. Three quasi-static tests were conducted and their results were averaged to estimate the quasi-static properties of the material. The results have been normalized by the yield strength of the electrical steel obtained at room temperature by Tolofari et al. [44] using ASTM E8/E345 samples [36, 37].

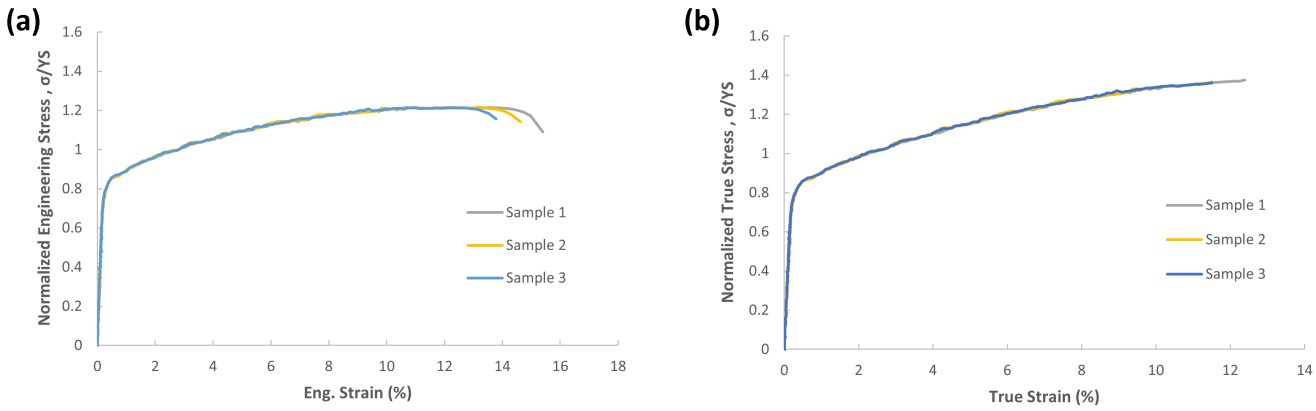

Figure 83: High temperature quasi-static test results for laminated samples (a) engineering and (b) true stress-strain curves

Table 8: Normalized quasi-static test results at high temperature for the laminated samples

Mechanical Properties	Sample 1	Sample 2	Sample 3	Average	Standard Dev.
Elastic Modulus [MPa/MPa]:	382	382	397	387	9
Yield Strength (0.2% offset) [MPa/MPa]:	0.84	0.84	0.85	0.84	0.01
True Ultimate Strength (MPa/MPa)	1.38	1.36	1.36	1.37	0.01
Engineering Ultimate Strength (MPa/MPa)	1.22	1.22	1.21	1.22	0.00
Engineering Fracture Strain [%]:	15	15	14	15	1
Strength coefficient, H [MPa/MPa] (*):	2.01	2.02	2.01	2.01	0.00
Strain hardening exponent, n (*):	0.18	0.18	0.18	0.18	0.00
Poisson's Ratio:	0.25	0.18	0.18	0.20	0.04

The samples before and after the elevated temperature quasi-static test are shown below.

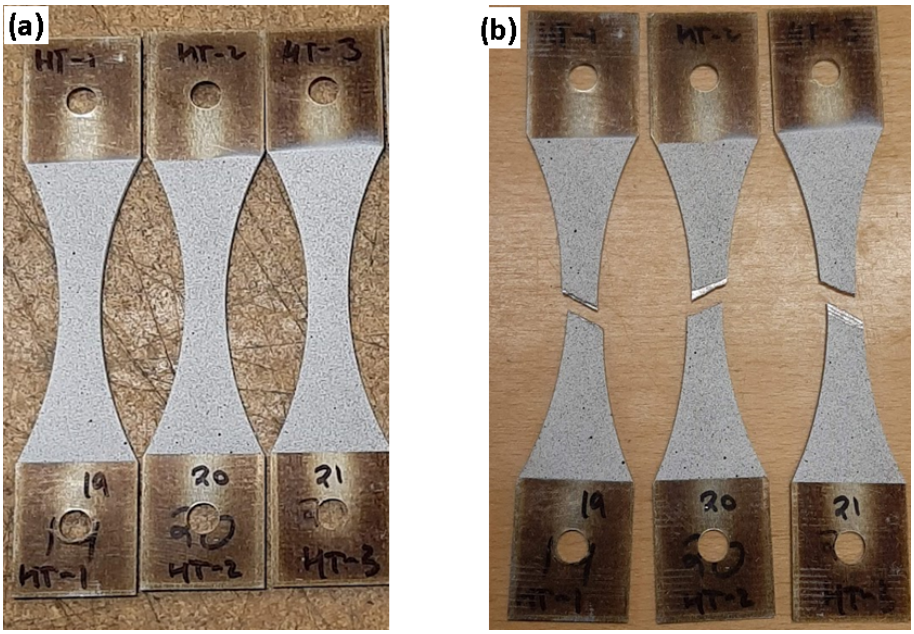

Figure 84: High temperature quasi-static tested laminated samples, painted and speckled for strain measurement using DIC (a) before and (b) after testing

6.2.3 Fatigue Testing Room Temperature

The results from the cyclic testing done at room temperature are shown below. Here a total of 21 tests were conducted and the stress amplitude was varied between 0.57 and 0.37. 2-3 tests were

conducted at each load level and the sample reached run-out at a normalized stress of 0.37. The results have been normalized by the yield strength of the electrical steel obtained at room temperature by Tolofari et al. [44] using ASTM E8/E345 samples [36, 37].

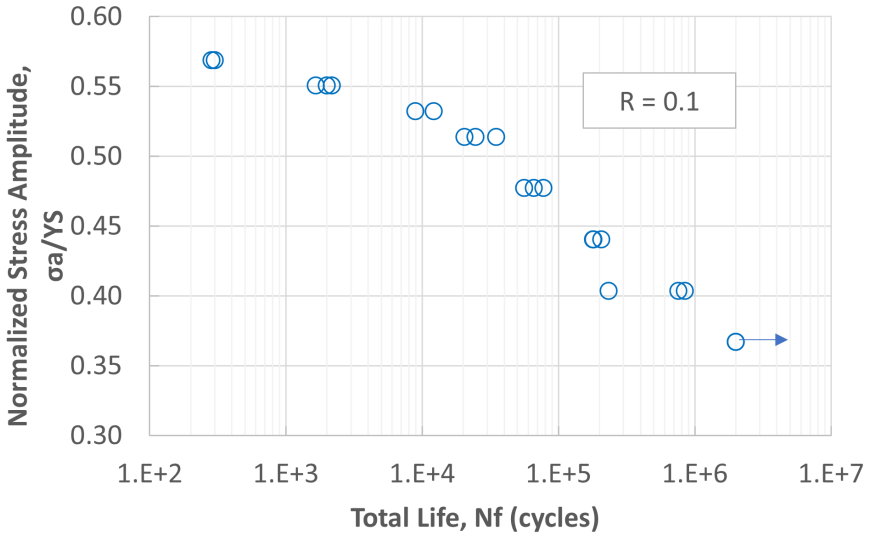

Figure 85: Fatigue results for room temperature tested laminated samples

Table 9: Normalized room temperature fatigue results for laminated samples

Test #	Sample #	R-ratio	Stress Amplitude (Mpa/MPa)	Loading Freq (Hz)	Total life, Nf (cycles)	Initial Sheet Failure, Ni (cycles)	Failure Location
1	29	0.1	0.57	0.5	285	-	within gauge section
2	28	0.1	0.57	0.5	300	-	within gauge section
3	34	0.1	0.55	0.5	1648	-	within gauge section
4	24	0.1	0.55	0.5	1997	-	within gauge section
5	40	0.1	0.55	0.5	2169	-	within gauge section
6	25	0.1	0.53	0.5	8915	-	within gauge section
7	33	0.1	0.53	0.5	12132	-	within gauge section
8	22	0.1	0.51	2	20423	-	within gauge section
9	36	0.1	0.51	2	24570	-	within gauge section
10	42	0.1	0.51	2	34918	-	within gauge section
11	31	0.1	0.48	3	55977	-	within gauge section
12	35	0.1	0.48	3	65950	-	within gauge section
13	38	0.1	0.48	3	77703	-	within gauge section
14	32	0.1	0.44	5	179292	-	within gauge section
15	39	0.1	0.44	5	180940	-	within gauge section
16	41	0.1	0.44	5	205124	-	within gauge section
17	27	0.1	0.40	10	233684	203200	within gauge section
18	26	0.1	0.40	10	757698	-	within gauge section
19	30	0.1	0.40	10	843747	-	within gauge section
20	23	0.1	0.37	10	2000000	-	Run-out
21	37	0.1	0.37	10	2000000	-	Run-out

The samples from the room temperature tests are shown below in figure 86. All samples that did not reach run-out, completely separated upon failure.

Figure 86: Fatigue samples for room temperature tested laminated samples

6.2.4 Fatigue Testing High Temperature

The results from the fatigue testing done at high temperature are shown below. The testing was brief and only 11 tests were conducted where the stress amplitude was varied between 0.53 and 0.37. 2 tests were conducted at each load level and the sample reached run-out at a normalized stress of 0.37. The results have been normalized by the yield strength of the electrical steel obtained at room temperature by Tolofari et al. [44] using ASTM E8/E345 samples [36, 37].

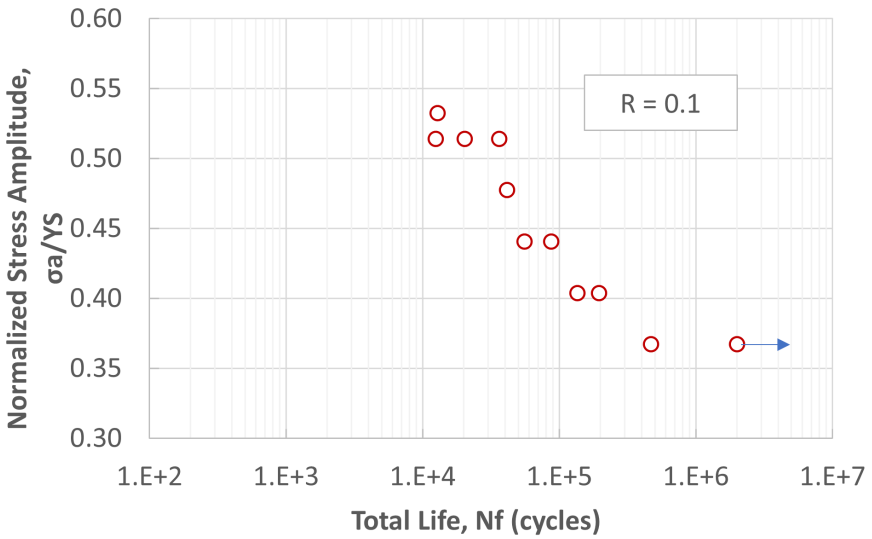

Figure 87: Fatigue results for high temperature tested laminated samples

Table 10: Normalized high temperature fatigue results for laminated samples

Test #	Sample #	R-ratio	Stress Amplitude (Mpa/MPa)	Loading Freq (Hz)	Total life, Nf (cycles)	Failure Location
1	50	0.1	0.53	0.5	12930	within gauge section
2	52	0.1	0.51	2	12471	within gauge section
3	48	0.1	0.51	2	20364	within gauge section
4	53	0.1	0.51	3	36302	within gauge section
5	46	0.1	0.48	3	41559	within gauge section
6	56	0.1	0.44	5	55583	within gauge section
7	45	0.1	0.44	5	87709	within gauge section
8	51	0.1	0.40	10	135929	within gauge section
9	47	0.1	0.40	10	196237	within gauge section
10	57	0.1	0.37	10	471123	within gauge section
11	49	0.1	0.37	10	2000000	Runout

The samples from the high temperature tests are shown below in figure 88. All samples that did not reach run-out, completely separated upon failure, with the exception of samples 55 which reached the displacement limit of 5mm.

Figure 88: Fatigue samples for high temperature tested laminated samples

6.3 Analysis

6.3.1 Quasi-Static Properties

The results of the testing done at both temperatures is shown below. Here both stress-strain curves are overlaid in figure 89 and the resulting mechanical properties are tabulated and compared in table 11.

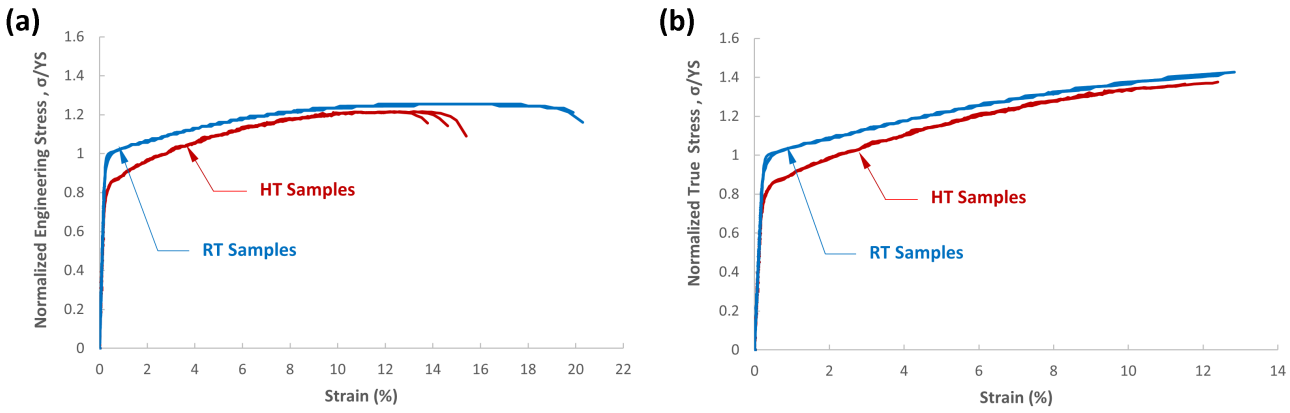

Figure 89: Quasi-static stress-strain curves of laminated samples

Table 11: Normalized quasi-static test results for the laminated samples

Mechanical Properties	Room Temperature	High Temperature	% Difference
Elastic Modulus [MPa/MPa]:	413 ± 3	387 ± 9	-6.7
Yield Strength (0.2% offset) [MPa/MPa]:	0.99 ± 0.03	0.84 ± 0.01	-18
True Ultimate Strength [MPa/MPa]:	1.42 ± 0.00	1.37 ± 0.01	-3.6
Engineering Ultimate Strength [MPa/MPa]:	1.25 ± 0.00	1.22 ± 0.00	-2.5
Engineering Fracture Strain [%]:	20 ± 0.4	15 ± 0.8	-33
Strength coefficient, H [MPa/MPa] (*):	1.94 ± 0.01	2.01 ± 0.00	3.5
Strain hardening exponent, n (*):	0.15 ± 0.00	0.18 ± 0.00	17
Poisson's Ratio	0.30 ± 0.02	0.20 ± 0.04	-50

6.3.2 Fatigue Properties

A comparison of the S-N curves for both the room temperature testing and high temperature testing of the laminated samples is shown below in figure 90.

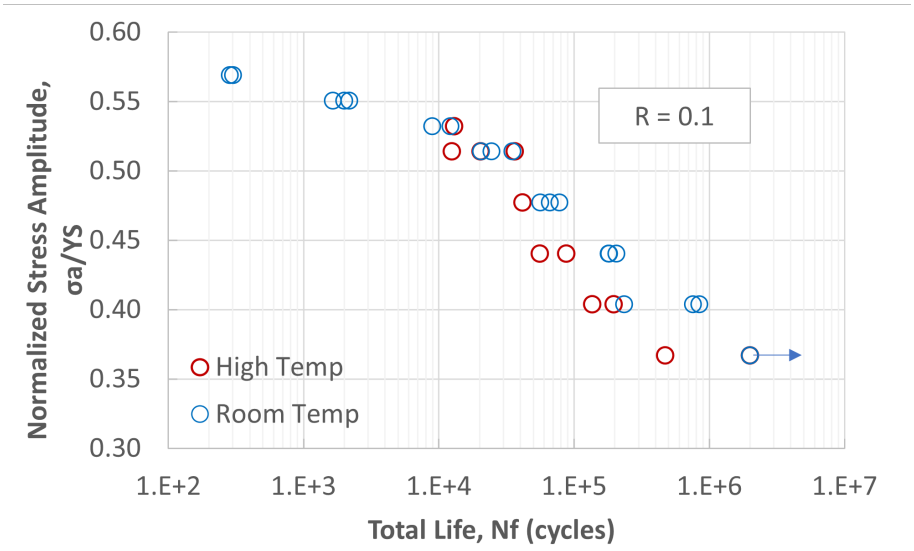

Figure 90: Fatigue results for room and high temperature tested laminated samples

A line of best fit was drawn for both the room temperature and high temperature results for the fatigue results in chapter 6 for the single sheet samples. However, the number of samples tested at high temperature was very small, and as a result, a Basquin model comparison cannot be done between the room temperature and high temperature results.

6.3.3 Fracture Analysis of Quasi-Static Testing

Below the fracture surfaces of the quasi-static tested samples will be discussed. One sample that was used for quasi-static testing at room temperature is shown below in figure 91. The sample fractured in an irregular manner where each sheet fractured at a different location. This behavior was observed with all of the laminated electrical steel samples. When looking at the fracture analysis below, some sheets may be difficult to see, and the reason for this is due to this phenomenon as it can be difficult to analyze multiple sheets on a fracture surface.

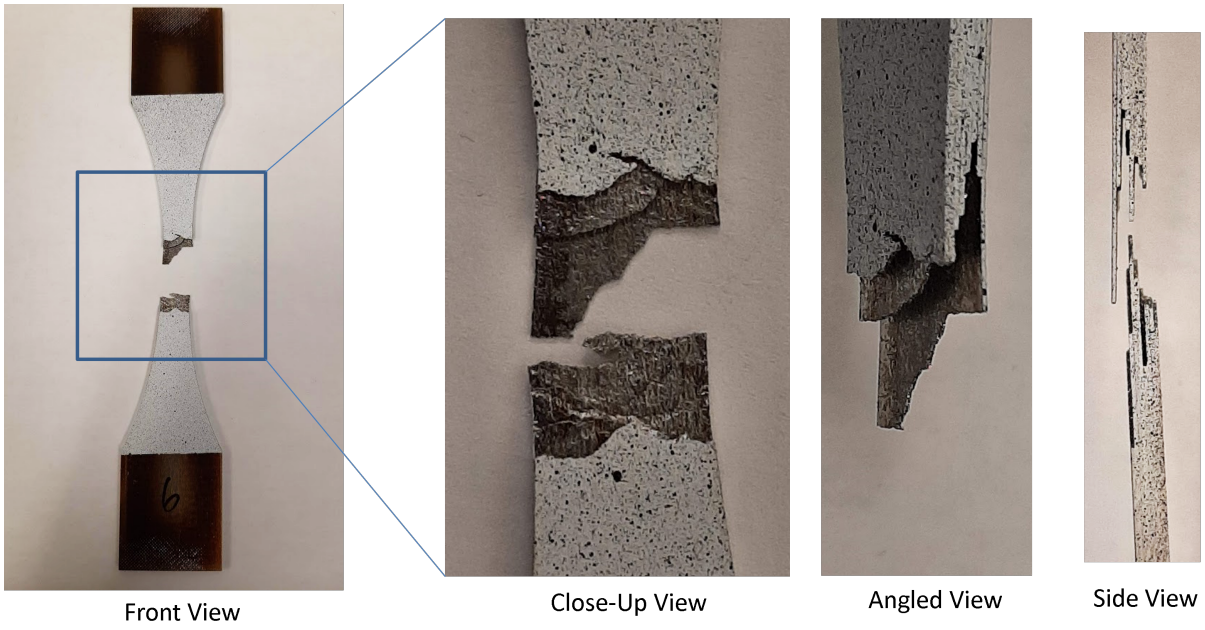

Figure 91: Fractured quasi-static laminated sample grain structure (a) front view (b) close-up to fracture surface (c) angled view (d) side view

The fracture surface for a QS samples at room temperature shown in figure 92. Here it is shows that each sheet had a different failure mechanisms along the cross section and these mechanisms are not all necessarily aligned and grouped together. The failure mechanisms at room temperature are local necking (shown with red arrows in figures 92b and 92c) and trans-granular cleavage facets (shown with green arrows in figures 92b and 92d). The same failure mechanism observed for the single sheet samples was observed here with the laminated samples. However, the samples do not align in failure mechanism along the thickness of the sample. This is likely due to a mis-alignment of the samples as all sheets are not perfectly aligned to one another (see figure 92a). Since they may not perfectly aligned when they were laminated, this small difference could have caused the

uneven failure mechanisms in the fracture surface and the uneven failure of individual sheets seen in figure 91 above.

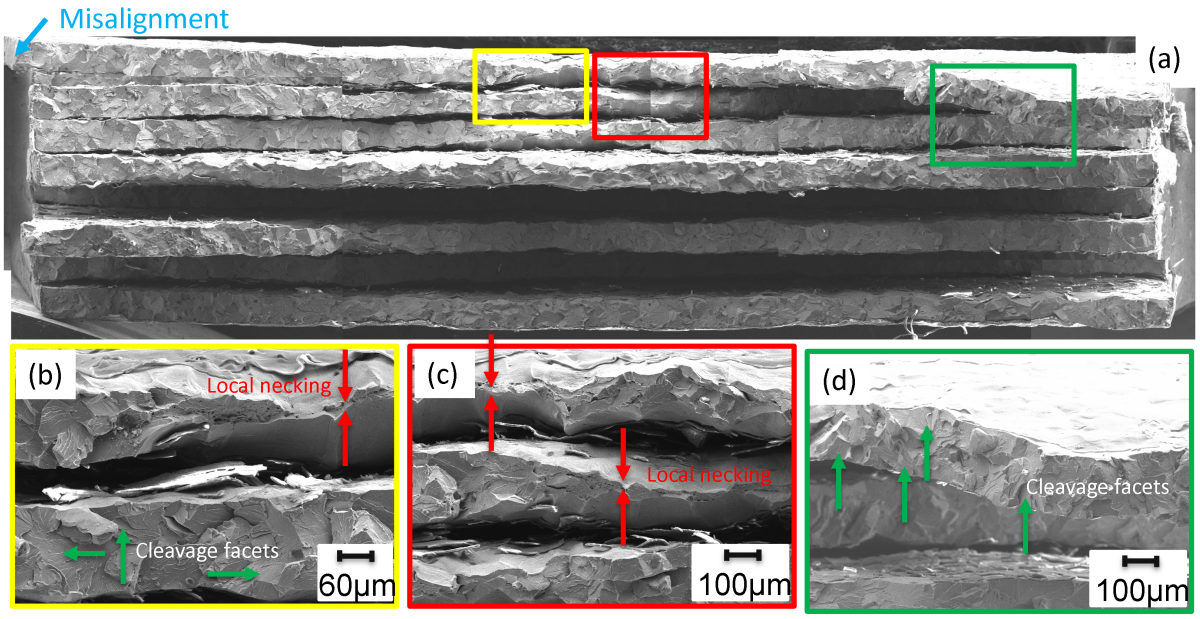

Figure 92: Fracture surface laminated quasi-static sample room temperature, (a) overall sample (b) cleavage facets and local necking (c) local necking (d) bending and cleavage facets

Below is the fracture surface for the laminated QS samples at high temperature. Here there is a lot of local necking that has occurred and this is indicated by the red arrows in figures 93b and 93d. In contrast to the room temperature samples, the high temperature samples all failed evenly at the 45 degree angle as seen in figure 84. At this high of temperature, the adhesive layer is known to weaken, and the result of this is a more even failure of the samples. There is still a slight misalignment present in this sample however, the misalignment is not obstructed by the adhesive layer, allowing the individual sheets to naturally align themselves.

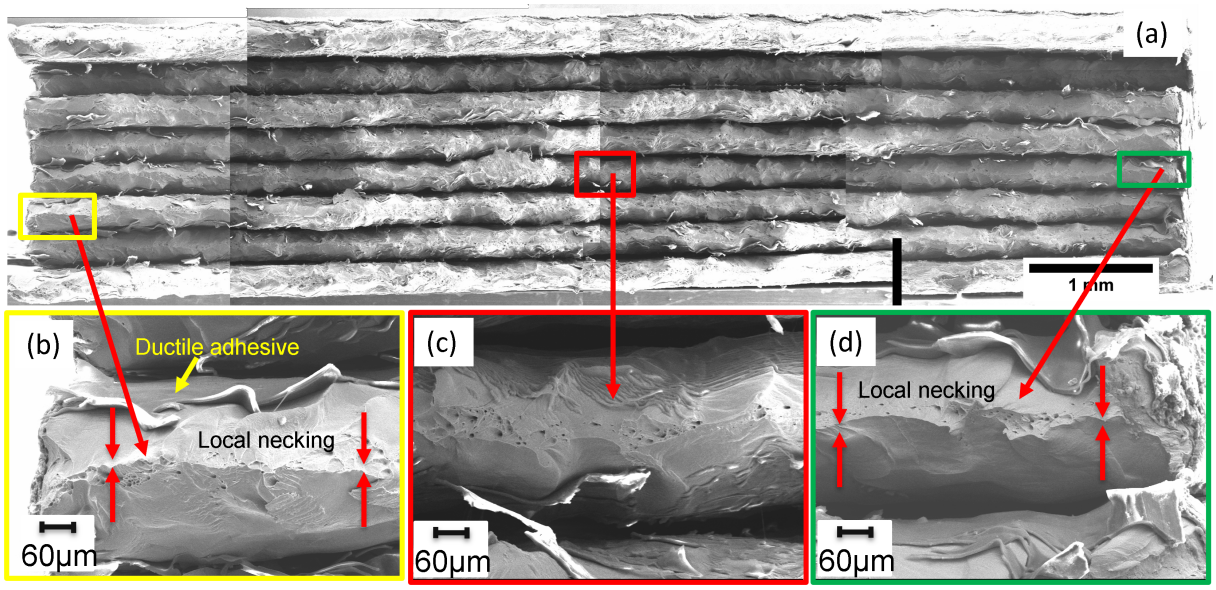

Figure 93: Fracture surface laminated quasi-static sample high temperature (a) overall sample (b) sheet 6, local necking (c) sheet 5, local necking (d) sheet 5, local necking

6.3.4 Fracture Analysis of Fatigue Testing

This section is an in-depth analysis of the fracture surfaces for the samples tested at room temperature and 150°C under cyclic loading. To understand the failure mechanisms occurring during cyclic testing, two samples at room temperature and two samples from the high temperature cyclic testing will be compared. At each temperature, one sample from the LCF and one sample from the HCF-regime will be compared to see the differences in the failure mechanism.

Sample 22 from the LCF regime of the room temperature testing is shown below in figure 94. This sample had a life of 20,423 cycles. This sample had a single failure, where the entire sample fractured at once. The fracture surface shows that only sheet 1 has a fatigue damage zone visible. Sheet 1 has a fatigue damage zone that is 1.05mm long, and its failure mode transitions to trans-granular cleavage facets, shown with green arrows on figure 94b. Sheet 2-8 only show trans-granular cleavage facets, and this indicates that the sheets all failed suddenly, with an exception to the first sheet. The first sheet had a crack initiate from the burr on the cutting edge (shown in figure 94c), and reached the length of 1.05mm, after which the sample overloaded (shown in figure 94b). Once the first sheet failed, the remaining 8 sheets were overloaded and also failed soon after. Similar to the single sheet samples some striations are also visible near the point of crack initiation, shown

with blue arrows on figure 94c.

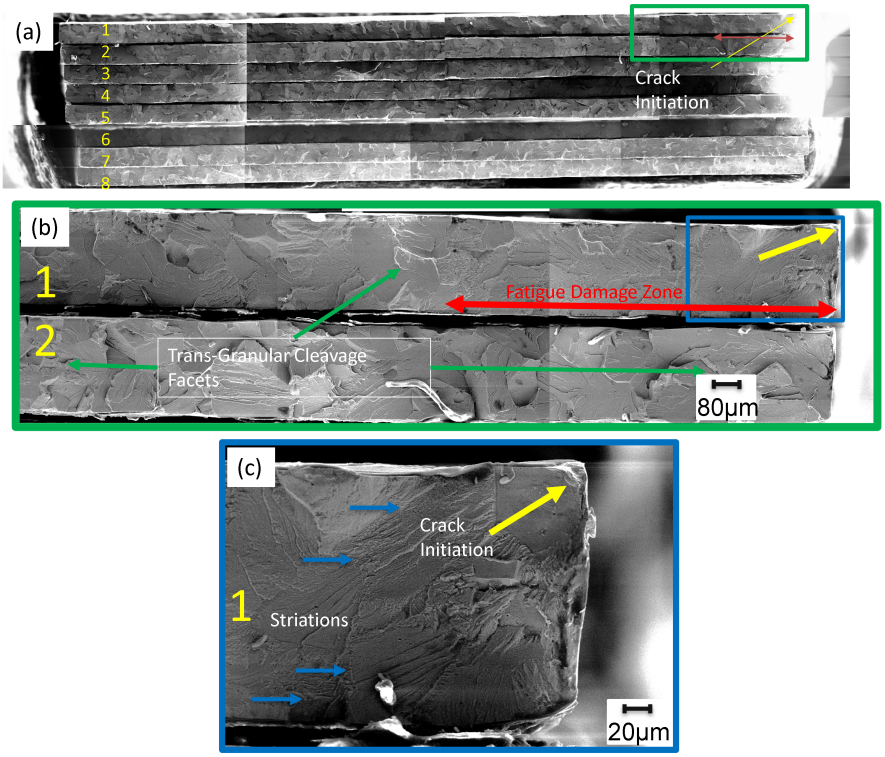

Figure 94: Fatigue samples for room temperature tested laminated sample Nf = 20,423 cycles (a) overall sample (b) close-up view for sheets 1 and 2 (c) fatigue damage zone for sheet 1

Sample 27 from the HCF regime of the room temperature testing is shown below in figure 95 (a) - (j). This sample had one sheet fail at 200,000 cycles before it had a sudden failure at the life of 233,684 cycles. This is the result of a two-step failure and is the only specimen that had a two-step failure in this testing. The first sheet that failed was sheet 1 and this sheet had a large fatigue damage zone (figure 95b and c) of 6.94mm, where it showed a mixed cleavage facet type of failure (shown in figure 95d indicated by the green arrows). Outside of this zone the failure mechanism transitioned to trans-granular cleavage facets. The next sheet that failed was sheet 4 shown in figure 95e. This is evident from its fatigue damage zone which has a length of 1.61mm and outside of this zone, the failure mechanism changed to trans-granular cleavage facets (highlighted with green arrows) shown in figure 95e. Here there is some striations visible indicated by the blue arrows in figure 95f. Once sheet 4 failed, the remaining sheets on the sample overloaded and the entire sample failed. It appears as if the sample had failed suddenly with emphasis on Sheet 8. Sheet 8, shown in figure 95g to 95j, shows some local necking (indicated by red arrows in figure 95i)

and trans-granular cleavage facets (highlighted with green arrows in figure 95h) and some mixed cleavage facets (highlighted with green arrows in figure 95j).

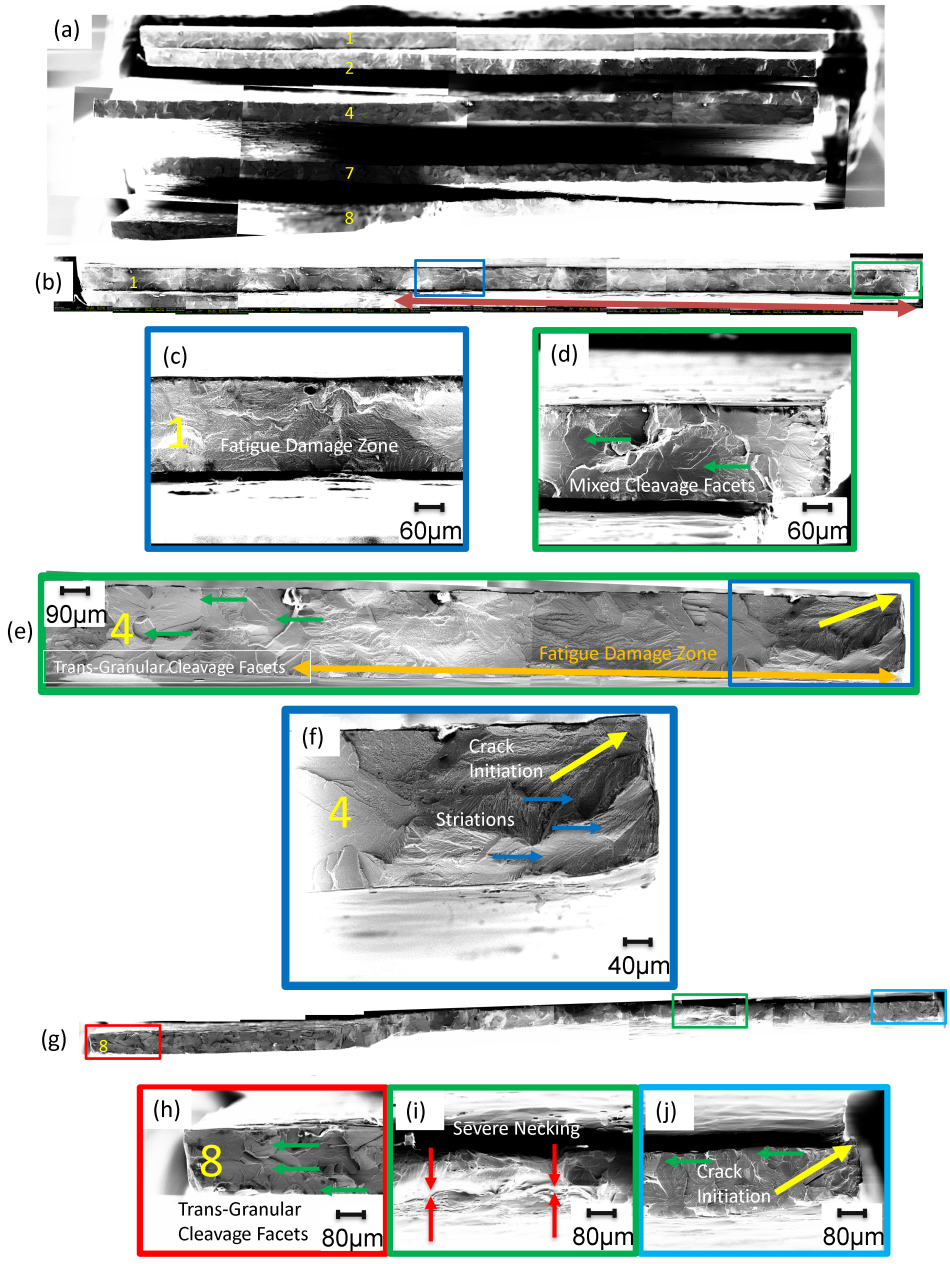

Figure 95: Fatigue sample for room temperature tested laminated sample, Nf = 233,684 cycles, (a) overall view of fracture surface (b) overall view of sheet 1 (c) fatigue damage zone (d) crack initiation zone (e) overall view of sheet 4 (f) crack initiation zone (g) overall view of sheet 8 (h) trans-granular cleavage facets (i) severe necking (j) crack initiation zone

Sample 48 from the LCF regime of the high temperature testing is shown below in figure 96. This sample had a life of 20,364 cycles and was tested at the same load as sample 22 shown in figure 94. This sample, had a single failure, where the entire sample fractured at once. The fracture surface shows that each sheet had a small fatigue damage zone visible. Sheet 1 has a fatigue damage zone that is 0.65mm long and is likely the first sheet that failed. The crack initiated from the burr and there is some striations (highlighted with blue arrows) shown in figure 96c. Its failure mode then changes to local necking (figure 96d). Likely sheet 1 failed first and then the other sheets followed at the same time. Sheet 8 failed in the same way with a similar sized fatigue damage zone of 0.35mm, with some visible striations in figure 96f and then the sample transitioned to local thinning. The sheets had a crack initiate from the burr on the cutting edge similar to the room temperature samples, after which the sample overloaded and failed.

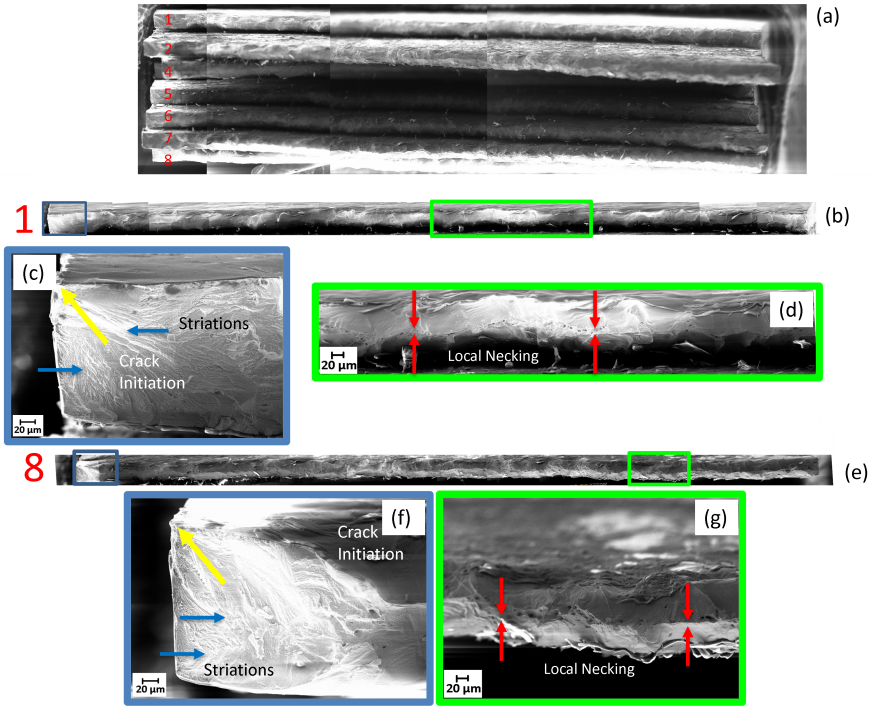

Figure 96: Fatigue sample for high temperature tested laminated sample, Nf = 20,364 cycles, (a) overall view of fracture surface (b) view of sheet 1 (c) crack initiation point of sheet 1 (d) some local necking on sheet 1 (e) view of sheet 8 (f) crack initiation point of sheet 8 (g) some local necking on sheet 8

Sample 51 from the HCF regime of the high temperature testing is shown below in figure 97. This

sample had a life of 135,929 cycles before it had a sudden failure. This sample was tested at the same load level as sample 27 shown in figure 95. This fracture was a single, sudden failure. The first sheet that failed was sheet 5, this sheet had a large fatigue damage zone of 6.7mm, where it showed a mixed cleavage facet type of failure (highlighted with green arrows) as shown in figure 97e and 97f. Outside of this zone the failure mechanism transitioned to local necking shown in figure 97g. The next sheet that failed is likely sheet 1 shown in figure 97b. This is evident from its fatigue damage zone which has a length of 0.35mm and outside of this zone, the failure mechanism changed to local necking (figure 97c). Once sheet 5 failed, the entire sample failed suddenly.

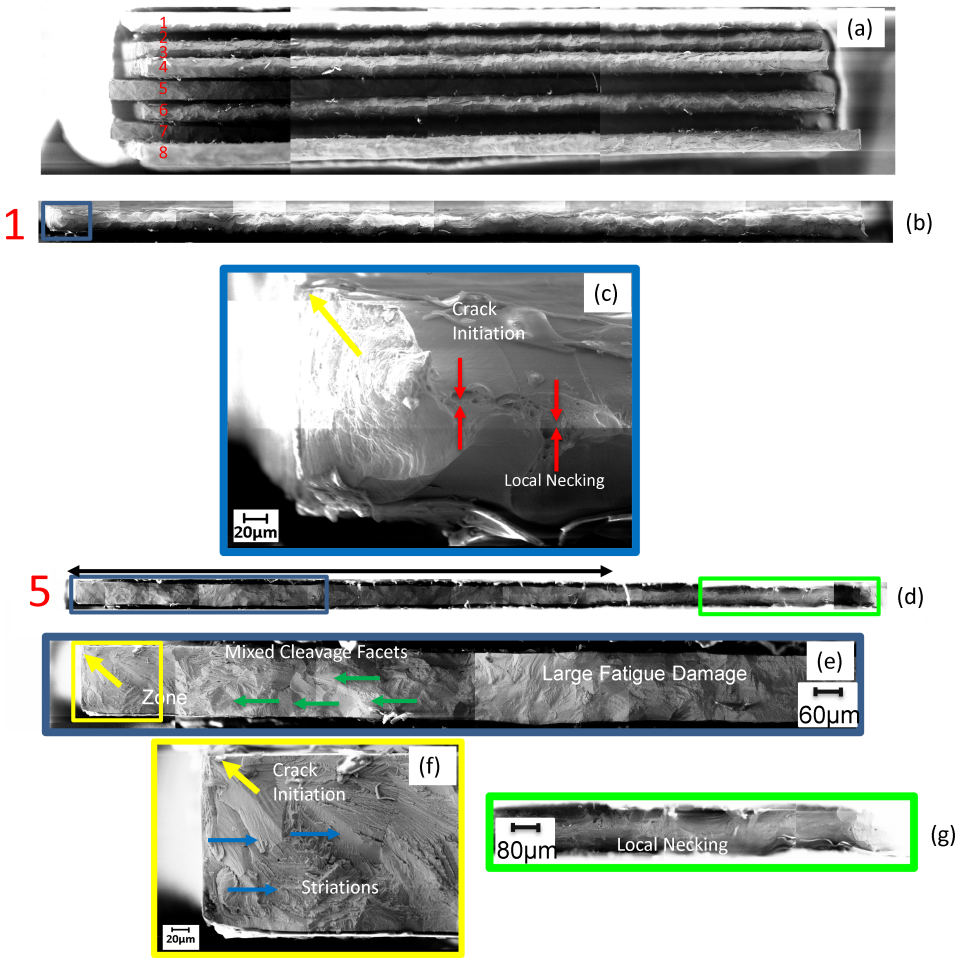

Figure 97: Fatigue sample for high temperature tested laminated sample, Nf = 135,929 cycles, (a) overall view of fracture surface (b) view of sheet 1 (c) crack initiation point of sheet 1 (d) view of sheet 5 (e) fatigue damage zone of sheet 5 (f) crack initiation point on sheet 5 (g) local necking on sheet 5

6.4 Discussion

6.4.1 Quasi-Static

The results of the testing done at both temperatures is overlaid in figure 89 and the resulting mechanical properties are tabulated and compared in table 11. These results show that the elastic modulus, yield strength, and ultimate tensile strength. This is the expected behavior as documented by Fortese et al. [41], where he observed a similar decrease in these mechanical properties at elevated temperatures. However, since the laminating adhesive broke down at 150°C, this temperature can be considered to be a limit for the material as beyond this temperature, the sample will de-laminate. Additionally, the fracture surface and failure mechanisms observed in figure 92 at room temperature is expected as this is the same findings as Bode et al. [38], where they found that under quasi-static loading, the specimens undergo a ductile failure, show trans-granular cleavage facets and show that the failure mechanism transitions to global necking. At 150° each sheet on the sample undergoes global necking (see figure 93) which is a distinct finding of this research. The laminated samples is behaving similarly in many respects to the single sheet sample as discussed in chapter 5, and the change in failure mechanism is written in great detail there.

Figures 98 and 99 show the overlaid quasi-static test results for both the room temperature testing and high temperature testing of single and laminated sheets. This is to compare the effects of the lamination process on the mechanical strength. This is important to understand as the electrical steel will be laminated when used in electric motor applications and it is important to understand the effect of the adhesive to ensure there is no detrimental effects to the mechanical strength.

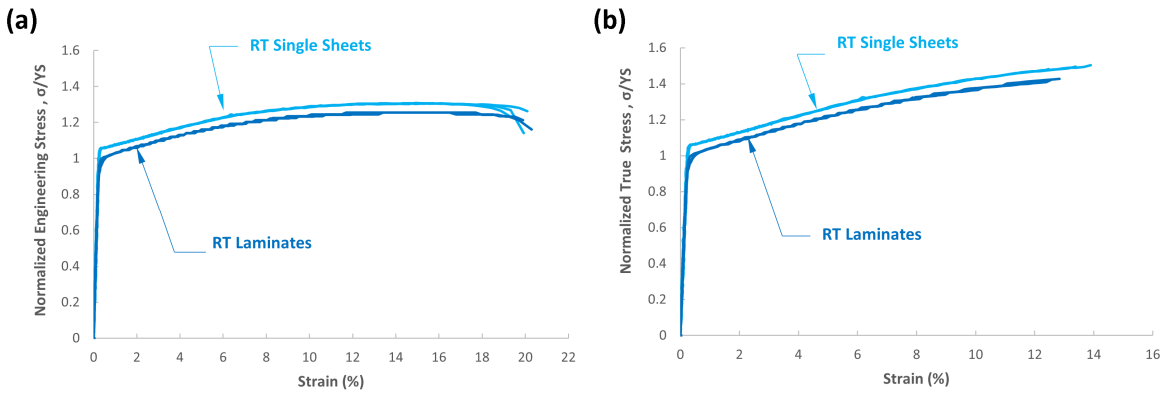

Figure 98: Comparison of quasi-static curves between laminated samples and sheet samples at room temperature

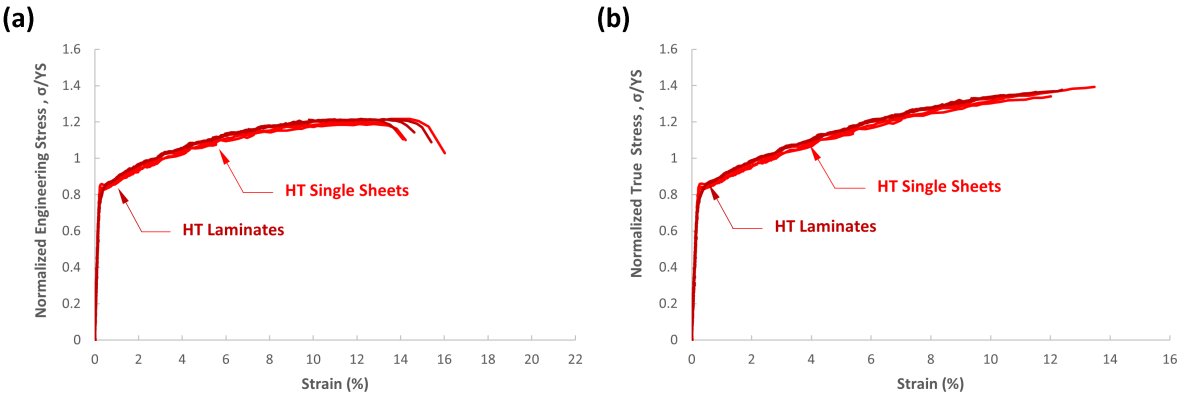

Figure 99: Comparison of quasi-static curves between laminated samples and sheet samples at 150°C

The high temperature results in figure 99 shows that there only a small difference between the test results for the laminated samples and the single sheet samples. This indicates that the laminating process has no significant effect at 150°. The room temperature results in figure 98 show a slight difference between the two sample geometries. The single sample and laminated sample stress-strain curves at room temperature differ slightly. However, the difference is minor and there does not appear to he a significant effect of the adhesive here. The samples are however closer in behavior at 150°C than at room temperature. The reason why the laminated samples differ in behavior more at room temperature is a result of the adhesive that holds the sheets together. The adhesive restricts the movement of the individual sheets, and doesn't allow the sheets to elongate independent of each other. This causes some sheets to yield in a more uneven manner due to the misalignment of

the sheets shown above in figure 92. This is not seen however in the high temperature results as this adhesive has been known to break down at 150°C and the individual sheets can de-laminate at this temperature. In general however, the effect of the adhesive layer is very minor and does not appear to effect the quasi-static properties of this material.

6.4.2 Fatigue

The fatigue results in figure 90 show that as the temperature increases to 150°C the fatigue life decreases in general. This is the expected trend, as this decrease in overall life is confirmed by Dehmani et al. [47] when he tested electrical steel at 180°C and saw a similar decrease in the overall life of the samples. This failure mechanism is also similar to what is expected for electrical steel as Schayes et al. [40] also found that at room temperature the failure was both trans-granular and inter-granular in nature, which transitioned to a sudden brittle fracture of the material. The failure mechanism at high temperature is global necking outside the fatigue damage zones, which are smaller in size compared to the room temperature samples. A more detailed analysis on this behavior is discussed in chapter 6 for the single sheet samples.

Figure 100 and 101 show the comparison of the stress life curve values for the room and high temperature fatigue testing of the single sheet samples and the laminated samples. Here there is a very good overlap of these two tests in the mid to high cycle fatigue results. This shows that the laminated samples behave very similarly to the single sheet samples.

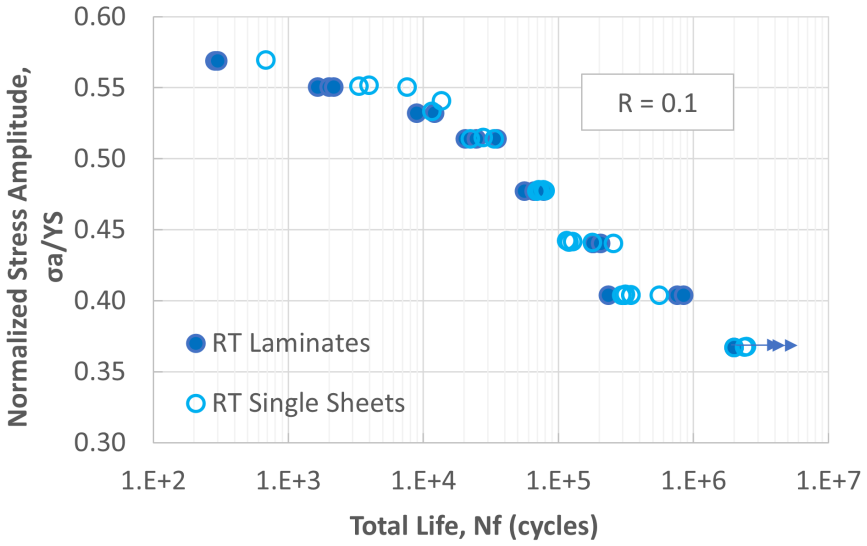

Figure 100: Stress life curve of laminated samples compared to single sheet samples at room temperature

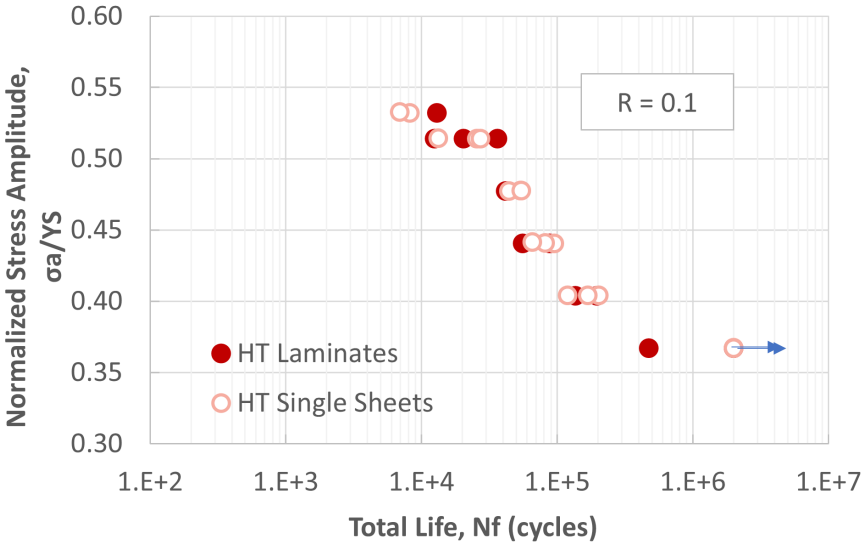

Figure 101: Stress life curve of laminated samples compared to single sheet samples at high temperature

While the overall life of the samples are very similar at room temperature and high temperature, the failure mechanism is slightly different. For the laminated samples, the main failure mechanism for the room temperature testing is a mixed cleavage facet failure in the fatigue damage zone and trans-granular cleavage facets outside the fatigue damage zone. For the high temperature sam-

ples, the main failure mechanism was global necking, and this was prevalent outside of the fatigue damage zone. This is the same failure mechanism observed for the single sheet samples discussed in chapter 6. However, the first sheet to fail in the laminated stack is different depending on the conditions. At room temperature the first sheet to fail was always the outer-most sheet (sheet 1 or 8) however at high temperatures it is possible for any of the sheets to be the first to fail due to the adhesive weakening at high temperatures. This was observed in sample 51 from figure 97. This sample had a life of 135,929 cycles and the first sheet to fail was the fifth sheet in the stack. This is a result of the adhesive weakening. Since the sample is pinned at both ends in the high temperature test setup, as shown in section 3.3 figure 49, once the adhesive weakens, the sample acts more similar to 8 individual sheets rather than as a single stack. What these findings conclude is that it is possible to have an internal sheet be the cause of the failure at high temperatures, and in general, the first sheet to fail is likely the outermost sheet (1 or 8).

The fatigue damage zone size for the first sheet to fail, increases dramatically in the high cycle regime for both the room and high temperature samples, and the cracks always initiated from the burr region of the cutting edge as seen in figures 94 to 97. This shows that the stack fails in two steps. Firstly, one sheet has a crack initiation and accumulates fatigue damage. After this sheet has a sudden failure, the entire stack fails. To add to this, sample 27 was observed to have this behavior during the test. Its first sheet failed at approximately 200,000 cycles and then the sample had a sudden failure at 233,684 cycles. The fracture analysis confirmed that the first sheet accumulated a lot of fatigue damage, and that the fatigue damage was then accumulated on the fourth sheet. This shows that the failure damage is not equally distributed across all of the sheets in the stack.

6.5 Chapter Conclusion

The laminated electrical steel samples were both tensile and cyclic-tested at room temperature and at an elevated temperature of 150°. After analyzing the results the following conclusions can be made based off the findings of the research.

- The laminated samples, and the single sheet samples show great overlap as they behave very similarly when comparing the quasi-static results and the fatigue results.
- In terms of the fracture mechanism, they are also very comparable where the same failure

mechanisms are shared between the single sheet samples and the laminated samples.

- For the laminated samples, the main failure mechanism for the room temperature testing was a mixed cleavage facet failure in the fatigue damage zone and trans-granular cleavage facets outside the fatigue damage zone. For the high temperature samples, the main failure mechanism was global necking, and this was prevalent outside of the fatigue damage zone.

- The fatigue damage zone for the first sheet to fail, increases dramatically in the high cycle regime for both the room and high temperature samples, and the cracks always initiated from the burr region of the cutting edge as seen in figures 94 to 97.

- Fatigue damage is not evenly distributed, and is concentrated at a single sheet, which fails before the subsequent sheets

- At room temperature the first sheet to fail was always the outer-most sheet (sheet 1 or 8) however at high temperatures it is possible for any of the sheets to be the first to fail due to the adhesive losing its strength at high temperatures.

Conclusion, Research Contribution and Future Work

Thesis Conclusions

This thesis characterized the quasi-static, and fatigue properties of electrical steel. Chapter 4 outlined the microstructural analysis that was completed on the electrical steel before the testing began and then discussed the quasi-static properties of stamped, single sheet electrical steel at room temperature and at 150C. Chapter 5 discussed the fatigue properties of the stamped, single sheet electrical steel at room temperature and then investigated the fatigue behavior at 150°C. Chapter 6 then investigated the effects of laminating on the quasi-static and fatigue properties of electrical steel at both room temperature and at elevated temperatures.

The material used in this study was a 3% silicon non-oriented electrical steel. In the beginning of the thesis, it was verified that the composition, the grain structure, grain sizes and grain orientation was correct and was what is expected for this material. In conducting the quasi-static testing at room temperature the behavior was verified to match the behavior found in literature and the behavior at 150°C was a new finding. Similarly for the fatigue testing, the room temperature results helped to verify the findings in the literature and the findings as 150°C was a new addition to the current knowledge for electrical steel. Finally, the quasi-static and fatigue testing done on the laminated samples showed that they behave almost the same as the single sheet samples in terms of the mechanical behavior and the failure mechanisms with some key differences in how the laminated samples fail. There is a very significant and important change to the material behavior at 150°C compared to how it behaves at room temperature. This finding is important as it will help engineers to better design electric motors to perform well, and not fail under repeated loading and under high temperatures. The findings of the laminated electrical steel testing in particular can be extrapolated to see how an electric motor can fail. In this research, the laminated stack had its fatigue damage concentrated on a single sheet in the laminated stack. Once that sheet reached the critical crack length at the end of its life, that sheet will fail and cause the remaining stack to fail due to an overloading. These findings are very important and deserve to be studied even further as the worldwide transportation industry moves towards electrification. As the number of applications increases for the electric motor, it will become more and more critical that the behavior of electrical steel be better understood to ensure that a reliable design is made in each application.

Research Contributions

This research presented in this thesis has contributed greatly to current literature available for electrical steel by adding new found knowledge and confirming the observations made by others on this specific electrical steel. The findings in Chapters 4-6 are very similar to what is available in literature as the microstructure, the quasi-static and the fatigue properties at room temperature for the single sheet samples align well with existing research that has been conducted by others.

Existing literature has shown that the failure mechanisms in great detail for room temperature quasi-static and fatigue testing. However, the failure mechanism that occurs at 150° was not available in the literature, and the in-depth analysis conducted in this research helps to contribute to the literature. Additionally, the severe thinning that occurs at 150° as well as the complete reduction in the cross sectional area is a point that was not available in the literature at the time of this research and is an important contribution to the current web of knowledge.

Another contribution is the findings of Chapter 6. There is no literature that discusses the effects of laminating on the quasi-static and fatigue properties of electrical steel. This research found that in quasi-static and fatigue loading, the laminated samples behave almost the same as the single sheet samples in terms of their mechanical properties. The failure mechanisms are also the same between the single sheet and the laminated samples however, for the laminated samples the behavior is not evenly distributed across the 8 sheets. In quasi-static loading, The crack initiates typically on one sheet, and once this sheet fails, the rest of the sample has a rapid and sudden failure. In fatigue testing, the fatigue damage is not evenly distributed across all of the sheets rather, it is concentrated at a single sheet which fails before the subsequent sheets. At room temperature the research found that the first sheet to fail was always the outer-most sheet and at high temperatures it is possible for any of the sheets to be the first to fail due to the adhesive losing its strength at high temperatures.

Recommended Future Work

Concluding the research, there is still some open questions that have yet to be answered. One observation that is not yet fully understood is the effect of the higher temperature on the failure mechanism, and why at 150°C, severe thinning occurs. Research into the failure mechanism and why there is a transition between the different failure mechanisms and how this contributes to the thinning of the material is needed to better understand the material behavior of electrical steel. This information will help to better understand the decrease in fatigue life and decrease in quasi-static properties of electrical steel. EBSD is a great method to see the strain response at room and higher temperatures and could help to better understand this change in failure mechanism of electrical steel.

One observation that was not quantified was the effect of the residual stresses on the material. It is recommended to measure the residual stresses on the cutting edge of the samples in detail and then expand the analysis to see what effect their presence has on the fatigue and quasi-static properties of stamped electrical steel. It is also recommended to measure the quasi-static properties using the correct sample geometry that follows ASTM E8 [36] and ASTM E345 [37] standards to better understand the stamping effect on the quasi-static results as the results in this thesis were not done using this geometry. Using the correct geometry and a DIC can help to see if the effect stamping has on the strain response of the material.

Letters of Copyright Permission

The following is included in Elsevier copyright permissions policies:

Authors can include their articles in full or in part in a thesis or dissertation for non-commercial purposes. No written permission from Elsevier is necessary. This right extends to the posting of your thesis to your university's repository provided that if you include the published journal article, it is embedded and not separately downloadable.

Below are the licenses obtained for the use of figures that were created and published by others. Proper referencing within this thesis has been done to give credit to the respective figures used in chapters 2, 3, 4, 5 and 6.

ELSEVIER LICENSE
TERMS AND CONDITIONS

Apr 01, 2023

This Agreement between University of Waterloo -- Gurmeet Gill ("You") and Elsevier ("Elsevier") consists of your license details and the terms and conditions provided by Elsevier and Copyright Clearance Center.

License Number	5520490276779
License date	Apr 01, 2023
Licensed Content Publisher	Elsevier
Licensed Content Publication	Journal of Magnetism and Magnetic Materials
Licensed Content Title	Developments in the production of grain-oriented electrical steel
Licensed Content Author	Zhaosuo Xia,Yonglin Kang,Quanli Wang
Licensed Content Date	Dec 1, 2008
Licensed Content Volume	320
Licensed Content Issue	23
Licensed Content Pages	5

JOHN WILEY AND SONS LICENSE
TERMS AND CONDITIONS

Apr 01, 2023

This Agreement between University of Waterloo -- Gurmeet Gill ("You") and John Wiley and Sons ("John Wiley and Sons") consists of your license details and the terms and conditions provided by John Wiley and Sons and Copyright Clearance Center.

License Number	5520491176053
License date	Apr 01, 2023
Licensed Content Publisher	John Wiley and Sons
Licensed Content Publication	Wiley Books
Licensed Content Title	Definitions and Units
Licensed Content Date	Feb 29, 2008
Licensed Content Pages	21

SPRINGER NATURE LICENSE
TERMS AND CONDITIONS

Mar 16, 2023

This Agreement between University of Waterloo -- Gurmeet Gill ("You") and Springer Nature ("Springer Nature") consists of your license details and the terms and conditions provided by Springer Nature and Copyright Clearance Center.

License Number	5510990512706
License date	Mar 16, 2023
Licensed Content Publisher	Springer Nature
Licensed Content Publication	Russian Journal of Nondestructive Testing
Licensed Content Title	Evaluating the level of residual stresses in anisotropic electric steel
Licensed Content Author	G. S. Korzunin et al
Licensed Content Date	Feb 8, 2017

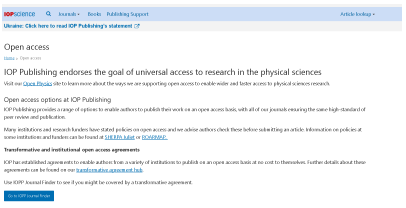

ELSEVIER LICENSE
TERMS AND CONDITIONS

Apr 01, 2023

This Agreement between University of Waterloo -- Gurmeet Gill ("You") and Elsevier ("Elsevier") consists of your license details and the terms and conditions provided by Elsevier and Copyright Clearance Center.

License Number	5520490858076
License date	Apr 01, 2023
Licensed Content Publisher	Elsevier
Licensed Content Publication	Journal of Magnetism and Magnetic Materials
Licensed Content Title	Recent development of non-oriented electrical steel sheets
Licensed Content Author	H. Shimanaka,Y. Ito,K. Matsumura,B. Fukuda
Licensed Content Date	Mar 1, 1982
Licensed Content Volume	26
Licensed Content Issue	1-3
Licensed Content Pages	8

ELSEVIER LICENSE
TERMS AND CONDITIONS

Apr 01, 2023

This Agreement between University of Waterloo -- Gurmeet Gill ("You") and Elsevier ("Elsevier") consists of your license details and the terms and conditions provided by Elsevier and Copyright Clearance Center.

License Number	5520491345626
License date	Apr 01, 2023
Licensed Content Publisher	Elsevier
Licensed Content Publication	Materials Chemistry and Physics
Licensed Content Title	Effect of silicon content in steel and oxidation temperature on scale growth and morphology
Licensed Content Author	Amine Alaoui Mouayd,Alexey Koltsov,Elaine Sutter,Bernard Tribollet
Licensed Content Date	Feb 14, 2014
Licensed Content Volume	143
Licensed Content Issue	3
Licensed Content Pages	9

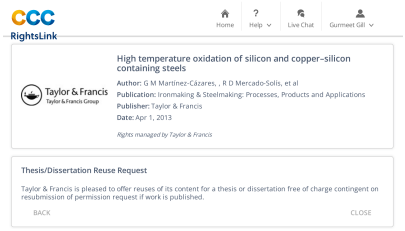

ELSEVIER LICENSE
TERMS AND CONDITIONS

Apr 01, 2023

This Agreement between University of Waterloo -- Gurmeet Gill ("You") and Elsevier ("Elsevier") consists of your license details and the terms and conditions provided by Elsevier and Copyright Clearance Center.

License Number	5520500336712
License date	Apr 01, 2023
Licensed Content Publisher	Elsevier
Licensed Content Publication	Materials Science and Engineering: A
Licensed Content Title	Microstructure and mechanical property connections for a punched non-oriented electrical steel lamination
Licensed Content Author	Aroba Saleem,Dina Goldbaum,Nicolas Brodusch,Raynald Gauvin,Richard R. Chromik
Licensed Content Date	May 16, 2018
Licensed Content Volume	725
Licensed Content Issue	n/a
Licensed Content Pages	10

ELSEVIER LICENSE
TERMS AND CONDITIONS

Apr 01, 2023

This Agreement between University of Waterloo -- Gurmeet Gill ("You") and Elsevier ("Elsevier") consists of your license details and the terms and conditions provided by Elsevier and Copyright Clearance Center.

License Number	5520500465387
License date	Apr 01, 2023
Licensed Content Publisher	Elsevier
Licensed Content Publication	Journal of Magnetism and Magnetic Materials
Licensed Content Title	The influence of punching process on residual stress and magnetic domain structure of non-oriented silicon steel
Licensed Content Author	Hongzhi Cao,Linpo Hao,Jingwen Yi,Xianglin Zhang,Zhonghan Luo,Shenglin Chen,Rongfeng Li
Licensed Content Date	May 15, 2016
Licensed Content Volume	406
Licensed Content Issue	n/a
Licensed Content Pages	6

SPRINGER NATURE LICENSE
TERMS AND CONDITIONS

Apr 01, 2023

This Agreement between University of Waterloo -- Gurmeet Gill ("You") and Springer Nature ("Springer Nature") consists of your license details and the terms and conditions provided by Springer Nature and Copyright Clearance Center.

License Number	5520500761117
License date	Apr 01, 2023
Licensed Content Publisher	Springer Nature
Licensed Content Publication	Journal of Wuhan University of Technology-Mater. Sci. Ed.
Licensed Content Title	Fatigue cracking characterization of high grade non-oriented electrical steels
Licensed Content Author	Liying Du 杜丽影 et al
Licensed Content Date	Dec 14, 2017

ELSEVIER LICENSE
TERMS AND CONDITIONS

Apr 01, 2023

This Agreement between University of Waterloo -- Gurmeet Gill ("You") and Elsevier ("Elsevier") consists of your license details and the terms and conditions provided by Elsevier and Copyright Clearance Center.

License Number	5520520040768
License date	Apr 01, 2023
Licensed Content Publisher	Elsevier
Licensed Content Publication	International Journal of Fatigue
Licensed Content Title	Quasi-static and cyclic failure behavior of electric sheet material
Licensed Content Author	B. Bode,A. Brueckner-Foit,F. Zeismann
Licensed Content Date	Jan 1, 2016
Licensed Content Volume	82
Licensed Content Issue	n/a
Licensed Content Pages	11

ELSEVIER LICENSE
TERMS AND CONDITIONS

Apr 01, 2023

This Agreement between University of Waterloo -- Gurmeet Gill ("You") and Elsevier ("Elsevier") consists of your license details and the terms and conditions provided by Elsevier and Copyright Clearance Center.

License Number	5520500942341
License date	Apr 01, 2023
Licensed Content Publisher	Elsevier
Licensed Content Publication	Journal of Materials Processing Technology
Licensed Content Title	Laser welding of laminated electrical steels
Licensed Content Author	Hongze Wang,Yansong Zhang,Shuhui Li
Licensed Content Date	Apr 1, 2016
Licensed Content Volume	230
Licensed Content Issue	n/a
Licensed Content Pages	10

MDPI Open Access Information and Policy

All articles published by MDPI are made immediately available worldwide under an open access license. This means:

- everyone has free and unlimited access to the full-text of all articles published in MDPI journals;
- everyone is free to re-use the published material if proper accreditation/citation of the original publication is given;
- open access publication is supported by the authors' institutes or research funding agencies by payment of a comparatively low **Article Processing Charge (APC)** for accepted articles.

Permissions

No special permission is required to reuse all or part of article published by MDPI, including figures and tables. For articles published under an open access Creative Common CC BY license, any part of the article may be reused without permission provided that the original article is clearly cited. Reuse of an article does not imply endorsement by the authors or MDPI.

ELSEVIER LICENSE
TERMS AND CONDITIONS

Apr 01, 2023

This Agreement between University of Waterloo -- Gurmeet Gill ("You") and Elsevier ("Elsevier") consists of your license details and the terms and conditions provided by Elsevier and Copyright Clearance Center.

License Number	5520520235070
License date	Apr 01, 2023
Licensed Content Publisher	Elsevier
Licensed Content Publication	Acta Materialia
Licensed Content Title	Local mechanical behavior and slip band formation within grains of thin sheets
Licensed Content Author	Mark Henning,Horst Vehoff
Licensed Content Date	Mar 1, 2005
Licensed Content Volume	53
Licensed Content Issue	5
Licensed Content Pages	8

Bibliography

[1] Cullity, Bernard Denis, and Chad D. Graham. Introduction to Magnetic Materials. Piscataway, NJ: IEEE Press, 2009.

[2] Roha, Vladimír, Emil Spišák, Peter Mulidrán, and Janka Majerníková. "Basic Classification and Processing of Electrical Steels." The IJES. Accessed October 2, 2022. https://www.theijes.com/papers/vol9-issue7/Ser-1/A0907010106.pdf.

[3] Xia, Zhaosuo, Yonglin Kang, and Quanli Wang. "Developments in the Production of Grain-Oriented Electrical Steel." Journal of Magnetism and Magnetic Materials 320, no. 23 (2008): 3229–33. DOI: 10.1016/j.jmmm.2008.07.003.

[4] Kawano, Masaki, Toshiro Fujiyama, and Tatsuya Aoki. "Electrical Steels for High-Functional Automotive Electrical Components Corresponding to Energy Saving." KAWASAKI STEEL TECHNICAL REPORT. Accessed March 24, 2023. https://www.jfe-steel.co.jp/archives/en/ksc_giho/no.48/e48-047-052.pdf.

[5] Toyota Canada. "Toyota Mirai." 2023 Toyota Mirai - Hyrdrogen Fuel Cell Vehicle - Toyota Canada, March 25, 2023. https://www.toyota.ca/toyota/en/vehicles/mirai/overview.

[6] Li, Fangjie, Huigai Li, Yuan Wu, Dan Zhao, Bowen Peng, Hefei Huang, Shaobo Zheng, and Jinglin You. "Effect of Precipitates on Grain Growth in Non-Oriented Silicon Steel." Journal of Materials Research 32, no. 12 (2017): 2307–14. DOI: 10.1557/jmr.2017.115.

[7] Nakashima, Shozaburo, Kunihide Takashima, and Jiro Harase. "Effect of Silicon Content on Secondary Recrystallization in Grain-Oriented Electrical Steel Produced by Single-Stage Cold Rolling Process." ISIJ International 31, no. 9 (1991): 1007–12. DOI: 10.2355/isijinternational.31.1007.

[8] "Manufacturing Process." Manufacturing process - electrical steel- products - POSCO products. Accessed October 2, 2022. http://product.posco.com/homepage/product/eng/jsp/process/s91p2000720e.jsp.

[9] Xu, Haijie, Yunbo Xu, Youliang He, Sifei Cheng, Haitao Jiao, Steve Yue, and Jianping Li. "Two-Stage Warm Cross Rolling and Its Effect on the Microstructure, Texture and Magnetic Properties of an FE-6.5 Wt% Si Non-Oriented Electrical Steel." Journal of Materials Science 55, no. 26 (2020): 12525–43. DOI: 10.1007/s10853-020-04861-7.

[10] Ouyang, Gaoyuan, Xi Chen, Yongfeng Liang, Chad Macziewski, and Jun Cui. "Review of Fe-6.5Wt%Si High Silicon Steel a Promising Soft Magnetic Material for Sub-Khz Application." Journal of Magnetism and Magnetic Materials 481 (2019): 234–50. DOI: 10.1016/j.jmmm.2019.02.089.

[11] Korzunin, G. S., M. L. Lobanov, and L. V. Lobanova. "Evaluating the Level of Residual Stresses in Anisotropic Electric Steel." Russian Journal of Nondestructive Testing 52, no. 12 (2016): 710–15. DOI: 10.1134/s106183091612010x.

[12] Ye, Tie, Zhiwen Lu, and Chunhua Ma. "Evolution of Microstructure and Texture with the Low-Silicon in Non-Oriented Silicon Steel." IOP Conference Series: Earth and Environmental Science 170 (2018): 042086. DOI: 10.1088/1755-1315/170/4/042086.

[13] Drumond, J., O. Girina, J. F. da Silva Filho, N. Fonstein, and C. A. Silva de Oliveira. "Effect of Silicon Content on the Microstructure and Mechanical Properties of Dual-Phase Steels." Metallography, Microstructure, and Analysis 1, no. 5 (2012): 217–23. DOI: 10.1007/s13632-012-0034-8.

[14] Shimanaka, H., Y. Ito, K. Matsumara, and B. Fukuda. "Recent Development of Non-Oriented Electrical Steel Sheets." Journal of Magnetism and Magnetic Materials 26, no. 1-3 (1982): 57–64. DOI: 10.1016/0304-8853(82)90116-0.

[15] Yamaji, T., M. Abe, Y. Takada, K. Okada, and T. Hiratani. "Magnetic Properties and Workability of 6.5% Silicon Steel Sheet Manufactured in Continuous CVD Siliconizing Line." Journal of Magnetism and Magnetic Materials 133, no. 1-3 (1994): 187–89. DOI: 10.1016/0304-8853(94)90521-5.

[16] Liang, Yong Feng, F. Ye, J.P. Lin, Y.L. Wang, and G.L. Chen. "Effect of Annealing Temperature on Magnetic Properties of Cold Rolled High Silicon Steel Thin Sheet." Journal of Alloys and Compounds 491, no. 1-2 (2010): 268–70. DOI: 10.1016/j.jallcom.2009.10.118.

[17] He, X.D., X. Li, and Y. Sun. "Microstructure and Magnetic Properties of High Silicon Electrical Steel Produced by Electron Beam Physical Vapor Deposition." Journal of Magnetism and Magnetic Materials 320, no. 3-4 (2008): 217–21. DOI: 10.1016/j.jmmm.2007.05.030.

[18] Mouayd, Amine Alaoui, Alexey Koltsov, Eliane Sutter, and Bernard Tribollet. "Effect of Silicon Content in Steel and Oxidation Temperature on Scale Growth and Morphology." Materials Chemistry and Physics 143, no. 3 (2014): 996–1004. DOI: 10.1016/j.matchemphys.2013.10.037.

[19] Khan, Zulfiqar A., and Matt Nugent. The Effects of Corrosion Rate and Manufacturing in the Prevention of Stress Corrosion Cracking on Structural Members of Steel Bridges. 17. Vol. 17. Fern Barrow, Poole, UK: Journal of Corrosion Science and Engineering, 2014.

[20] Martínez-Cázares, G M, R D Mercado-Solís, R Colás, and N F Garza-Montes-de-Oca. "High Temperature Oxidation of Silicon and Copper–Silicon Containing Steels." Ironmaking & Steelmaking 40, no. 3 (2013): 221–30. DOI: 10.1179/1743281212y.0000000064.

[21] Saleem, Aroba, Dina Goldbaum, Nicolas Brodusch, Raynald Gauvin, and Richard R. Chromik. "Microstructure and Mechanical Property Connections for a Punched Non-Oriented Electrical Steel Lamination." Materials Science and Engineering: A 725 (2018): 456–65. DOI: 10.1016/j.msea.2018.04.054.

[22] Baudouin, P., M. De Wulf, L. Kestens, and Y. Houbaert. "The Effect of the Guillotine Clearance on the Magnetic Properties of Electrical Steels." Journal of Magnetism and Magnetic Materials 256, no. 1-3 (2003): 32–40. DOI: 10.1016/s0304-8853(02)00004-5.

[23] Dehmani, Helmi, Charles Brugger, Thierry Palin-Luc, Charles Mareau, and Samuel Koechlin. "Study of the Contribution of Different Effects Induced by the Punching Process on the High Cycle Fatigue Strength of the M330-35A Electrical Steel." Procedia Structural Integrity 2 (2016): 3256–63. DOI: 10.1016/j.prostr.2016.06.406.

[24] Cao, Hongzhi, Linpo Hao, Jingwen Yi, Xianglin Zhang, Zhonghan Luo, Shenglin Chen, and Rongfeng Li. "The Influence of Punching Process on Residual Stress and Magnetic Domain Structure of Non-Oriented Silicon Steel." Journal of Magnetism and Magnetic Materials 406 (2016): 42–47. DOI: 10.1016/j.jmmm.2015.12.098.

[25] Maurel, Vincent, Florence Ossart, and René Billardon. "Residual Stresses in Punched Laminations: Phenomenological Analysis and Influence on the Magnetic Behavior of Electrical Steels." Journal of Applied Physics 93, no. 10 (2003): 7106–8. DOI: 10.1063/1.1557279.

[26] Lakkonavar, Virupakshappa, Swaroop Kavi, Peggy Jones, Margarita Thompson, Yew Sum Leong, and Paul Crepeau. "Edge-Quality Effects on Mechanical Properties of Stamped Non-Oriented Electrical Steel." SAE Technical Paper Series, 2020. DOI: 10.4271/2020-01-1072.

[27] Du, Liying, Guifeng Zhou, Jing Liu, Wenmin Shi, Yunjie Bi, Zhaoyang Cheng, and Huan Xue. "Fatigue Cracking Characterization of High Grade Non-Oriented Electrical Steels." Journal of Wuhan University of Technology-Mater. Sci. Ed. 32, no. 6 (2017): 1329–35. DOI: 10.1007/s11595-017-1749-9.

[28] Wang, Hongze, Yansong Zhang, and Shuhui Li. "Laser Welding of Laminated Electrical Steels." Journal of Materials Processing Technology 230 (2016): 99–108. DOI: 10.1016/j.jmatprotec.2015.11.018.

[29] Park, Joon Sik, and Kyoung Mook Lim. "Effect of Laser Welding Variables on the Formability of 3wt% Si-Added Steel Welds." Materials and Manufacturing Processes 24, no. 4 (2009): 431–37. DOI: 10.1080/10426910802714332.

[30] Schoppa, A, J Schneider, C.-D Wuppermann, and T Bakon. "Influence of Welding and Sticking of Laminations on the Magnetic Properties of Non-Oriented Electrical Steels." Journal of Magnetism and Magnetic Materials 254-255 (2003): 367–69. DOI: 10.1016/s0304-8853(02)00877-6.

[31] Lamprecht, Erik, Martin Homme, and Thomas Albrecht. "Investigations of Eddy Current Losses in Laminated Cores Due to the Impact of Various Stacking Processes." 2012 2nd International Electric Drives Production Conference (EDPC), 2012. DOI: 10.1109/edpc.2012.6425097.

[32] Zhang, Yansong, Hongze Wang, Kunkun Chen, and Shuhui Li. "Comparison of Laser and TIG Welding of Laminated Electrical Steels." Journal of Materials Processing Technology 247 (2017): 55–63. DOI: 10.1016/j.jmatprotec.2017.04.010.

[33] Marchfelder, Cornelia, Robert Pugstaller, Gernot M. Wallner, Oliver Brüggemann, and Maëlenn Aufray. "Effect of Epoxy Structure on Properties of Waterborne Coatings and Electrical Steel Laminates." Polymers 14, no. 8 (2022): 1556. DOI: 10.3390/polym14081556.

[34] Pugstaller, Robert, Gernot M. Wallner, Bernhard Strauß, and Ronald Fluch. "Advanced Characterization of Laminated Electrical Steel Structures under Shear Loading." The Journal of Adhesion 95, no. 9 (2018): 834–48. DOI: 10.1080/00218464.2018.1450747.

[35] Budynas, Richard, and J Keith Nisbett. Shigley's Mechanical Engineering Design. New York: McGraw-Hill, 2019.

[36] ASTM E8/E8M-22, Standard Test Methods for Tension Testing of Metallic Materials, 2022. DOI: 10.1520/E0008_E0008M-22.

[37] ASTM A345-16 Standard Test Methods of Tension Testing of Metallic Foil, 2016. DOI: 10.1520/E0345-16.

[38] Bode, B., A. Brueckner-Foit, and F. Zeismann. "Quasi-Static and Cyclic Failure Behavior of Electric Sheet Material." International Journal of Fatigue 82 (2016): 350–60. DOI: 10.1016/j.ijfatigue.2015.04.012.

[39] Gill, Gurmeet, Behzad Behravesh, Dulal Saha, Wensheng Zhang, Jim Chen, Gianni Lamonaca, Marie Mills, and Hamid Jahed. "Effect of Edge Finish on Fatigue Behavior of Thin Non-Oriented Electrical Steel Sheets." SAE International 2023-01-0803 (n.d.).

[40] Schayes, C., J.-B. Vogt, J. Bouquerel, and F. Palleschi. "Rotor Design Optimisation through Low Cycle Fatigue Testing." Procedia Engineering 133 (2015): 233–43. DOI: 10.1016/j.proeng.2015.12.663.

[41] Fortese, G, G Nicoletto, and E Riva. "Fatigue Behaviour of Thin Fe-Si Steel Sheets for Electric Motor Production." IOP Conference Series: Materials Science and Engineering 1038, no. 1 (2021): 012004. DOI: 10.1088/1757-899x/1038/1/012004.

[42] HENNING, M, and H VEHOFF. "Local Mechanical Behavior and Slip Band Formation within Grains of Thin Sheets." Acta Materialia 53, no. 5 (2005): 1285–92. DOI: 10.1016/j.actamat.2004.10.052.

[43] Vandenbossche, L., S. Jacobs, D. Van Hoecke, B. Weber, E. Leunis, and E. Attrazic. "Improved Iron Loss Modelling Approach for Advanced Electrical Steels Operating at High Frequencies and High Inductions in Automotive Machines." 2012 2nd International Electric Drives Production Conference (EDPC), 2012. DOI: 10.1109/edpc.2012.6425108.

[44] Tolofari, Tamuno-Ibim, Behzad Behravesh, Dulal Saha, Yi-Hsin Chen, Marie Mills, Wensheng Zhang, Gianni Lamonaca, and Hamid Jahed. "Fatigue Behaviour of Thin Electrical Steel Sheets at Room Temperature." SAE International WCX 2023, n.d.

[45] ASTM E739-23, Standard Guide for Statistical Analysis of Linear or Linearized Stress-Life (S-N) and Strain-Life (-N) Fatigue Data, 2023. DOI: 10.1520/E0739-23.

[46] Shen, C. L., P. H. Wirsching, and G. T. Cashman. "Design Curve to Characterize Fatigue Strength." Journal of Engineering Materials and Technology 118, no. 4 (1996): 535–41. DOI: 10.1115/1.2805953.

[47] Dehmani, Helmi, Charles Brugger, Thierry Palin-Luc, Charles Mareau, and Samuel Koechlin. "High Cycle Fatigue Strength of Punched Thin Fe-Si Steel Sheets." Materials Performance and Characterization 5, no. 3 (2016). DOI: 10.1520/mpc20150063.

[48] Jahed H, Roostaei A., Cyclic Plasticity of Metals, Elsevier Series on Plasticity of Materials, 2021, Elsevier, ISBN: 978-0-12-819293-1

[49] ASTM E466-15, Standard Practice for Conducting Force Controlled Constant Amplitude Axial Fatigue Tests of Metallic Materials, 2015. DOI: 10.1520/E0466-15.

[50] Van Hoecke, Dennis, Sigrid Jacobs, Lode Vandenbossche, Bastien Weber, and Emmanuel Attrazic. "Effect of Punching and Stress Concentrations on Mechanical Behaviour of Electrical Steels." World Electric Vehicle Journal 6, no. 3 (2013): 741–46. DOI: 10.3390/wevj6030741.

[51] "3D Laser Scanning Microscope – VK-X250." Keyence. Accessed April 1, 2023. https://www.keyence.com/landing/lpc/lp_vk250_micro.jsp.

[52] ASTM E384-17, Standard Test Method for Microindentation Hardness of Materials, 2017. DOI: 10.1520/E0384-99.

[53] "Automated Hardness Testing: Solutions." Clemex. https://clemex.com/image-analysis-solutions/microhardness-testing-software/.

[54] Saha, D. C., H. Jahed, S. B. Behravesh, and T. -I Tolofari. "Quasi-Static Properties of Non-Oriented Electrical Steel Sheet at Room and Elevated Temperature," n.d.

[55] A. E112-13, ASTM E112, Standard Test Methods for Determining Average Grain Size, ASTM Int. (2013) 1–28.

[56] T. Massalski, H. Okamoto, P. Subramanian, and L. Kacprzak, Binary Alloy Phase Diagrams, 2nd ed. Ohio: ASM International, 1990, vol. 3.

[57] Steiner Petrovic, Darja. (2010). Non-oriented electrical steel sheets. Materials and Technologies. 44. 317-325.

[58] Gill, Gurmeet, Behzad Behravesh, Dulal Saha, Wensheng Zhang, Jim Chen, Gianni Lamonaca, Marie Mills, and Hamid Jahed. "Fatigue Behavior of Stamped Electrical Steel Sheet at Room and Elevated Temperatures." SAE International 2023-01-0804 (n.d.).